HOKKAIDO UNIVERSITY

Title	A study of lightning magnitudes and thunderstorm activity based on the observation of VLF sferics
Author(s)	,
Citation	. ( ) 11375
Issue Date	2014-03-25
DOI	10.14943/doctoral.k11375
Doc URL	http://hdl.handle.net/2115/58164
Type	theses (doctoral)
File Information	Takeshi_Kudo.pdf

Instructions for use

Doctoral Dissertation

A study of lightning magnitudes and thunderstorm activity based on the observation of VLF sferics

（VLF 帯空電観測に基づいた落雷規模と雷雨活動に関する研究）

Takeshi Kudo

工藤 剛史

Planetary and Space Group, Department of Cosmosciences,

Graduate School of Science, Hokkaido University

北海道大学 大学院理学院 宇宙理学専攻 惑星宇宙グループ

December 2013

Dedication

To my wife

Sachiko

and to my son

Arata

Abstract

Previous studies have suggested that there is correlation between occurrence frequency of lightning and meteorological parameters, such as precipitation, radar reflectivity, and updraft of thunderstorms. The lightning data which has high time resolution is useful in investigating thunderstorms, because a space-time resolution of meteorological radar which is typically used to research thunderstorms is not enough to investigate rapid development and fine convective structure of thunderstorm. However, previous studies used only the information of lightning occurrence frequency, nevertheless each lightning has a different electrical properties, such as charge moment change (CMC).

CMC is a physical quantity which neutralized charge amount of lightning discharge times vertical discharge length. CMC and peak current intensity show lightning magnitude. CMC is estimated by observation of electromagnetic wave radiated by cloud-to-ground lightning discharge (CG) in the range of Extremely Low Frequency (ELF) . The observation of ELF band has high sensitivity for the lightning continuing current which flows continuously for the time period of few millisecond – hundreds of millisecond after the lightning return stroke. The amount of charge neutralized by continuing current is larger than that by return stroke in the presence of continuing current. The negative cloud-to-ground lightning discharge (–CG) account for 90 % or more of CGs expect in winter in Japan. The CMC of most of the –CG is smaller than 100 C·km, since approximately 40 % of –CG is accompanied with continuing current. In order to estimate the smaller CMC than 100 C·km, observation of the radiowaves in Very Low Frequency (VLF) range radiated by return stroke which has the time constant from a few tens of microsecond to a few hundreds of microsecond is required. In addition, in order to link short-term meteorological forecast and the lightning data in the future, the method of estimation of CMC in a short time with high detection efficiency

is important. However, by the current lightning detection systems covering the range of a few hundreds of km, which use radiowaves at a higher frequency over 100 kHz, only the peak current of stroke is estimated and the CMC cannot be derived.

The purpose of this thesis is to establish the methods of analysis to estimate small CMC of –CG and to investigate the relationship between developing process of thunderstorm and lightning activity with information of magnitudes (CMC) of each lightning stroke. This thesis deals with three subject: 1) development of a new VLF observation system in Kanto region, Japan and its continuous operation, 2) establishment of the methods of analysis to estimate small CMC of –CG and peak current from VLF waveform, 3) investigation of the relationship between meteorological parameters and lightning activity with information of magnitudes.

Firstly, a new VLF lightning observation system was developed. A continuous monitoring of waveform in frequency range of 2 kHz – 35 kHz at three stations in Kanto region located in the range of 150 km from Tokyo, Japan, has been carried out for the first time. Kanto region is the one of the best location to investigate the relationship between meteorological parameters and lightning activity in the world because of the dense meteorological observation networks. The observation system with three observation sites has been operated since May 15, 2013.

Secondly, peak current and CMC were estimated from VLF data. In order to estimate the peak current from VLF waveform, the relationship between the peak current of Japan Lightning Detection Network (JLDN) and normalized amplitude of electric field waveform was investigated. It is shown that high correlation between the peak current of JLDN and the normalized amplitude in the range of 50–200 km (R^2 = 0.79). The methodology to estimate peak current using waveform in VLF band, which is detectable at far distance than that in LF band was established. A new method of estimation of impulsive CMC (iCMC) with a duration of 1 ms or less without use of frequency analysis nor VLF propagation model was established. The iCMC is estimated using the duration time of electric field of groundwave identified from the VLF waveform and peak current. The data of 10,606 VLF sferics observed at Yamanashi site (35.669˚N, 138.581˚E) at the distance from 50 to 200 km were analyzed. The numbers of estimated iCMC of –CG and +CG were 7418 and 57, respectively. The detection

efficiency (DE) of iCMC estimation of –CG in this study is about 72 %, while the estimated DE of current systems for iCMC or peak current using VLF are less than 11 %. The DE of VLF lightning observation system for estimation of iCMC is the highest level in the world. The relationship between iCMC and the peak current estimated from VLF data was examined. It is found that correlation between iCMC over 20 C·km and the peak current is small ($R^2 = 0.21$), and correlation between iCMC less than 20 C·km and the peak current is high ($R^2 = 0.69$). The relationship among iCMC, the peak current and duration time of electric field waveform was also examined. There is a weak correlation between iCMC and the duration time of electric field waveform (–CG: $R^2 = 0.12$, +CG: $R^2 = 0.31$). The peak current intensities show no correlation with the duration time of electric field waveform (–CG: $R^2 = 0.03$, +CG: $R^2 = 0.05$). These results suggest that iCMC cannot be estimated from the peak current for the event over 20 C·km. It is necessary to estimate iCMC more than 20 C·km from the time variation of waveform.

Finally, using the estimated iCMC, peak current and the duration time of electric field waveform, the relationship among a time variation of rain volume, the area size of radar echo height (nearly cloud top) more than 12 km and lightning parameters for the 3 cases was examined. The rain volume and the area size of echo height more than 12 km were calculated using the Japan Meteorological Agency (JMA) C-band radar data every 10 minutes. It is found that the absolute value of iCMC of –CG increases as occurrence frequency of –CG, the area size of the radar echo height more than 12 km and rain volume increase (i.e., with the development of thunderstorm) for the first time. One possibility is that the negative charges in the cloud are carried upward by updraft or many negative charges generated by updraft are distributed in the cloud. The time variations both of the peak current and the duration time of electric field enhancement show a similar variation. It is found that occurrence frequency of –CG shows temporal decrease in advance of the occurrence of downburst on the ground by ~15 minutes, while the area size of radar echo height more than 12 km is continuously increasing for the first time in Japan. It is possible that large negatively-charged particles (hail and graupel) carried upward by strong updraft approach the positively-charged particles (ice crystal), then the occurrence frequency of –CG decreases. In addition, it is found that –

CG with iCMC smaller than 5 C·km in absolute value is dominant in the occurrence time period of the downburst. It is possible that negatively-charged hails and graupels fall to the ground with downburst, or negative charges decrease by IC and –CG activities, and the ratio of –CG with the absolute value of iCMC smaller than 5 C·km increases. In the present study, the lightning magnitudes, that is, iCMC for any CG lightning at a distance in the range of 50–200 km was examined. Comparing the distribution of the estimated lightning magnitudes with meteorological radar data, examples of the electrical properties of CG change according to the developing process of thunderstorm in some cases were suggested for the first time.

Acknowledgments

also like to express my sincere appreciation to all the staffs of OTOWA ELECTRIC CO., LTD. for their encouragement.

Finally, special thanks go to my wife, Sachiko and my son, Arata, who have been patient during the past three years while I researched in Sapporo, and for your moral support.

TAKESHI KUDO

Sapporo, Hokkaido

Contents

List of Tables

List of Figures

Chapter 1

General introduction

1.1 Lightning

A source of lightning discharges are positive and negative charges separated in the cloud. Lightning discharges are generally divided into three classes, such as intra-cloud discharge (IC), cloud-to-cloud discharge (CC) and cloud-to-ground discharge (CG). Especially with CGs, downward lightning flashes (–CG) account for about 90 percent or more of global CG lightning, and that of 10 percent or less are positive lightning flashes (+CG) [*Rakov and Uman*, 2003].

Each lightning has several electrical characteristics, not only polarity. Previous studies demonstrated that lightning peak current ranges from a few kA to a few hundred of kA range, by the observation of direct lightning current using a recording system with coaxial shunt resistor or Rogowski coil [e.g., *Berger*, 1967; *Narita et al.*, 2000]. Figure 1.1 shows the cumulative frequency distributions of peak current observed at the transmission towers in Japan, and the results are superimposed on the results of early studies [*Narita et al.*, 2000]. The mean of lightning peak current is about 30 kA. Early observations show that neutralized electric charge ranges from 1 coulomb to hundreds of coulombs [e.g., *Berger*, 1967; *Fisher et al.*, 1993]. It is suggested that the charge moment change (CMC) which is a value of multiplying removed charge in the thundercloud by vertical discharge channel has a wide range more than few hundred times the value of CMC [e.g., *Fullekrug et al.*, 2002; *Williams et al.*, 2006]. Figure 1.2 shows the global distribution of CMC [*Yamashita et al.,* 2011]. Most of –CGs are

1

smaller than 100 C·km [*Kase et al.*, 2009; *Yamashita et al.*, 2011]. –CG of small CMC is not accompanied with continuing current.

   Measurement of the electromagnetic radiation produced by lightning discharge is suitable for the investigation of the electrical property of lightning discharges. Lightning discharge radiates electromagnetic wave from a few Hz to s a few hundred of MHz [*Burke and Jones*, 1992; *Weidman and Krider*, 1986]. Each frequency band of the electromagnetic wave is caused by the different process of lightning discharge. The electromagnetic waves of VHF (Very High Frequency, 30 MHz − 300 MHz) band are radiated by extending leader and streamer in the process of initial breakdown discharge. Return stroke of lightning discharge radiates VLF (Very Low Frequency, 3 kHz − 30 kHz) and LF (Low Frequency, 30 kHz − 300 kHz) waves. ELF (Extremely Low Frequency, 3 Hz − 3 kHz) waves are radiated by whole CG process including continuing current which flow continuously for the time period of few millisecond − hundreds of millisecond after the lightning return stroke.
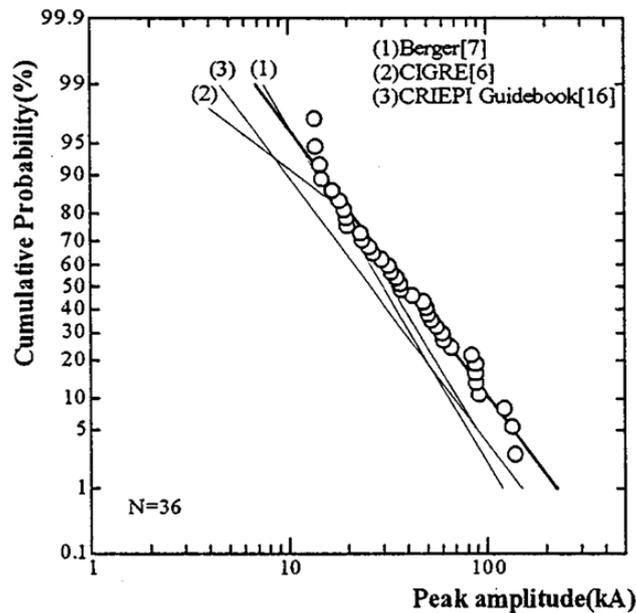
Figure 1.1. Cumulative frequency distributions of peak current of lightning strokes [*Narita et al.*, 2000].
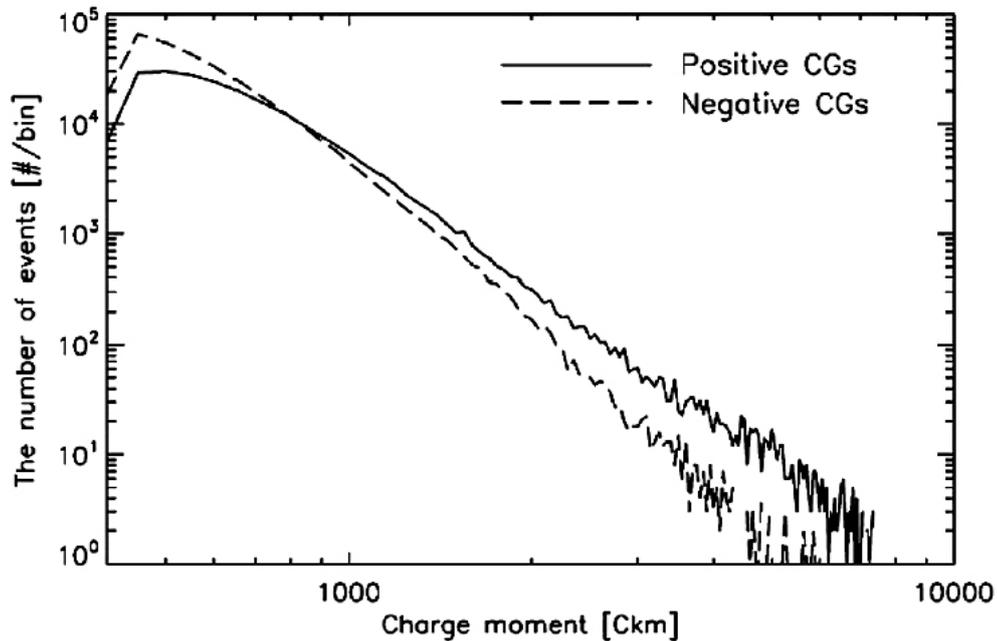
Figure 1.2. Distribution of charge moments with whole events. The number of positive CGs and negative ones are 182,689 and 288,046 respectively. [*Yamashita et al.*, 2011].

1.2   Relationship between lightning activity and meteorological parameters

Most of lightning occur in the developed convection clouds which often brings concentrated heavy rain and results in flash floods and wreaks enormous damage. There is a commonly held view that strong updraft and graupel-ice mechanism [*Takahashi*, 1978] in the mixed phase region of the cloud pose electrical charge separation in the cloud. Previous studies suggested that there is correlation between occurrence frequency of lightning and meteorological parameters, such as precipitation, radar reflectivity, and updraft of thunderstorms. Figure 1.3 shows a schematic diagram of the relationship between the lightning activity and the meteorological parameters. The rain volume and cloud height estimated from meteorological radar, intensity of radar reflectivity, and occurrence of downburst, tornado and hail typically indicate aspect of storm evolution.
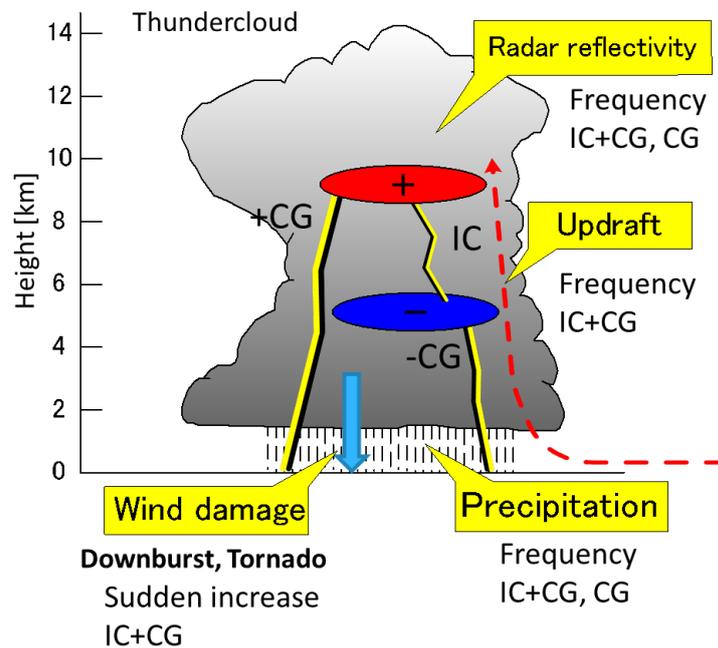
Figure 1.3 Schematic diagram of relationship between atmospheric parameters and lightning activity.

Many studies suggested that lightning occurrence frequency and rain activity generally show a similar variation [*Tapia et al.*, 1998; *Carey and Rutledge*, 2000; *Soula and Chauzy*, 2001]. *Tapia et al.* [1998] show that seasonal and diurnal analysis of rainfall and lightning climatology in Florida illustrate the correlation between lightning occurrence and convective rainfall. In addition, rainfall flux and lightning frequency are well correlated for analyzed 22 storm. Figure 1.4 shows an evolution of the rain rate and of the flash rates on July 11, 1997 in northern France [*Soula and Chauzy*, 2001]. The time evolution of lightning flash rate and that of the rainfall rate show good correspondence in this case. Some studies found that the frequency of CG flashes tends to peak a few minutes before the surface rainfall [*Tapia et al*., 1998; *Gungle and Krider*, 2006]. *Gungle and Krider* [2006] suggested that the storms that produce lager number of CG flashes tend to produce longer lag time. In order to lead to a better estimation of convective rainfall in areas with poor or incomplete coverage regions, the Rainfall-Lightning ratio of isolated thunderstorm was examined [*Kempf and Krider*, 2003; *Price and Federmesser*, 2006; *Pineda et al.*, 2007].
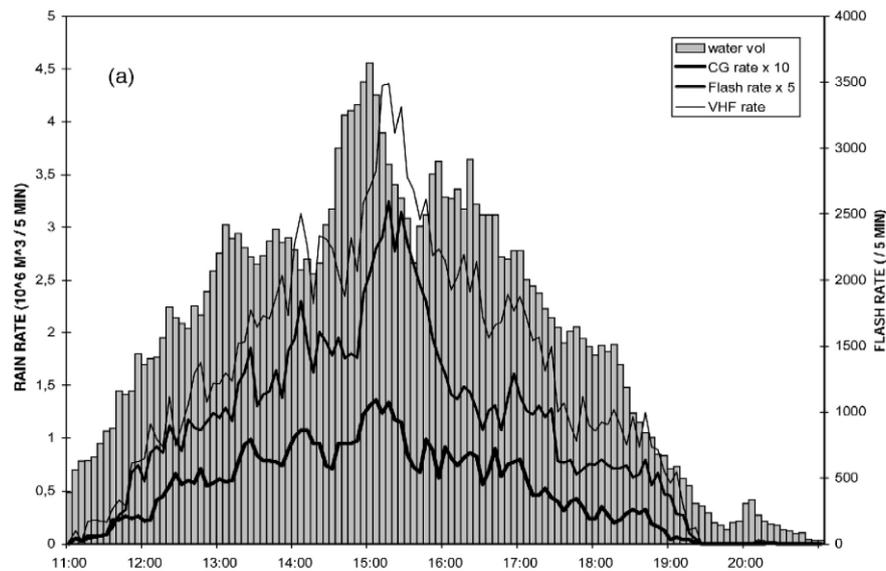
Figure 1.4. Evolution of the rain rate and of the flash rates. (a) July 11, 1997 [*Soula and Chauzy*, 2001].

Meteorological radar contributes not only to the understanding of distribution and intensity of precipitation but also to the vertical structure of thunderstorm, wind structure, and precipitation particle (graupel/hail). *Seity et al.* [2003] found that CG flash rates are well correlated with the volume of graupel-hail mixture in the cell and with the volume having radar reflectivity greater than 35 dBZ (R = 0.8~) using Doppler and polarimetric radar data for 5 cells of thunderstorm in northern Italy.

Previous studies investigated the relationship between the lightning activity and the updraft of thunderstorm [*Zipser and Lutz*, 1994; *Tessendorf et al.*, 2005; *Wiens et al.*, 2005]. *Tessendorf et al.* [2005] found correlation between the updraft volume exceeding 10 m/s and total lightning activity for one severe thunderstorm in United States. *Deierling and Petersen* [2008] found that time series of updraft volume in the charging zone with vertical velocities greater than either 5 or 10 m/s have clear relationship with total lightning activity (IC and CG) for 11 thunderstorms in United States (r = 0.93).
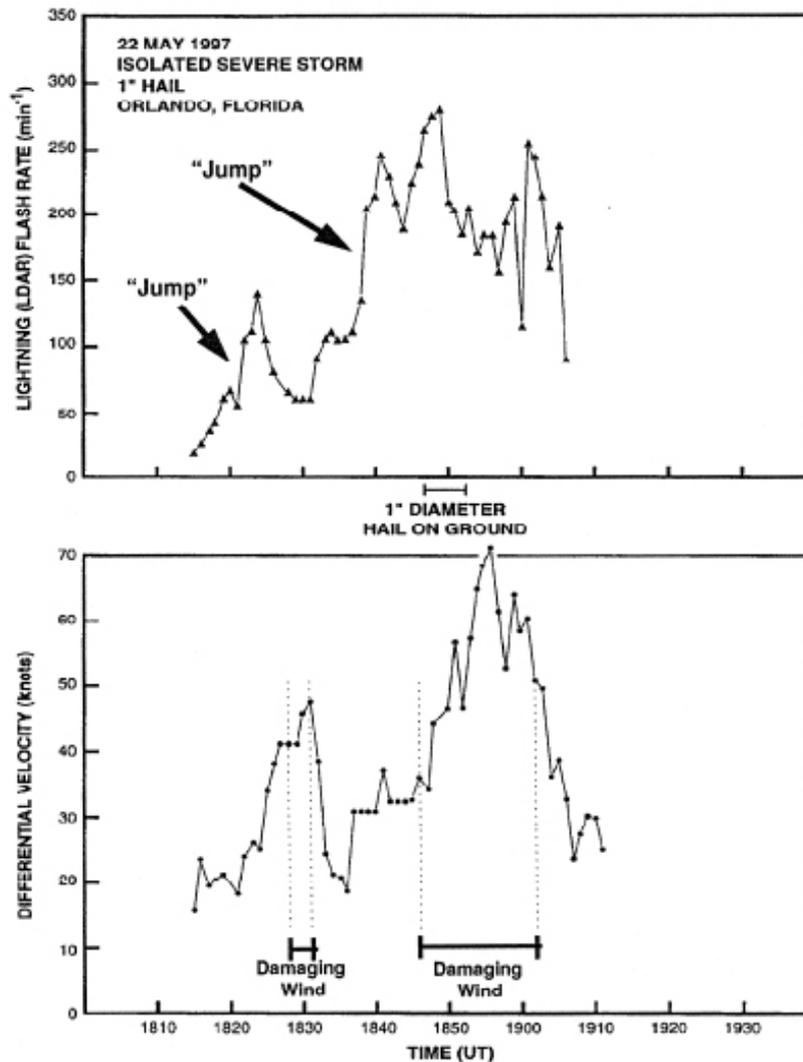
Figure 1.5. May 22, 1997 hailstorm with severe microburst near Orlando. (a) History of total lightning flash rate, and (b) history of differential radial Doppler velocity at the surface [*Williams et al.*, 1999].

An interesting behavior of total lightning (IC+CG) activity in advance of the occurrence of severe weather such as downburst, hail, and tornadoes was found in United States [*Williams et al.*, 1999; *Goodman et al.*, 2005; *Schultz et al.*, 2009; *MacGorman et al.*, 2012].The behavior called as lightning jumps is that total lightning frequency rapidly increase in advance of severe weather. Figure 1.5 shows (a) history of total lightning flash rate, and (b) history of differential radial Doppler velocity at the surface [*Williams et al.*, 1999]. It is shown that the total lightning frequency rapidly increased in advance of the occurrence of damaging wind at the surface.

Lightning data have been used in the mesoscale forecast models. The weather forecast was improved by assimilating lightning data [*Alexander et al.*, 1999; *Chang et al.*, 2001; *Mansell et al.*, 2007; *Pessi and Businger*, 2009]. Lightning data have been also used for flash flood forecast [*Price et al.*, 2011]. The method of lightning data assimilation proposed by *Mansell et al.* [2007] used lightning as a proxy for the presence or absence of deep convection. For the case study, the lightning assimilation was successful not only in aspect of rain intensity but also in generating cold pools that were present in the surface observations at initialization of the forecast. Figure 1.5 shows the observed and modeled total precipitation for a 6-h period starting 0600 UTC 20 Jul 2000 during the spinup period [*Mansell et al.*, 2007]. The cases with lightning data assimilation and have a reproducibility compared with the case of no lightning assimilation.

The lightning data which has high time resolution is useful in investigating thunderstorms, because a space-time resolution of meteorological radar which is typically used to research thunderstorms (1–2 km) is not enough to investigate rapid development and fine convective structure of thunderstorms. However, previous studies used the lightning occurrence frequency only, nevertheless each lightning has different electrical properties. There are very few studies focused on CMC for examining the relationship between the lightning activity and the meteorological parameters.
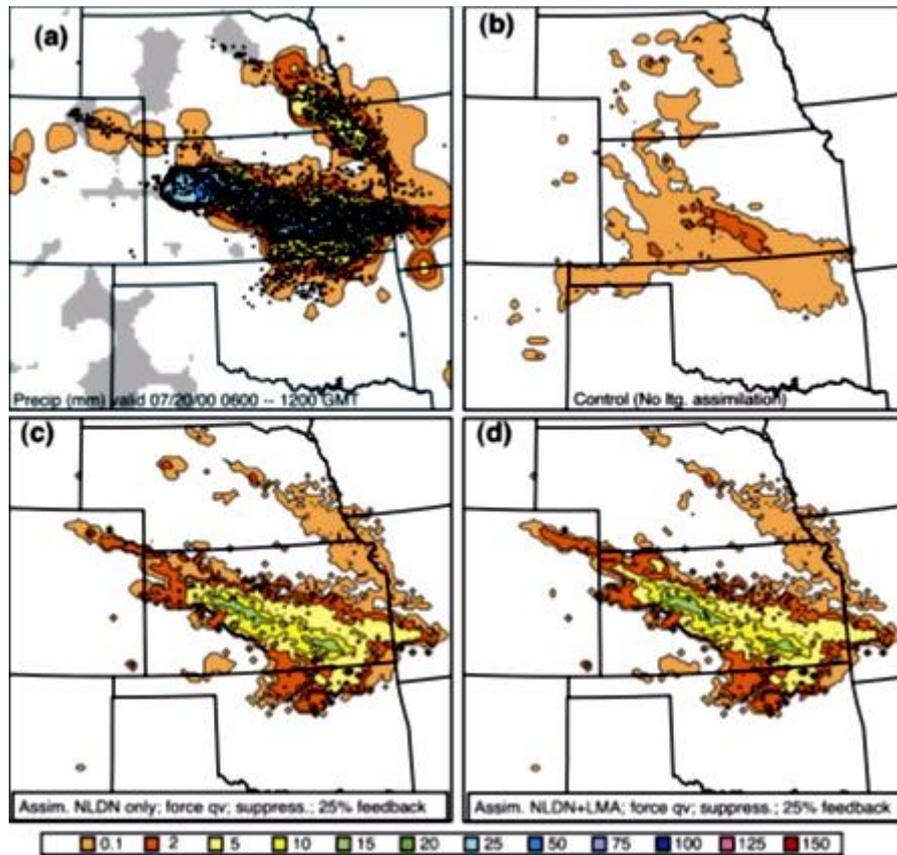
Figure 1.6. Observed and modeled total precipitation (mm) for a 6-h period starting 0600 UTC 20 Jul 2000 during the spinup period. (a) Rain gauge data with sampled NLDN strikes. (The 1st and 30th strikes are plotted in each 10-km grid box.) Gray-filled areas indicate data voids. (b) Pure forecast (no lightning assimilation). (c) With assimilation of CG lightning from NLDN, moisture forcing, and full suppression. (d) With assimilation of both CG and total (LMA) lightning, moisture forcing, full suppression, and 25% feedback of KF precipitation [*Mansell et al*., 2007]

1.3   VLF electromagnetic wave from lightning discharge

VLF electromagnetic wave from lightning is radiated by return stroke. Large part of the electromagnetic energy radiated from lightning discharge is in the VLF frequency range. Figure 1.7 shows the frequency spectra for 18 lightning strokes at the distance of about 50 km [*Uman*, 1984]. The higher frequencies than the VLF range, the energy is smaller.
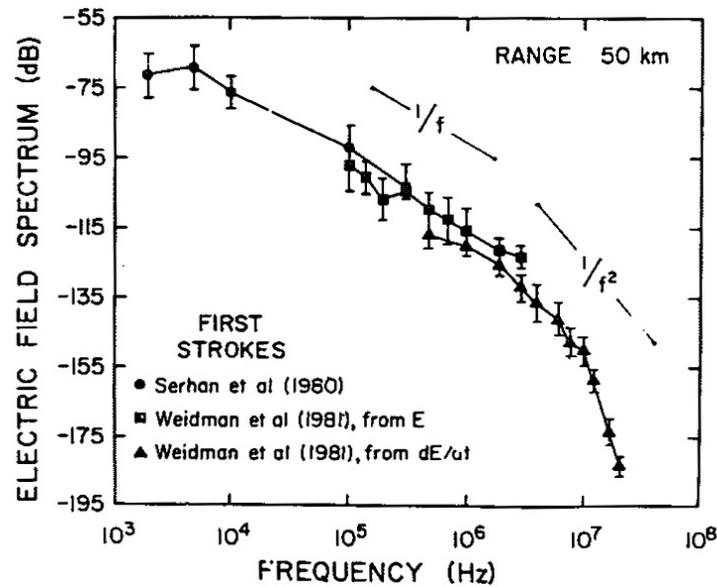
Figure 1.7. Frequency spectra for 18 strokes at a distance of about 50 km [*Uman*, 1984].

VLF radiowave propagates with very low attenuation, about 2 dB/Mm. VLF waves are reflected by the lower ionosphere at altitude of about 70 km at daytime, and about 85 km at nighttime, respectively [*Marshall*, 2009]. The ground wave (direct wave) which propagates along the surface of the earth is stronger than the skywave (reflected wave) within 1,000 km from radiation source. The skywave dominate at more than 1,000 km [*Pessi et al.*, 2009, *Said et al.*, 2010]. Figure 1.8 shows a schematic diagram of the earth-ionosphere waveguide, which allows VLF (3 kHz – 30 kHz) emissions from thunderstorms (sferics) to propagate thousands of kilometers through reflection [*Pessi et al.*, 2009]. Figure 1.9 shows that a time of arrival of the skywave varies depending on the distance and a period of time (day or night) [*Said et al.*, 2010].

These characteristics of VLF sferics which is abroadband electromagnetic impulse generated by lightning discharges make it possible to observe lightning discharges with extensive coverage (~4,000 km). VLF sferics include the information of peak current and impulsive charge moment change with a duration of 1 ms or less.
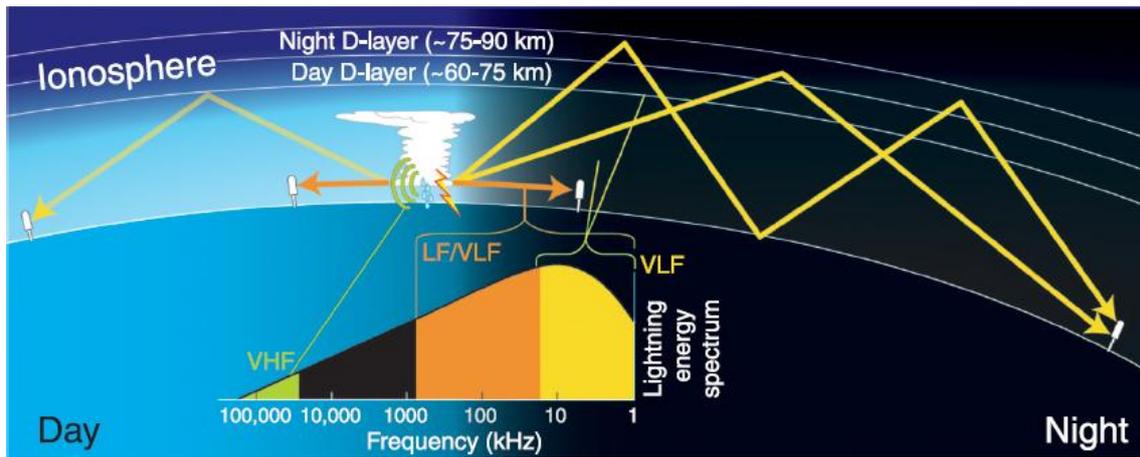
Figure 1.8 Schematic diagram of the earth–ionosphere waveguide, which allows VLF (3 kHz – 30 kHz) emissions from thunderstorms (sferics) to propagate thousands of kilometers through reflection [*Pessi et al.*, 2009].
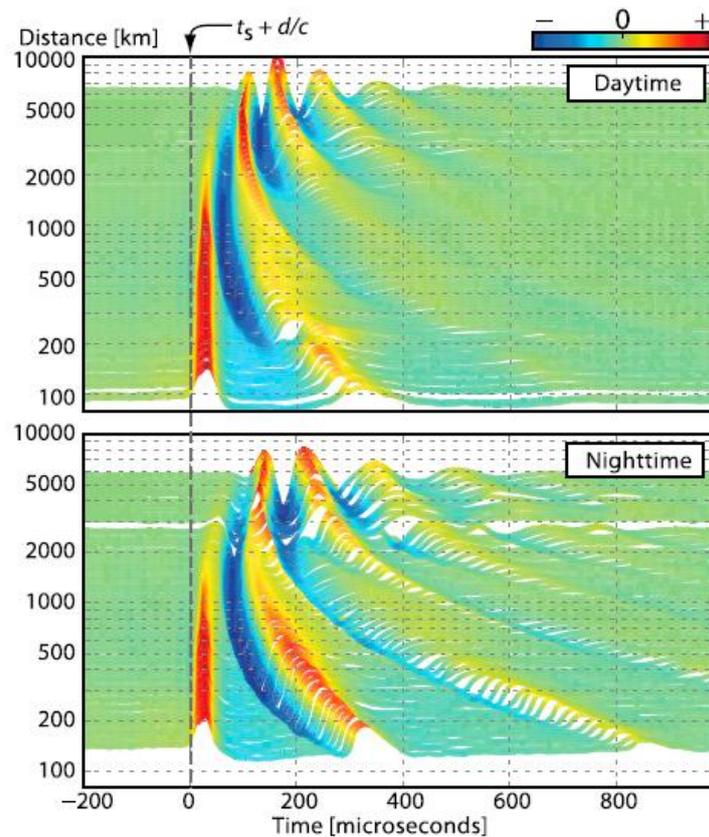
Figure 1.9. Day and night VLF average waveform banks radiated from lightning [*Said et al.*, 2010].

1.4   Lightning observation system and electrical properties of lightning

The World Wide Lightning Location Network (WWLLN) consisted of 57 VLF stations is a long-range network of locating lightning strokes [*Hutchins et al.*, 2012]. The lightning location is determined using the time of group arrival (TOGA) of the VLF (3 kHz – 30 kHz) radiation from a lightning stroke [*Dowden et al.*, 2002; *Rodger et al.*, 2009]. The overall detection efficiency of CG flashes is 10.3 % in 2008–2009, and the location accuracy is confirmed to have a northward and westward bias, with average location errors of 4.03 km in the north-south and 4.98 km in the east-west directions, respectively [*Abarca et al.*, 2010]. Peak currents weaker than −35 kA have a detection efficiency lower than 10 % compared with the NLDN (National Lightning Detection Network) [*Abarca et al.*, 2010]. The WWLLN can estimate the occurrence time, location, peak current of individual lightning strokes. Figure 1.10 shows location of the WWLLN stations (black triangles) and the result of global stroke density estimated by the WWLLN [*Hutchins* et al., 2012].
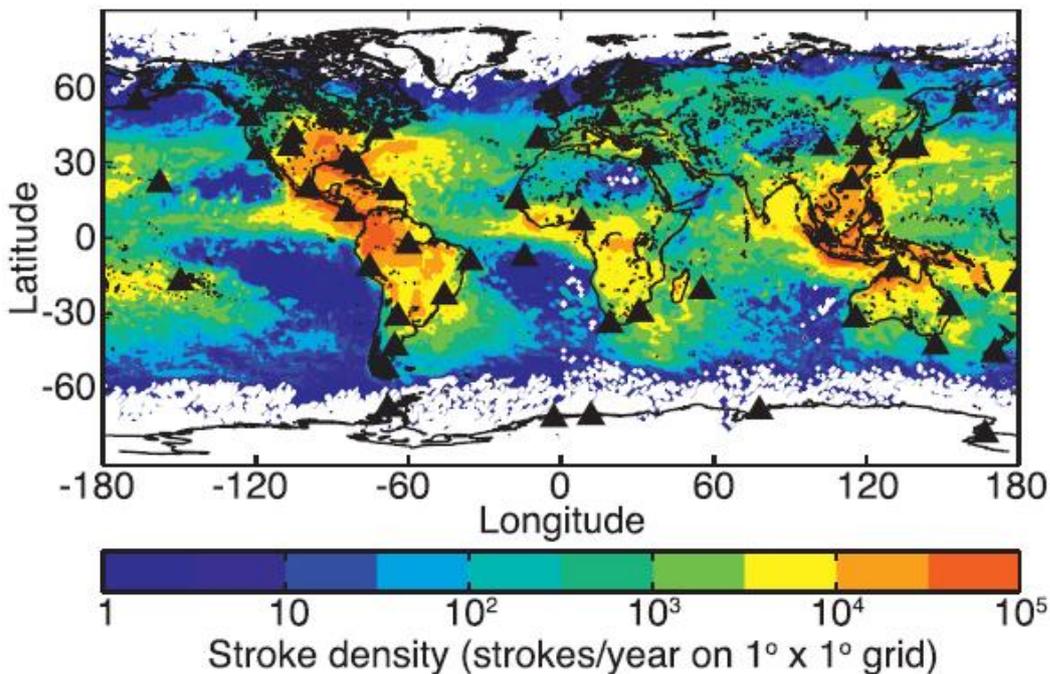
Figure 1.10. WWLLN 2010 global stroke on 1°×1° grid, station location shown (black triangles) [*Hutchins et al.*, 2012].

The Pacific Lightning Detection Network/long-range lightning detection network (PacNet/LLDN) has monitored lightning activity over the central North Pacific Ocean using both magnetic direction finding (MDF) and time of arrival (TOA) of VLF wave [*Pessi et al.*, 2009]. The daytime and nighttime flash detection efficiency in the northcentral Pacific is in the range of 17–23 % and 40–61 %, respectively, and the median location accuracy is in the range of 13–40 km [*Pessi et al.*, 2009]. The PacNet/LLDN can estimate the occurrence time and location of individual lightning strokes.

The arrival time difference long–range lightning location network (ATDnet) consisted of 10 stations in Europe is the long-range VLF lightning location network [*Nash et al., 2005*; *Bennett et al.*, 2010]. The lightning location is determined using the time of arrival of the VLF (6.87 kHz – 20.6 kHz) radiation from a lightning stroke [*Bennett et al.*, 2010]. The detection efficiency is in the range of 70– 90 % (Winter) and 20– 90 % (Summer) in the United Kingdom and 10– 70 % in the Europe [*Keogh et al.*, 2006]. The median location accuracy is 4.9 km in the France compared with the location of Meteo France systems which provide the location accuracy of lightning with better than 1 km [*Gaffard et al.*, 2008]. The ATDnet can estimate the occurrence time and location of individual lightning strokes.

The NLDN has provided lightning data covering the continental United States. The lightning location is determined using time of arrival (TOA) of the VLF/LF (1 kHz –1 MHz [*Krider et al.*, 1980]). The detection efficiency of NLDN is approximately 90 % [*Biagi et al.*, 2007], the median accuracy of location is 500 m [*Cummins et al.*, 1998]. NLDN can estimate the occurrence time, location, polarity, peak current of individual lightning strokes. Since NLDN operate on groundwaves in the VLF/LF frequency range, NLDN is comprised of more than 100 sensors covering the United States. In fact, NLDN require dense observations (approximately 300 km spacing). There are more than 60 networks of same system worldwide [*Cummins and Murphy*, 2009].

The Japan Lightning Detection Network (JLDN) which covers the whole area of Japan with 30 sensor is same system as the NLDN. The detection efficiency of –CG in summer is expected more than 90 % in the four main islands of Japan [*Ishii et al.*, 2001a]. The median accuracy of location is 1.08 km [*Ishii et al.*, 2001b]. JLDN can

estimate the occurrence time, location, polarity, peak current of individual lightning strokes.

The lightning charge moment change network (CMCN) which combines the NLDN lightning event geolocations with ELF (less than 1 kHz) data from two stations has provided impulse charge moment change (the lightning charge moment change during the first 2 ms after the discharge onset) measurements across the entire United States in near real time [*Cummer et al*., 2013]. The CMCN automatically computes impulse charge moment change for the event with the peak current magnitude of NLDN more than 10 kA. The detection efficiency is approximately 9.3 % for total lightning events, and 20 % and lower for lightning events below 40 kA [*Cummer et al.*, 2013].

By the current lightning detection systems covering the range of a few hundreds of km, which use radiowaves at the higher frequency over 100 kHz, only the peak current of the stroke is estimated and the CMC cannot be derived. The detection efficiency of current lightning detection network which can estimate CMC is low to examine the relationship between the meteorological parameters and the lightning magnitudes for investigating thunderstorms.

1.5   Purpose of this thesis

Previous researches show that the lightning data is effective and important in investigating thunderstorms. However, most of them used the lightning occurrence frequency only, nevertheless each lightning has different magnitudes which might be quantitatively related to the meteorological parameters. Little attention has been given to lightning magnitudes such as CMC of each lightning. In order to estimate the small charge moment change, observation of the VLF (2 kHz – 35 kHz in this thesis) radiowave radiated by return stroke which has the time constant from a few tens of microsecond to a few hundreds of microsecond is required. In addition, in order to link short-term meteorological forecast and lightning data in the future, the method of estimation of CMC in a short time is important for operational use.

The purpose of this thesis is to establish the method of analysis to estimate small CMC of –CG and to investigate the relationship between the developing process of thunderstorm and the lightning activity with information of magnitudes (CMC). This thesis deals with three subjects: 1) development of a new VLF observation system in Kanto region, Japan and its continuous operation, 2) establishment of the method of analysis to estimate small CMC of –CG and peak current form VLF waveform, 3) investigation of the relationship between meteorological parameters and lightning activity with information of magnitudes.

A new method of estimation of peak current and charge moment change without use of frequency analysis nor VLF propagation model was established. The relationship between the thunderstorm evolution and the lightning activity with information of electrical properties was investigated using the estimated charge moment change and peak current.

This dissertation is composed of 5 chapters. In Chapter 2, the instruments and construction of VLF observation system is introduced. In Chapter 3, the method of analysis to estimate small CMC of small CG and peak current form VLF waveform is described. In Chapter 4, the investigation of relationship between developing process of thunderstorm and lightning activity with the information of magnitudes is described and obtained results are discussed. Finally, the summary and conclusions of this dissertation and the suggestion for future works are presented in Chapter 5.

Chapter 2

Observations

2.1 VLF measurement system

A new measurement system for VLF electromagnetic field was developed. The VLF lightning observation network with identical observation system, consisting of three observation sites in Kanto region, Japan, was constructed. Purpose of this observation is to detect lightning discharges which occur within a few hundreds of km from observation site. The antennas for electric and magnetic fields are not required to be large because lightning events at distance within a few hundreds of km from observation site are observed. Also since the observation system is installed in a small space, compact antennas are used.

  In this chapter, each developed instrumentation is introduced in detail. Each observation system is composed of a vertical electric dipole antenna and two horizontal magnetic loop antennas, amplifiers, data recording system and GPS clock (Figure 2.1).
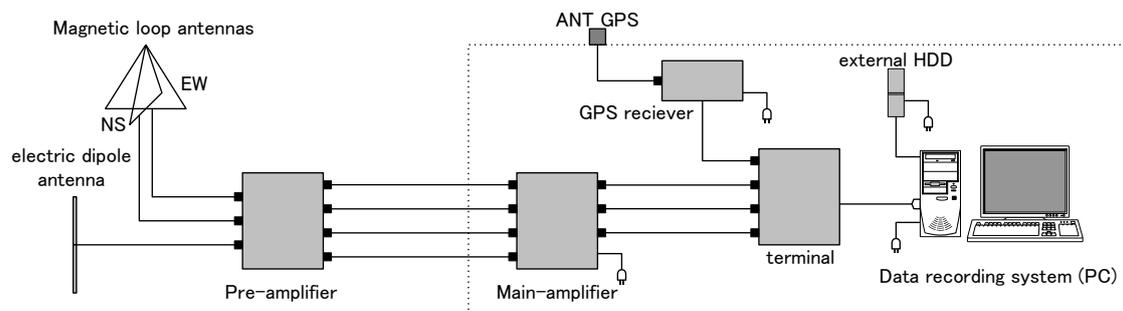
Figure 2.1. Block diagram of the VLF observation system.

2.1.1   Vertical Electric field

The vertical dipole antenna, pre-amplifier and main-amplifier were made. The equipment to observe the raidowaves on the VLF range was designed. The antenna is composed of two elements of aluminum rod with a length of 1 m and a diameter of 6 mm. Because the wavelength of VLF electromagnetic wave is order of several tens of km to several hundreds of km, the antenna can be presumed as a minute dipole antenna. The output voltage of the antenna depends on the capacitance of the element. Figure 2.2 shows a schematic diagram of the antenna and pre-amplifier.

According to *Ohkubo* [2004], the capacitance of antenna is given as

$$C_a = \frac{2\pi\varepsilon_0 l}{\log\left(\frac{l}{\sqrt{3}a}\right)} \ [\text{F}] \tag{2.1}$$

where ε_0 is the dielectric constant, l is the length of antenna, a is the radius of antenna. Substituting $l = 2.0$ [m], $a = 0.06$ [m] into the equation, C_a is given as 56.58 [pF].

Figure 2.2. Schematic diagram of the antenna and pre-amplifier.

   In order to receive an output voltage of the antenna with certainty, the pre-amplifier was installed near the antenna. The input impedance of the pre-amplifier is 10^{10} [Ω]. A circuit diagram of pre-amplifier is shown in Figure 2.3. The characteristic value and the equivalent electric circuit of the antenna and pre-amplifier are shown in Table 2.1 and Figure 2.4, respectively.
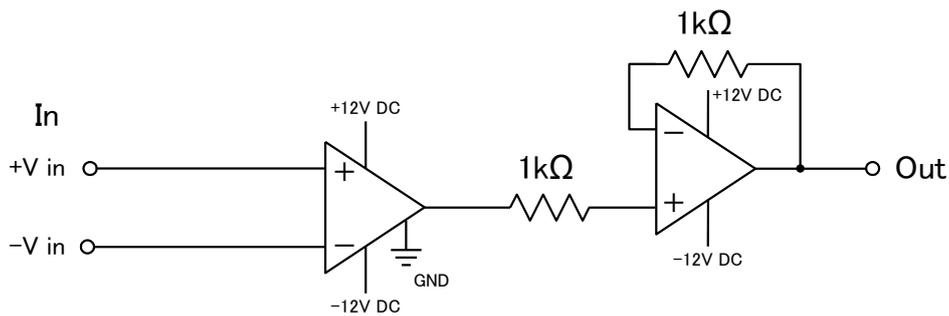
Figure 2.3. Circuit diagram of the pre-amplifier

Table 2.1. Characteristic value of the antenna and pre-amplifier.

L (Length of antenna)	2 [m]
Ca (Capacitance of antenna)	56.58 [pF]
Ci (Input capacitance)	15 [pF]
Ri (Input impedance)	10^{10} [Ω]
G (Gain of pre-amplifier)	1
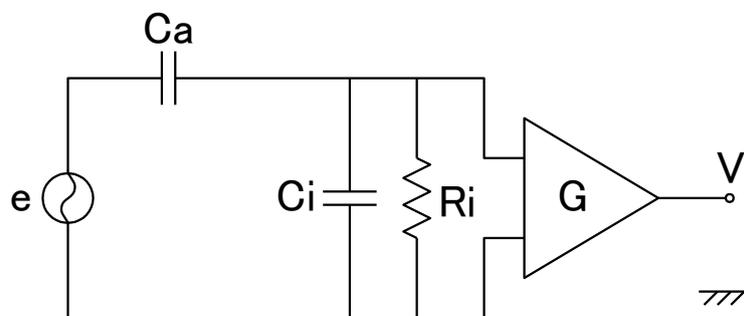
Figure 2.4. Equivalent electric circuit of the antenna and pre-amplifier.

An electromotive force from a dipole antenna is determined by multiplying effective length of the antenna (h_{eff}) by amplitude value of electric field (E). Since the length of the dipole antenna is very short compared with wavelength of VLF radiowave, the effective length can be presumed as a real length of the antenna. Moreover, since the input impedance of the pre-amplifier is extremely high, the output voltage is determined from the ratio of capacitances of the antenna and the input impedance. The relational expression is given as

$$\mathrm{V} = \frac{\dfrac{1}{i\omega C_i} + \dfrac{1}{i\omega C_a}}{\dfrac{1}{i\omega C_i}} \times G h_{eff} E = \left(1 + \frac{C_i}{C_a}\right) \times G h_{eff} E \qquad (2.2)$$

where V is the output voltage, C_i is the input capacitance, and G is gain of the pre-amplifier.

Figure 2.5 shows a circuit diagram of the main-amplifier of electric field. The main-amplifier of magnetic field is same circuit configuration with that of electric field. The band-pass filter consists of 2nd high-pass filter with a cutoff frequency of 500 Hz, 6th low-pass filter with a cutoff frequency of 50 kHz. The magnification of electric field of +20 dB was selected from +6 dB, +14 dB, +20 dB and +40 dB.

The frequency characteristics of gain and phase including pre-amplifier and main-amplifier is shown in Figure 2.6 and Figure 2.7, respectively. The lower cut-off frequency and higher cut-off frequency including main-amplifier and pre-amplifier is 1.7 kHz and 28 kHz, respectively. The original waveform was reconstructed using these characteristics of the instrumentation. The method of reconstruction of the waveform is explained in section 3.2.4.
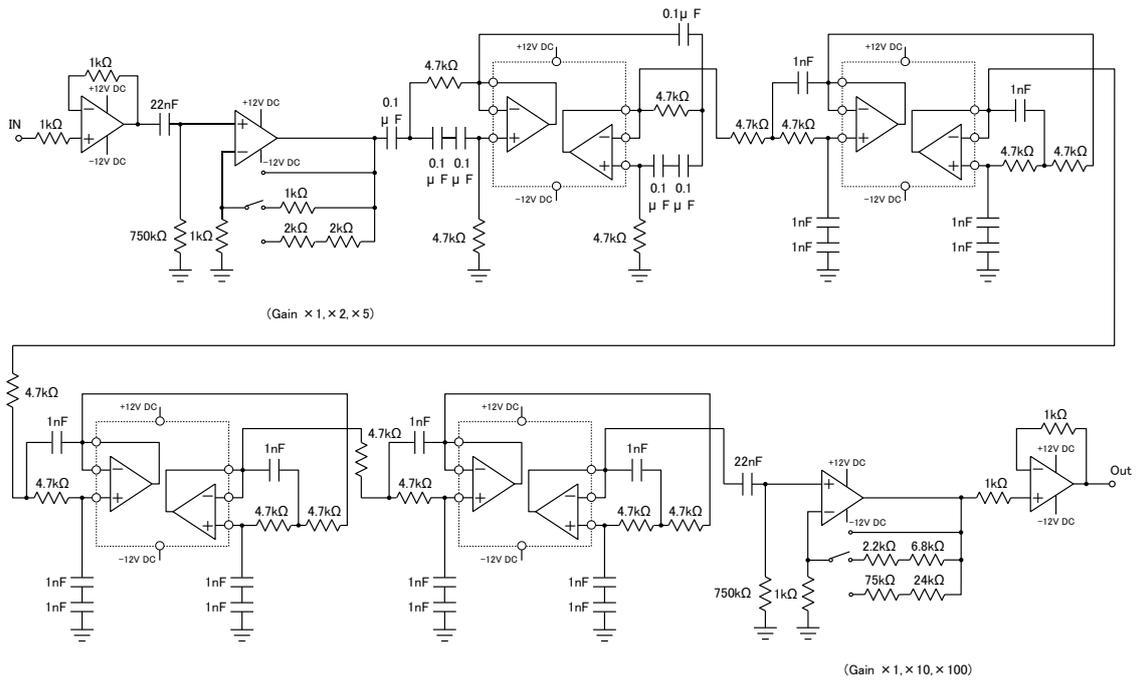
Figure 2.5. Circuit diagram of the main-amplifier.
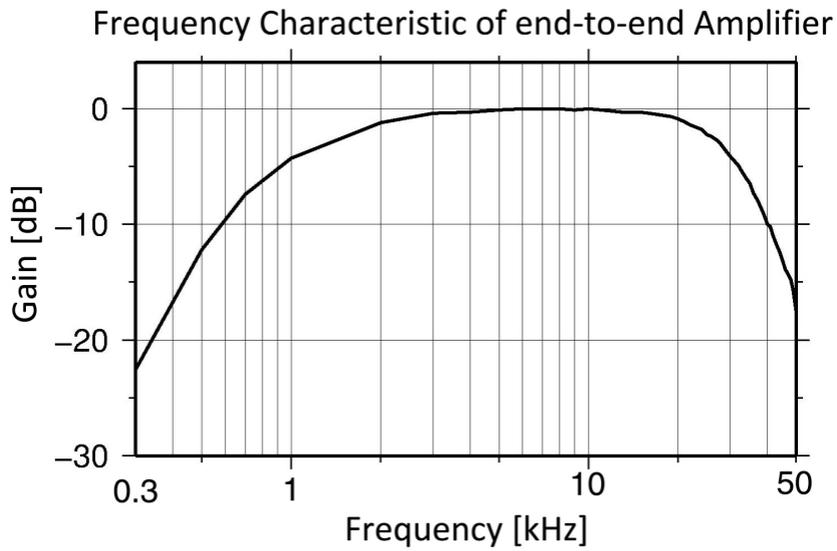
Figure 2.6. Frequency characteristic of gain including main-amplifier and pre-amplifier.

Frequency Characteristic of end-to-end Amplifier
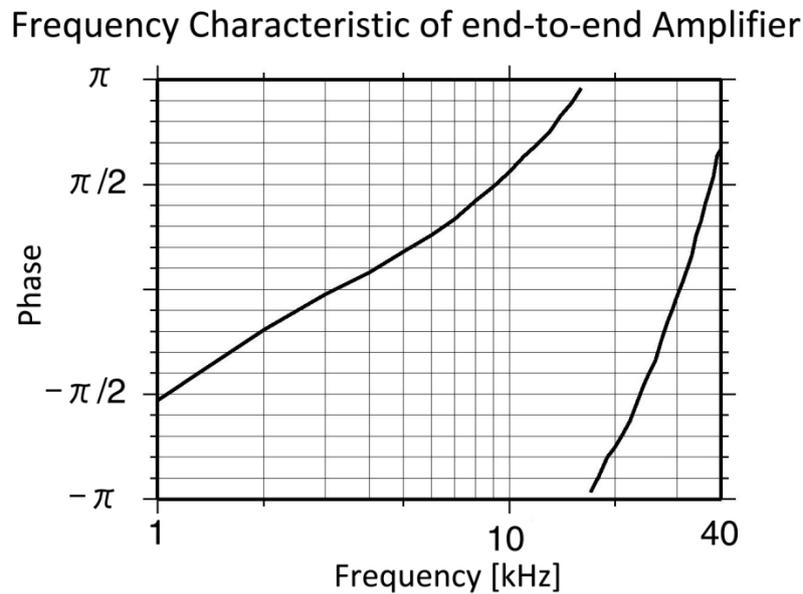
Figure 2.7. Frequency characteristic of phase including main-amplifier and pre-amplifier.

2.1.2   Magnetic field

The magnetic field measurement system consists of two horizontal magnetic loop antennas, pre-amplifiers and main-amplifier. The loop antenna and pre-amplifier were designed so as to avoid the resonant frequency in the observation band. A shape of loop antenna is triangle with 1.4 m base and 1.4 m height. The number of turns of the antenna is five. The characteristic value and equivalent electric circuit of the antenna and pre-amplifier, equivalent electric circuit of the antenna and pre-amplifier, and a circuit diagram of main-amplifier are shown in Table 2.2, Figure 2.8 and Figure 2.9, respectively. Figure 2.10 and Figure 2.11 show view of the developed main-amplifier and pre-amplifier, respectively.

Table 2.2 Characteristic value of the antenna and pre-amplifier.

N (Number of turn)	5 [turns]
S (Area of antenna)	0.98 [m^2]
La (Inductance of antenna)	86.83 [μH]
Ra (Impedance of antenna)	0.896 [Ω]
Ci (Input capacitance)	0.047 [μF]
Ri (input impedance)	10^{12} [Ω]
G (Gain of pre-amplifier)	25
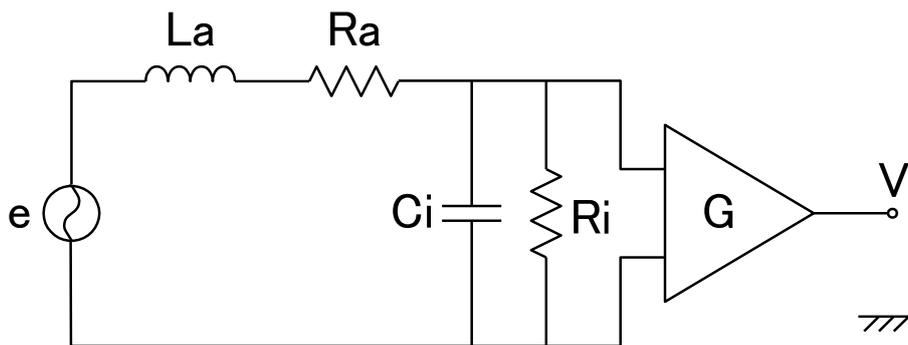
Figure 2.8. Equivalent electric circuit of the antenna and pre-amplifier.
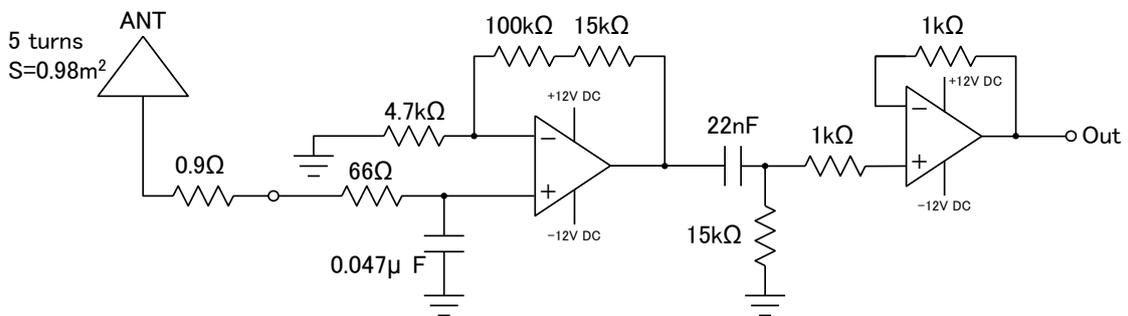
Figure 2.9. Circuit diagram of the pre-amplifier.
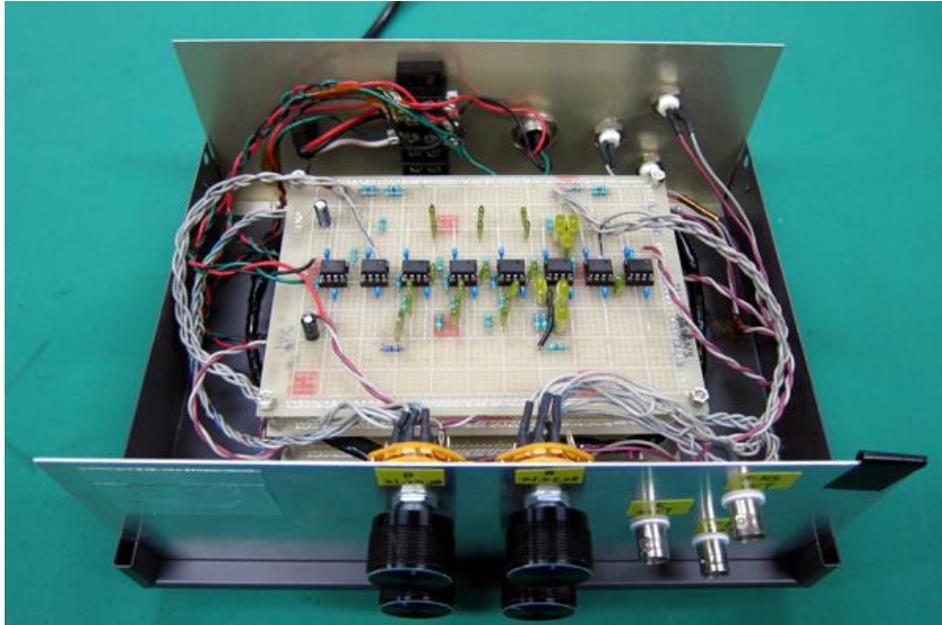
Figure 2.10. View of the main-amplifier.
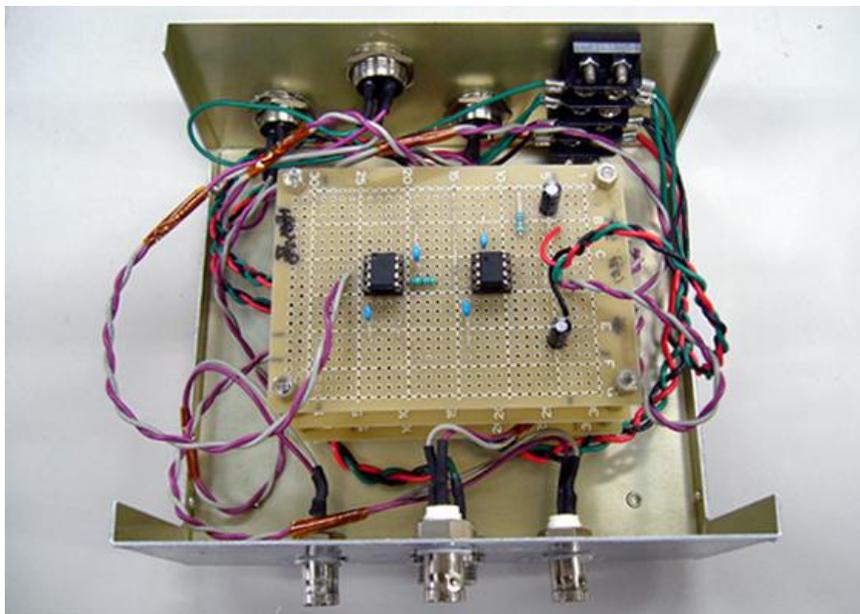
Figure 2.11. View of the pre-amplifier.

An electromotive fore (e_{mf}) generated by the magnetic flux (φ) change is given as

$$e_{mf} = -N\frac{d\emptyset}{dt} = -SN\frac{dB}{dt} \tag{2.3}$$

where N in equation (2.3) is the turn number of the antenna, S is the area of the antenna, B is the magnetic flux density. Assuming $B = B_0\,exp(-i\omega t)$, the absolute value (|e|) is given as

$$\left|e_{mf}\right| = SNB_0\omega = 2\pi SNB_0 f \tag{2.4}$$

where ω is the angular frequency and f is the frequency. Since R_i is extremely high with 10^{12} [Ω], the output voltage is given as

$$|V| = \frac{A\left|\frac{1}{i\omega C_i}\right|}{\left|R_e + i\omega L + \frac{1}{i\omega C_i}\right|}\left|e_{mf}\right| = \frac{A\frac{1}{\omega C_i}}{\sqrt{R_e{}^2 + (\omega L - \frac{1}{\omega C_i})^2}} \tag{2.5}$$

where R_e is the sum of resistance of antenna and serial resistance of the low-pass filter. Substituting e_{mf} (electromotive force) and f (frequency), the following equation was obtained.

$$|V| = \frac{2\pi GSNB_0 f}{\sqrt{(2\pi C_i R_e f)^2 + ((2\pi f)^2 C_i L_a - 1)^2}} \tag{2.6}$$

where L_a is the inductance of antenna. Substituting the characteristic value of the antenna and pre-amplifier in table 2.2 into equation (2.6), the frequency characteristic of output voltage is obtained. Figure 2.12 shows the frequency characteristic of gain of magnetic field.

Frequency Characteristic of antenna and pre-Amplifier
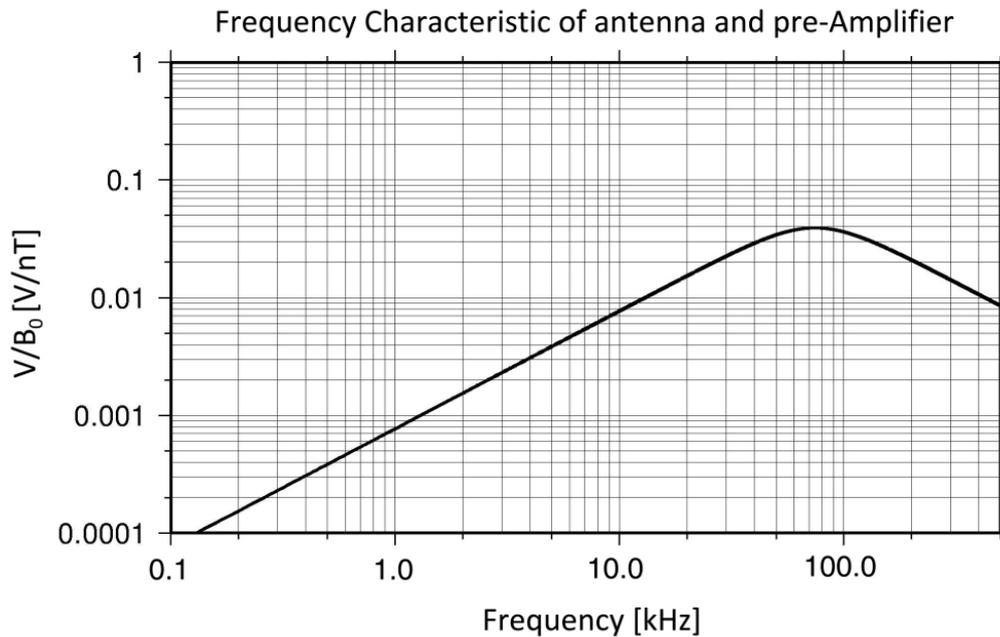
Figure 2.12. Frequency characteristic of gain of magnetic field.

2.1.3   Data recording system

Data recording system with an A/D board, GPS and personal computer (PC) was developed to obtain the VLF lightning waveforms. Lightning geo-location accuracy must be less than 10 km because level scale of the single cell of thunderstorm is approximately 10 km. IRIG-B time code generated by GPS receiver (Hakusan LS-20K) was selected. The time error of GPS receiver is within ±10 μs in order to achieve the necessary geo-location accuracy.

A data sampling rate is important not only for geo-location of lightning but also for investigation of VLF sferic characteristics. The system of sampling frequency with 83.3 kHz create a data file for the time period of 46 seconds per minute (75%). The output signals from the main-amplifier and GPS receiver are digitally and simultaneously sampled using A/D board (Contec AD16-16U(PCI)EV).

2.2   VLF lightning observation network

A continuous recording of waveforms in the frequency range of 2 kHz – 35 kHz at three stations in Kanto region in the range of 150 km from Tokyo, Japan, has been carried out for the first time. Kanto region is one of the best location to investigate the relationship between lightning activity and meteorological parameters in the world because of the dense meteorological observations and a flat stretch of land. The radar beam is shielded due to mountains. The observation system at three sites has been operated since May 15, 2013. The data obtained at Yamanashi site was analyzed in this thesis.

Figure 2.13 shows a position of existing meteorological observation sites and VLF observation sites. The three VLF sites shown as red star in Figure 2.13 were selected so as to surround the capital. Yamanashi site (35.669°N, 138.581°E) is located at Yamanashi prefectural science center, Kofu, Yamanashi, Oami (35.503°N, 140.366°E) is located at Oami-shirasato, Chiba and Maebashi site (36.431°N, 139.043°E) is located at are Gunma University, Maebashi, Gunma. Figure 2.14 and Figure 2.15 show an external view of the antenna and the data recording system of Maebashi site, respectively. The black square in Figure 2.13 indicates AMeDAS (Automated Meteorological Data Acquisition System) sites operated by JMA (Japan Meteorological Agency). There are 128 AMeDAS sites in the area. The squares in green and yellow are meteorological C-band radar site and X-band radar sites, respectively. The JMA Tokyo C-band radar (35.8567°N, 139.9625°E) data was analyzed in this thesis.
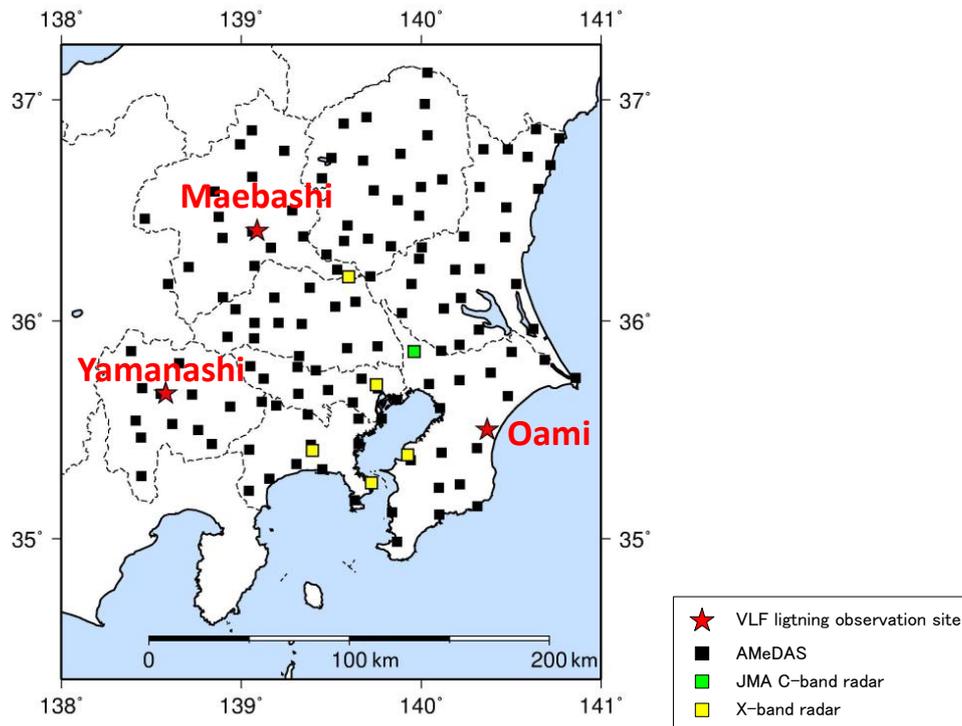
Figure 2.13 Position of existing meteorological observation and VLF observation sites. The red star is the VLF lightning observation sites. The squares in black are the AMeDAS sites, green square is the meteorological C-band radar and the yellow squares are the meteorological X-band radar site.

Figure 2.14. External view of the antenna of Maebashi site.

Figure 2.15. External view of the data recording system of Maebashi site.

2.3 ELF measurement system

In order to observe global lightning activities with ELF electromagnetic waves, continuous recording of ELF waves has been carried out at three observation sites; Syowa (69.018˚S, 39.506˚E), Antarctica since 2000, Onagawa (38.433°N, 141.483°E), Japan since 2001, Esrange (67.9˚N, 21.1˚E), Sweden since 2003 and Santa Cruz (122.214°W, 37.116°N), U.S.A. since 2006 [*Sato et al.*, 2008; *Yamashita et al.*, 2012]. In this thesis, the data obtained at Onagawa site was analyzed to estimate the lightning magnitudes.

The ELF observation system consists of search coil magnetometers, a main amplifier and a data recording system. Figure 2.16 and Figure 2.17 show a schematic diagram of the ELF observation system and a view of the ELF magnetic search-coil antenna, respectively. The system at Onagawa site has been operated with the frequency range of 1 Hz – 400 Hz. Output signals from main–amplifier and IRIG-E time code

signals form the GPS receiver are digitally sampled simultaneously with sampling
frequency 10 kHz [*Sato*, 2004; *Sato et al.*, 2013].
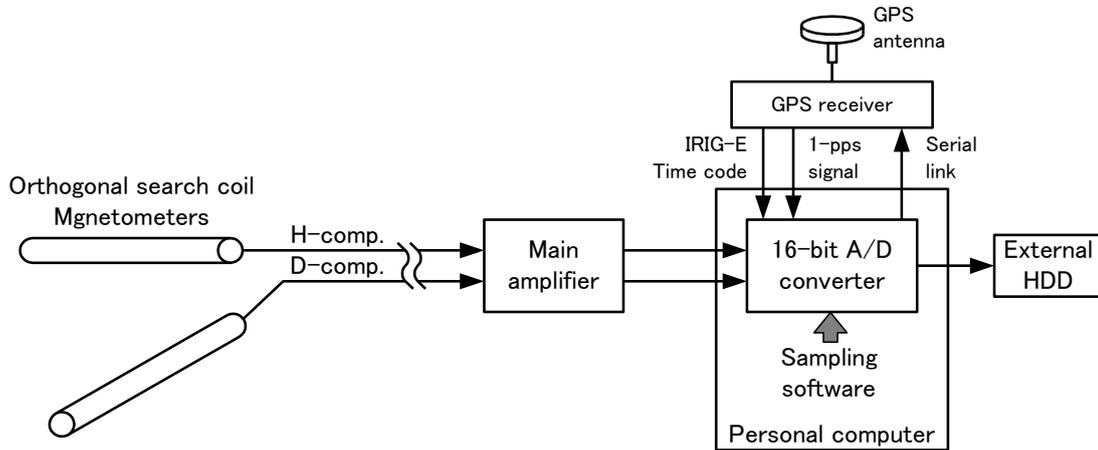
Figure 2.16. Schematic diagram of the ELF observation system.

Figure 2.17. View of the magnetic search-coil antenna [*Sato*, 2004].

Chapter 3

Estimation of lightning magnitudes

3.1 Introduction

The electromagnetic fields of VLF/LF are produced by the lightning return strokes. Especially, the LF band is used to estimate the peak current intensity of the return strokes. Previous studies have developed the return stroke models which describe the electric and magnetic fields waveform generated by the return stroke at different distance, such as transmission line model [*Uman et al.*, 1975; *Thottappillil and Uman*, 1993; *Rakov and Uman*, 1998]. Figure 3.1 shows a schematic diagram of lightning current. Since the observation of the VLF band whose waveform is detectable at far distance than that of the LF band also has sensitivity for the return stroke, some studies estimated peak current form the VLF waveform [*Said et al.*, 2010; *Hutchins et al.*, 2012; *Yanagi*, 2012].

On the other hand, CMC is estimated by the observation of the electromagnetic wave radiated by CG lightning in the range of the ELF band. As Figure 3.1 shows, the ELF band has high sensitivity for the lightning continuing current which flow continuously for the time period of few millisecond – hundreds of millisecond after the lightning return stroke. The amount of charge neutralized by the continuing current is larger than that of the return stroke in the presence of the continuing current. Therefore, the observation of the ELF band is suitable to estimate a huge CG lightning with more than a few hundreds of C·km. The negative CG lightning (–CG) accounts for 90 % or more of CG except in winter in Japan. Most of –CG is smaller CMC than 100 C·km [*Cummer et al.*, 2013], because 40 % of –CG is not accompanied with the continuing

[*Medeiros and Saba*, 2012]. In order to estimate the small CMC of –CG without the continuing current, the observation of the VLF radiowaves radiated by the return stroke which has a time constant from a few tens of microsecond to a few hundreds of microsecond is required.
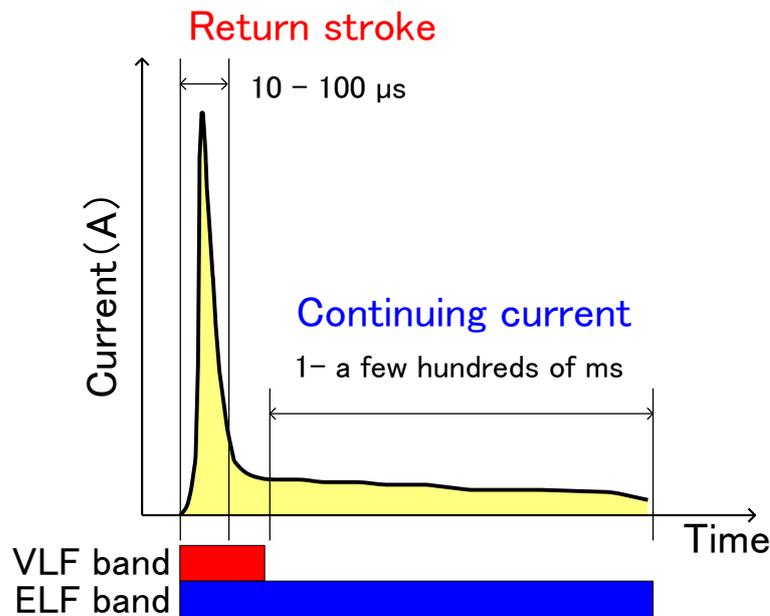
Figure 3.1. Schematic diagram of lightning current.

The estimation method of CMC is roughly classified into two ways, namely, the sferic analysis [*Cummer and Inan*, 1997; *Cummer and Inan*, 2000] and the Schumann resonance analysis [*Hung et al*. 1999; *Sato et al*., 2008]. Since these methods based on the propagation characteristic of ELF electromagnetic waves, they cannot be directly applicable to estimate CMC in the VLF band because of different propagation characteristic.

Cummer [2000] and *Hu and Cummer* [2006] developed a full-wave two-dimensional cylindrical finite-difference time-domain (FDTD) model for the lightning-generated electromagnetic field simulations in the ELF/VLF band. The FDTD method is a numerical analysis technique for the calculation of electric and magnetic field. The time-dependent Maxwell's equations are discretized using central-difference approximations to the space and time partial derivatives. The partial derivatives are computed sequentially. Fitting this simulated lightning current to the observed

waveform, the CMC can be estimated. However, it is difficult to estimate CMC in a short time a for mass CG lightning, because it takes long calculation time with personal computer.

The skywave reflected by the ionosphere overlaps the groundwave (direct wave). Figure 3.2 shows simulated vertical electric field waveforms in the VLF range at different distance [*Haddad et al.*, 2012]. The first skywave overlaps the groundwave after 170–250 microsecond from time of arrival of return stroke at distance less than 200 km from observation site. In order to estimate CMC from the groundwave, removal of influence of the skywave is required. In order to realize the application to short-term meteorological forecast, the method of estimation of CMC in a short time for with high detection efficiency is important. The methods of analysis to estimate impulsive charge moment change and peak current form the VLF waveform are established in the present study.
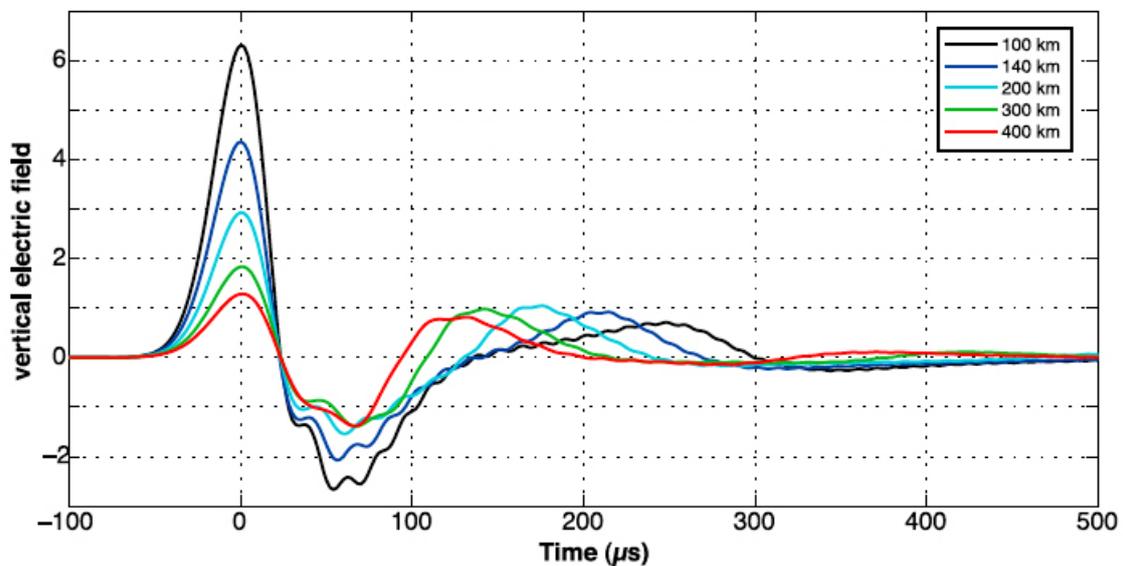
Figure 3.2. Simulated vertical electric field waveform in the VLF range at different distance. The reflection altitude is assumed at 73 km, daytime [*Haddad et al.*, 2012].

3.2   Data and methodology

The electric field waveforms was analyzed in order to estimate the peak current and impulsive charge moment change (iCMC). In this study, iCMC is defined as CMC estimated from the electric field waveform with a duration of 1 ms or less. In this section, the used data, and method of estimation of peak current and iCMC are described.

3.2.1   Data description

The four days where lightning occurred in Kanto region from May 2013 to August 2013 were selected. The area of analysis is confined from 34.5°N to 37.2°N and 138°E to 141°E, and in the range of 50–200 km from Yamanashi site (Figure 3.3). In order to estimate iCMC from electric field waveform, the lightning events observed at distance more than 50 km from the VLF lightning observation site were analyzed, since the distance must be far enough compared to one sixth of wave length at 2 kHz (cutoff frequency). In addition, upper limit of the distance from the observation site is set at 200 km where the skywave can be separated from the groundwave.

In order to identify the events of CG lightning, JLDN (Japan Lightning Detection Network) lightning data was used. Information of location, occurrence time, peak current, and discharge type (CG or IC) in JLDN data are used. A median of geo-location accuracy of JLDN is reported as 1.08 km [*Ishii et al*., 2001b], and the detection efficiency of –CG is more than 90 %. Figure 3.3 shows the area of analysis and lightning locations detected by JLDN of 4 days. The crosses in Figure 3.3 show the lightning location on May 16, 2013 (red), June 22, 2013 (orange), July 11, 2013 (green), and August 11, 2013 (blue). The black triangles show the VLF lightning observation site. The small and large circles indicate 50 km and 200 km distance from Yamanashi site, respectively. Table 3.1 shows the number of CG lightning flashes detected by JLDN of each day. Total number of CGs for 4 days is 10,606 flashes. 7,475 events of VLF data

are matched with the events of JLDN data. The result is explained in section 3.3 in detail.
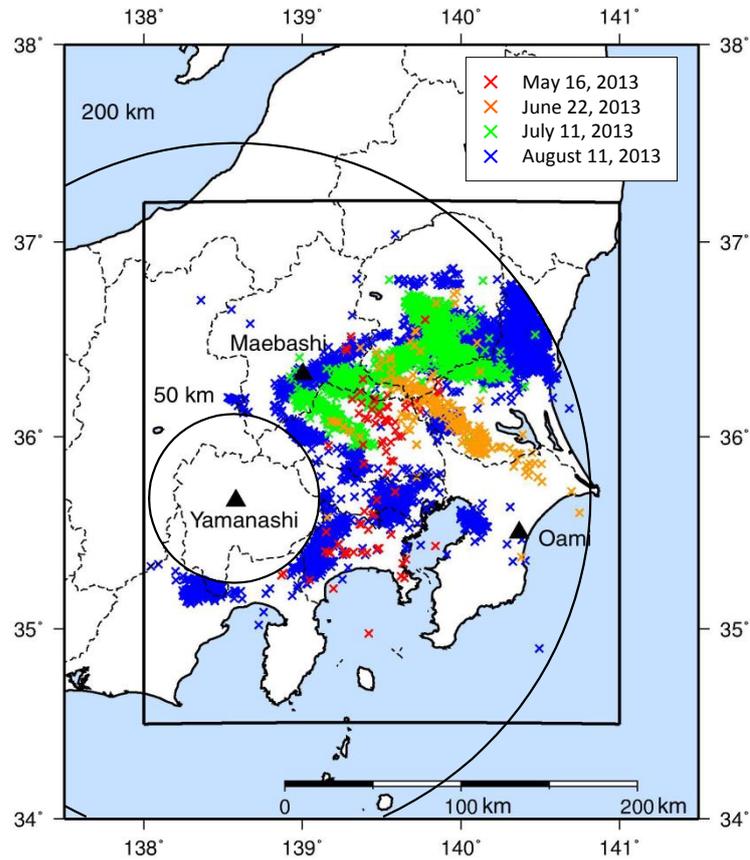
Figure 3.3. Area of analysis and lightning location of each day.

Table 3.1. Number of CG lightning flashes detected by JLDN

Day	Hour (JST)	Number of –CG	Number of +CG
May 16, 2013	14:00 – 22:00	49	32
June 22, 2013	10:00 – 20:00	184	23
July 11, 2013	13:30 – 20:00	2,439	17
August 11, 2013	12:00 – 21:00	7,688	174

3.2.2   Concept of estimation of iCMC

An electric field caused by electrical charges and their motions is expressed as the following polynomial equation. The first term, second term and third term are the electrostatic term, induction term, and radiation term, respectively. As equation (3.2) shows, the radiation term is proportional to derivation of the current moment (I_M).

$$4\pi\varepsilon_0 E \approx \frac{M_0 - M}{r^3} + \frac{1}{cr^2}\frac{dM}{dt} + \frac{1}{c^2 r}\frac{d^2 M}{dt^2} \tag{3.1}$$

$$\frac{1}{c^2 r}\frac{d^2 M}{dt^2} \propto \frac{dI_M}{dt} \tag{3.2}$$

where ε_0 is the dielectric constant of vacuum, c is the speed of light, r is the distance from the charge, M is the charge moment change (C·km), M_0 is the charge moment of the thundercloud.

Equation (3.1) and (3.2) indicate that the current moment (I_M) is obtained by integrating the electric field waveform with time. In addition, iCMC is obtained by integrating current moment with time. Figure 3.4 shows a schematic diagram of a concept of iCMC estimation in this study. The blue waveform in Figure 3.4 is observed the electric field waveform which corresponds to the radiation term of electric field. T_0 is the time of start of the waveform. T_1 is the time of peak amplitude of the waveform. T_p is the time of first zero-crossing of the waveform. T_2 is the time of first negative peak of the waveform. T_3 is the time of second zero-crossing of the waveform. It is assumed that the lightning current moment decays to zero at T_3. The current moment (red waveform) is obtained by integrating the blue waveform from T_0 to T_3. When the observed waveform reaches its first zero-crossing point (T_p), current moment reaches its peak at the time. iCMC is estimated by integrating the current moment (red waveform) from T_0 to T_3.

However, it is not simple to estimate iCMC in actuality. When observed waveform is integrated from T_0 to T_3, integrated waveform is not equal to zero at T_3. It is presumed that the discharge channels of lightning extend intricately, and the skywave overlaps the groundwave. In order to estimate the current moment, T_3 is determined

removing the influence of the skywave, and it is assumed that the current moment exponentially decays from T_p to T_3.
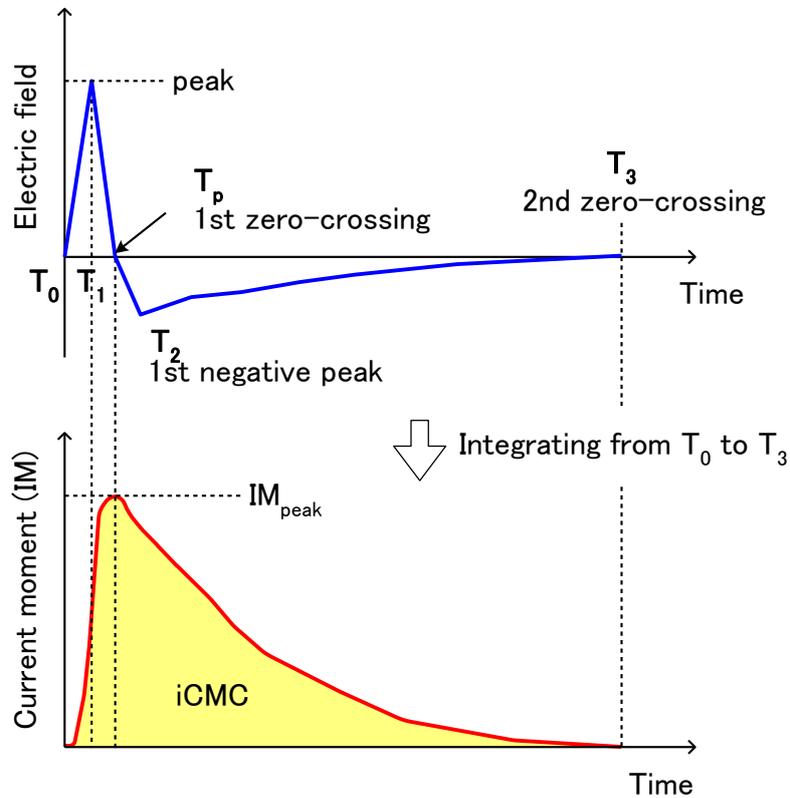
Figure 3.4. Schematic diagram of a concept of iCMC estimation.

Figure 3.5 shows a flow diagram of the estimation of iCMC. First, obtained VLF lightning waveforms (sferics) are identified based on JLDN as shown in section 3.2.3. The VLF sferics are reconstructed using gain and phase characteristics as section 3.2.4 shows. The peak current of lightning is estimated by the relationship between the peak amplitude of VLF sferic and JLDN peak current as shown in section 3.2.5. The skywave which overlaps the groundwave of the VLF sferics is removed as shown in section 3.2.6. The current moment and iCMC are estimated as shown in section 3.2.7. Finally, in order to estimate iCMC with a duration of 1 ms or less, integrating interval is corrected using the VLF and ELF waveform as section 3.2.8 shows.
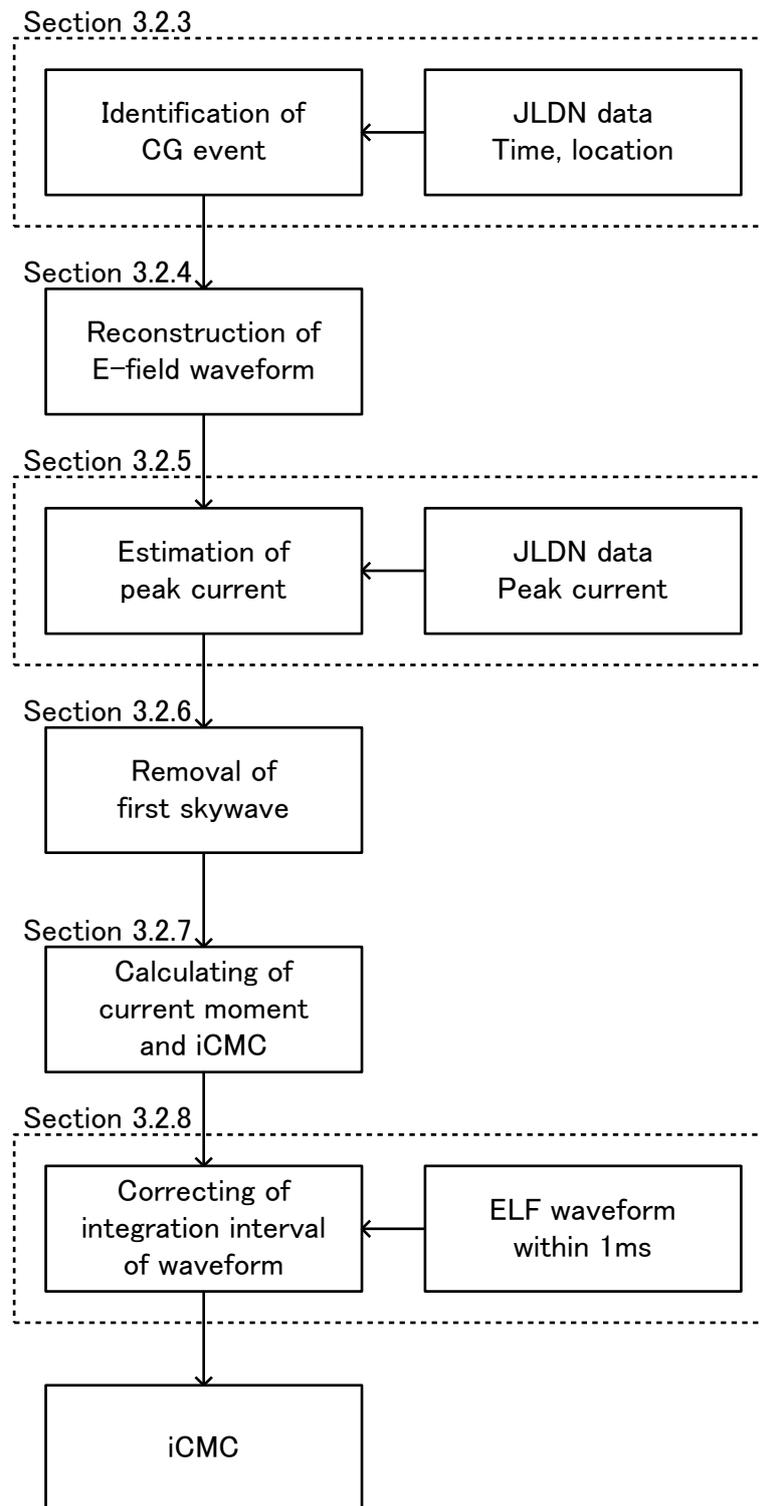
Figure 3.5. Flow diagram of the estimation of iCMC.

3.2.3   Identification of event of cloud to ground lightning

The method of identification of the CG events is described in this section. The occurrence time (T_0) and the location of CGs are obtained by the JLDN lightning data. The distance (D_1) between the lightning location and Yamanashi site is calculated using the the location (latitude, longitude) of JLDN data. By assuming that the VLF electromagnetic wave propagate in the atmosphere at the speed of light, propagation time (dT) for D_1 is calculated. An arrival time (T_a) at Yamanashi site can be estimated by T_0 plus dT. The peak of transient waveforms is searched for before and after T_a with 180 microsecond. If the polarity of the JLDN lightning data and the VLF waveform are consistent and the absolute value of amplitude of the waveform with greater than or equal to 0.05 V, the VLF waveform is identified as the CG event. The time of peak of the waveform is defined as T_1. Figure 3.6 shows an example of identified waveform of the electric field of Yamanashi site with this method. The blue solid line in Figure 3.6 indicates the time of peak of the waveform (T_1), and the red solid line indicates estimated time of arrival (T_a).
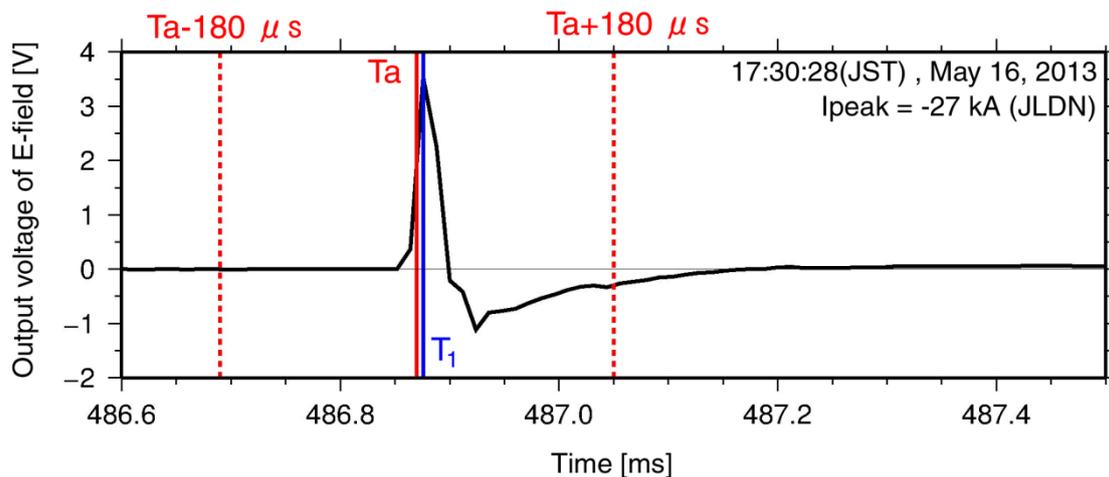
Figure 3.6. Example of identified waveform of the electric field of Yamanashi site.

3.2.4   Reconstruction of electric field waveform

The observation system developed in this study has characteristics of gain and phase as shown in Figure 2.6 and Figure 2.7. In order to estimate the peak current and iCMC using the amplitude of the electric field waveform and its wave shape, the original waveform has to be reconstructed with characteristics of gain and phase. The procedure of the reconstruction of the waveform is described below.

According to *Huang et al.*, [2011], following equation holds for any signal waveform.

$$\Phi_{in}(t) = \frac{1}{\sqrt{2\pi}} \int_{-\infty}^{\infty} A_{in}(\omega) e^{i\omega t} d\omega \tag{3.3}$$

where t is the time, $A_{in}(\omega)$ is the power spectrum of $\Phi_{in}(t)$, ω is the angular frequency. When a signal pass the system with instrumental function, the intensity and phase of signal are varied. The output signal is described as

$$\Phi_{out}(t) = \frac{1}{\sqrt{2\pi}} \int_{-\infty}^{\infty} A_{in}(\omega) M_{filter}(\omega) e^{i\left(\omega t + \Phi_{filter}(\omega)\right)} d\omega \tag{3.4}$$

where $M_{filter}(\omega)$ is the gain characteristics, $\Phi_{filter}(\omega)$ is the phase characteristics. The output signal is also described as following equation.

$$\Phi_{out}(t) = \frac{1}{\sqrt{2\pi}} \int_{-\infty}^{\infty} A_{out}(\omega) e^{i\omega t} dt \tag{3.5}$$

In fact, the following relation is obtained.

$$A_{out}(\omega) = A_{in}(\omega) M_{filter}(\omega) e^{i\varphi_{filter}(\omega)} d\omega \tag{3.6}$$

Equation (3.6) is also described as below.

$$F\{\Phi_{in}(t)\} = \frac{e^{-i\varphi_{filter}(\omega)}}{M_{filter}(\omega)} F\{\Phi_{out}(t)\} \tag{3.7}$$

By computing the inverse Fourier transform of equation (3.7), the input signal waveform is obtained.

$$\Phi_{in}(t) = F^{-1} \left\{ \frac{e^{-i\varphi_{filter}(\omega)}}{M_{filter}(\omega)} F\{\Phi_{out}(t)\} \right\} \tag{3.8}$$

The output signal of electric field is reconstructed using the gain and phase characteristics shown in Figure 2.6 and Figure 2.7. The electric field waveform is extracted in T_1 with 100 millisecond before and after. The waveform is reconstructed in 2 kHz –35 kHz, approximately cutoff frequency. Figure 3.7 shows a verification result of the gain and phase reconstruction of sin wave at 5 kHz. The waveforms indicated in blue and in red are the input signal and the reconstructed signal, respectively. The reconstruction of waveform observed at Yamanashi site is shown in Figure 3.8. The obtained waveform sifted by 24 µs after by the correction of the phase characteristic. This result has an effect on determination of occurrence time and location of CG lightning. The occurrence time of CG lightning can be determined accurately by the correcting.
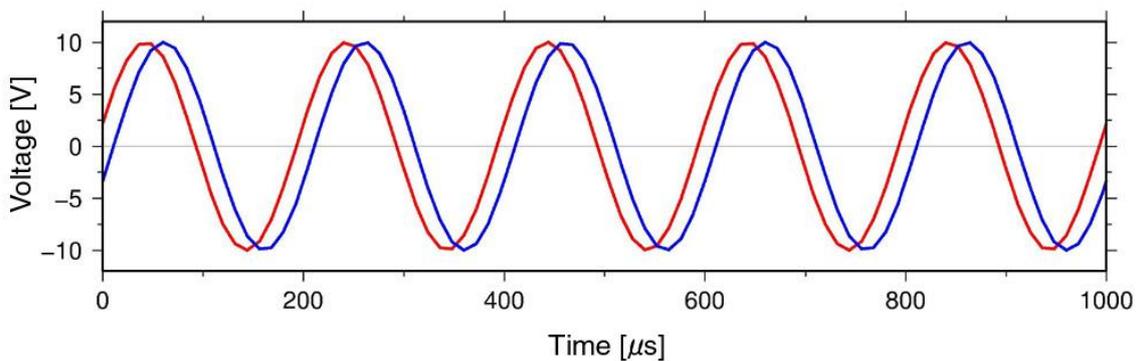
Figure 3.7. Verification result of the gain and phase reconstruction of sin wave at 5 kHz. The waveforms indicated in blue and in red are input signal and reconstructed signal, respectively.
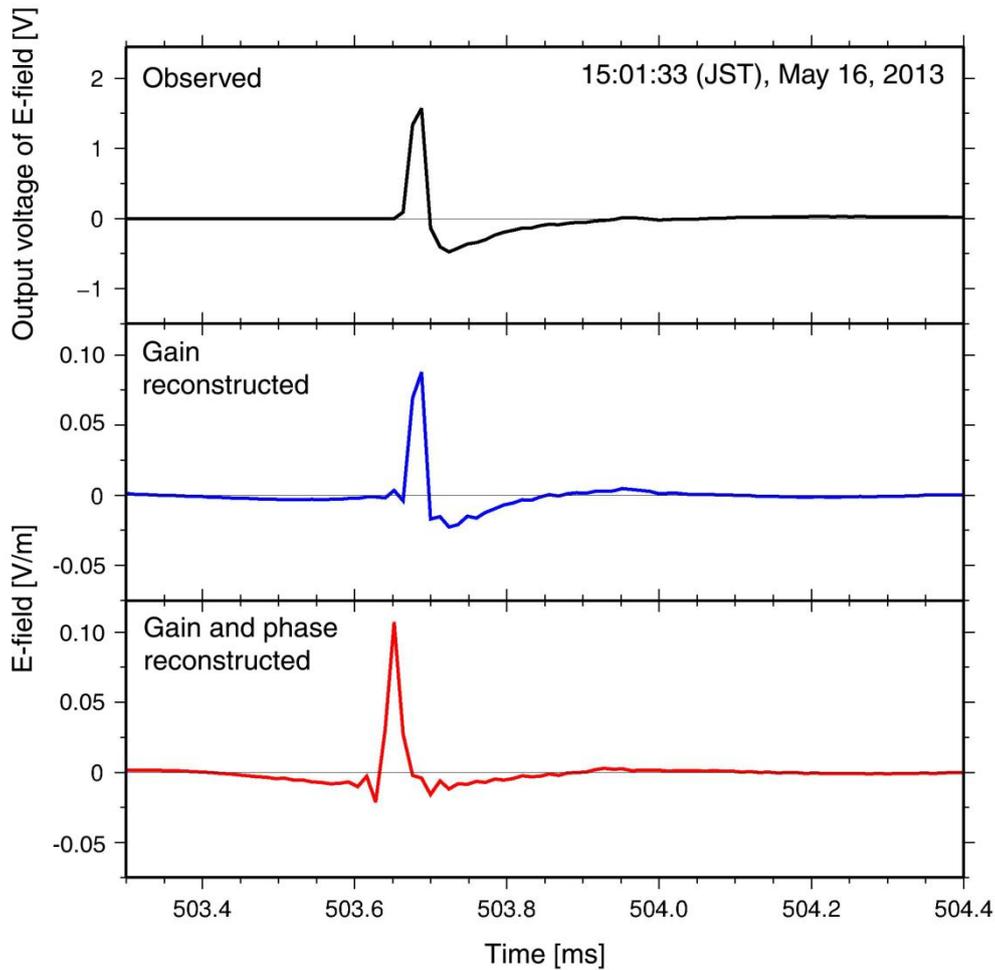
Figure 3.8. Example of reconstruction of the waveform observed at Yamanashi site.

3.2.5   Estimation of peak current

In order to estimate the peak current of lightning, the relation between the normalized amplitude of the electric field waveform and peak current of JLDN data was investigated. According to *Yanagi* [2012], there is a good correlation between the amplitude of VLF ferics normalized for distance and the peak current of JLDN data for the events which occurred within 1,400 km from observation site. In the method proposed by *Yanagi* [2012], the phase characteristics of amplifier is not considered, resulting in problems for the events within a few hundreds of km. Therefore, the method

proposed by *Yanagi* [2012] is improved in this study. The method of estimation of the peak current is described below.

The distance (D_1) (km) between the lightning location and Yamanashi site is calculated using the lightning location of JLDN data. By assuming that the peak amplitude of electric field (E_{peak}) is inversely proportional to the distance, the normalized peak amplitude at 50 km (V_n) is described as the following equation. A radiation term of electric field dominates at distance more than 50 km in the VLF band.

$$V_n = \frac{D_1}{50} E_{peak} \tag{3.9}$$

The relationship between V_n and the JLDN peak current of −CG and +CG is examined, respectively. The relational expression for the estimation of the peak current is obtained by the comparison between V_n and the JLDN peak current.

A result of the comparison in the case of −CG is shown in Figure 3.9. There are three panels of scatter plot of V_n versus the JLDN peak current. The left, center and right panels indicate the relationship between normalized amplitude and peak current for observed, gain-reconstructed, and gain and phase reconstructed data, respectively. All of them show a good correlation between V_n and the JLDN peak current with high determination coefficient (R^2), more than 0.79. The three fitted linear functions have a almost same inclination and intercept. The linear function for the gain- and phase-reconstructed data are used for the estimation of peak current of −CG like as for the estimation of iCMC.

$$I_{peak} = -58V_n - 9.2 \text{ [kA]} \tag{3.10}$$

where V_n is the normalized peak amplitude at 50 km (V/m).

Similarly, a result of the comparison in the case of +CG is shown in Figure 3.10. The left, center and right panels indicate the relationship between normalized amplitude and the peak current for observed, gain-reconstructed, and gain- and phase-reconstructed data, respectively. All of them also show a good correlation between V_n and the peak current of JLDN data with high determination coefficient,

more than 0.81. The following equation was used for estimation of the peak current of +CG.

$$I_{peak} = -438V_n + 5.6 \text{ [kA]} \tag{3.11}$$
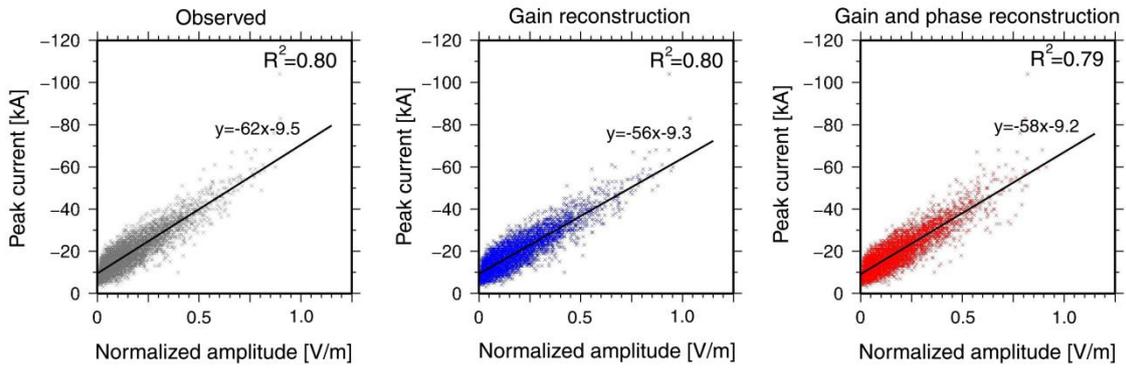
Figure 3.9. Three scatter plots of the normalized amplitude (V_n) versus the peak current of JLDN data (I_{peak}) in the case of –CG. Left panel: observed E-field, center panel: gain reconstructed E-field, right panel: gain and phase reconstructed E-field.
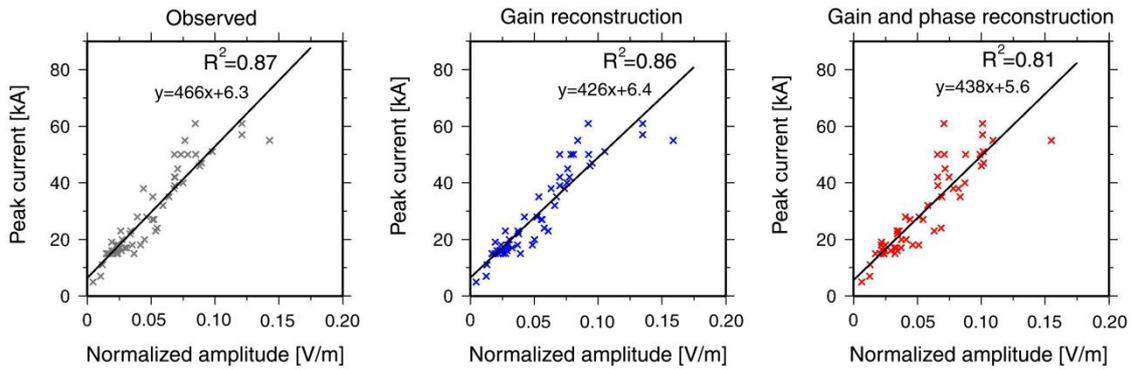
Figure 3.10. Three scatter plots of the normalized amplitude (V_n) versus the peak current of JLDN data (I_{peak}) in the case of +CG. Left panel: observed E-field, center panel: gain reconstructed E-field, right panel: gain and phase reconstructed E-field.

3.2.6   Removing an influence of first skywave

The purpose of this section is to remove the influence of the skywave for the duration time of the electric field waveform. The time of arrival of the first skywave vary depending on the distance from the observation site. The altitude of reflection is assumed to be 70 km in order to calculate the time of arrival of the first skywave.

Figure 3.11 shows a schematic procedure of removing the first skywave from the reconstructed waveform of –CG. The red solid line in Figure 3.11 indicates the reconstructed electric field waveform. T_2 is the time of first negative peak of the reconstructed waveform. T_R is a time of arrival of the first skywave when the altitude is assumed of 70 km. T_{2s} is a time 12 microsecond before T_R. Assuming that the source current moment decay gradually, linear approximation is fitted to the reconstructed waveform from T_2 and T_{2s} (green dashed line in Figure 3.11). The reconstructed waveform was replaced with the linear approximation after T_2. The time of second zero crossing of the corrected waveform is defined as T_3.

The altitude of reflection in daytime (70 km) is typically lower than that in nighttime by about 10–20 km [*Smith et al.*, 2004]. If the altitude of reflection is assumed to be larger than (nighttime), time of arrival of skywave (T_R) is delayed, resulting in less overlapping with ground wave. Therefore, the assumed altitude of reflection of 70 km is the worst case of overlap between ground wave and skywave.
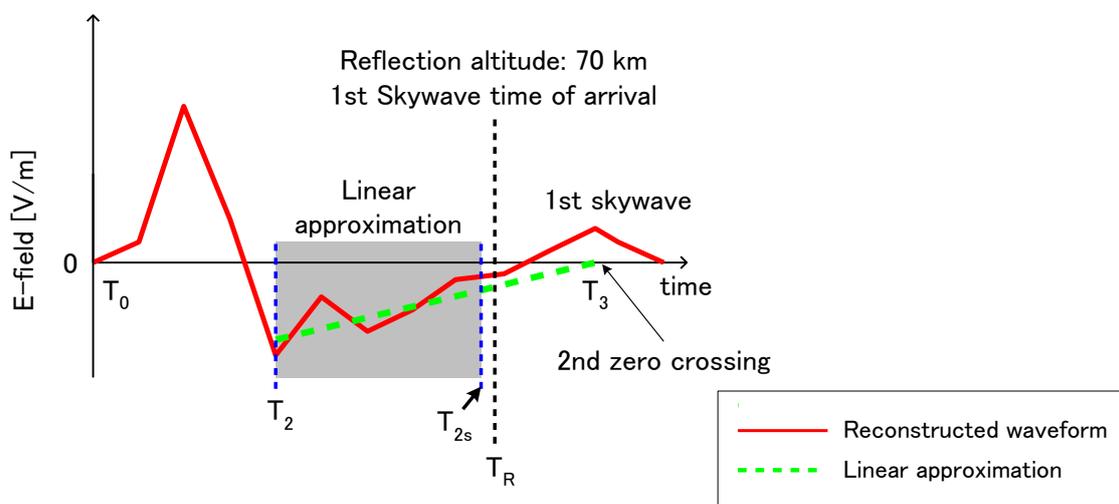
Figure 3.11. Schematic diagram of removing the first skywave from the reconstructed waveform.
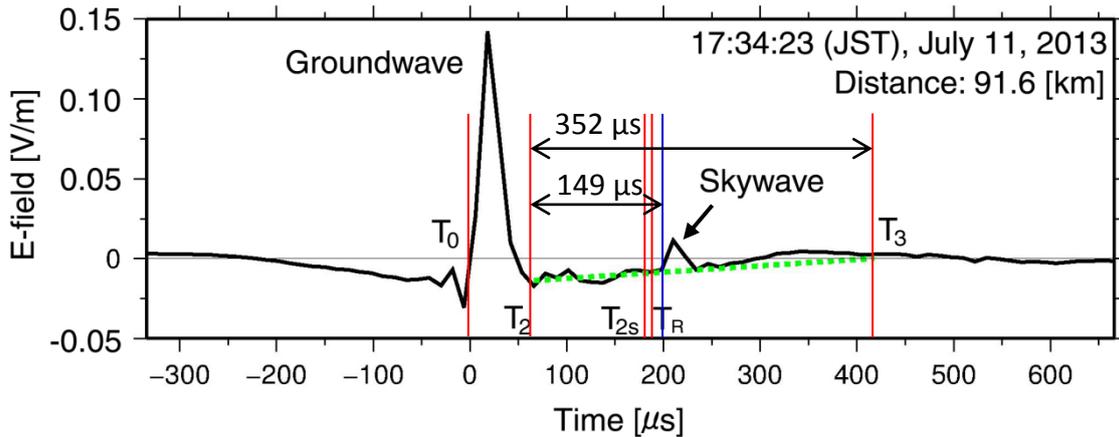
Figure 3.12. Example of reconstructed waveform and calculated T_R, T_{2s} and T_3.

Figure 3.12 shows an example of the reconstructed waveform and calculated T_R, T_{2s} and T_3. The black line is the electric field waveform observed at 17:34:23 (JST), July 11, 2013. The waveform has two positive peaks at 20 μs and 220 μs. The first positive peak is caused by groundwave, and second positive peak by the skywave. The green dashed line is a linear curve fitted for a period between T_2 and T_{2s}. If the reconstructed waveform is not corrected by this method, the time of second zero crossing from T_2 is 149 microsecond. The result of this case, the time of second zero crossing (T_3) from T_2 is 352 microsecond.

3.2.7   Calculating current moment and iCMC

In this section, the method for calculating the current moment and iCMC using the reconstructed waveform and T_3 is described. Firstly, relative current moment is calculated by integrating the reconstructed waveform. The relative current moment is converted into the current moment using the estimated peak current. Figure 3.13 shows a schematic diagram for the calculation of the relative current moment.

  (1) The reconstructed waveform is integrated from T_0 to the time of first zero crossing (T_p) in Fugure 3.13. The relative current moment waveform is obtained until its peak.

(2) It is assumed that the current moment decays exponentially from the peak of the relative current moment (T_p) to T_3 in Figure 3.13. The relational equation is described as

$$IM(t) = e^{\frac{-\alpha t}{(T3-Tp)}} \, [\text{kA} \cdot \text{km}] \tag{3.12}$$

where *IM* is the relative current moment after T_p, *t* is a time from T_p, and α is the attenuation coefficient. Figure 3.14 shows the time variation of the current moment with different α of the equation (3.12). In the case of $\alpha=1$, the value of the current moment at T_3 becomes approximately –40 kA·km. On the other hand, in the case of $\alpha=7$, the value of the current moment becomes approximately zero at 300 microsecond earlier than T_3. 5 was selected as the value of α, so that the current moment becomes approximately zero at T_3.
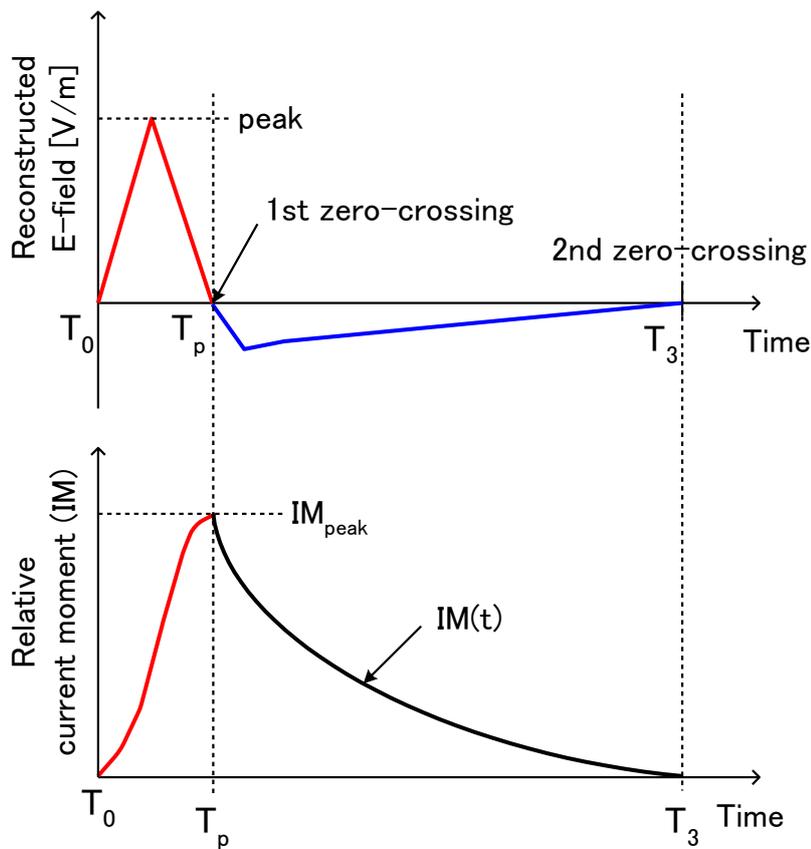
Figure 3.13. Schematic diagram of calculating a relative current moment.
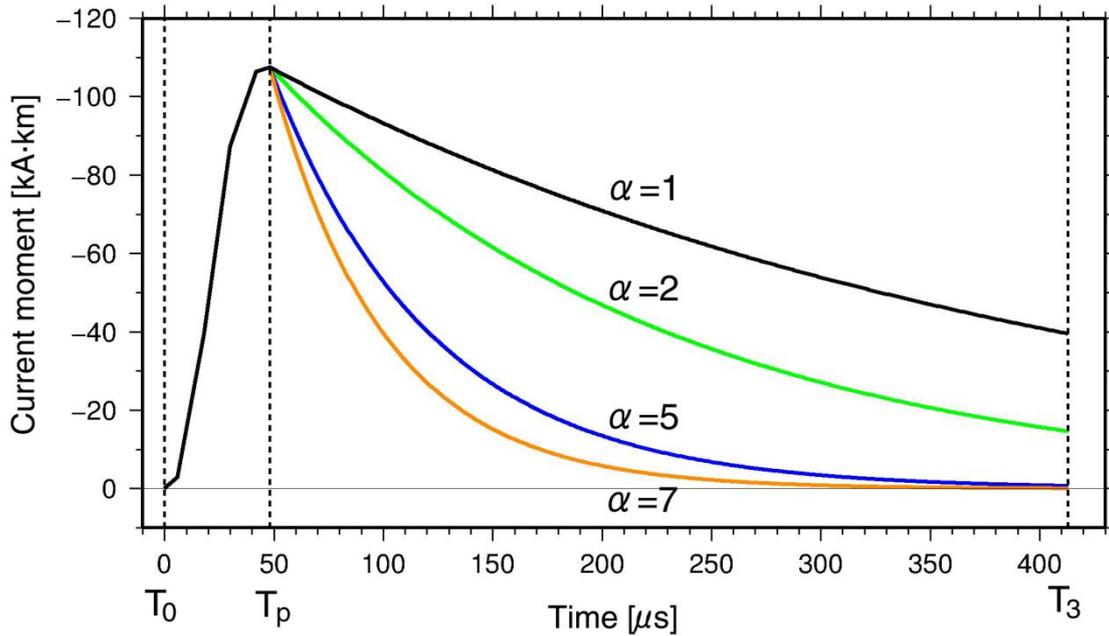
Figure 3.14. The time variation of current moment by different time constant.

The relative current moment is converted to the current moment (kA·km) using the peak current and the vertical length of discharge channel (discharge length) at the time of peak amplitude of the reconstructed waveform (T_1). Figure 3.15 shows a flow diagram of converting the relative current moment to the absolute value of current moment. The average lightning current between T_0 and T_1 is calculated. The current moment at T_1 is estimated by its discharge length and the average lightning current. The ratio of the relative current moment at T_1 to the current moment at T_1 is calculated, the relative current moment between T_0 and T_3 is converted to the current moment by the ratio.
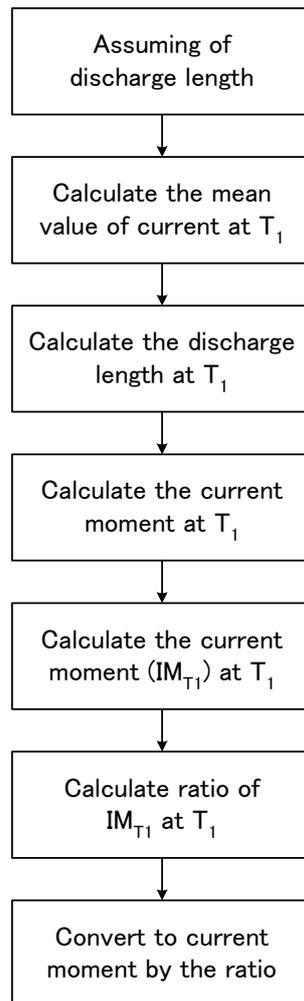
Figure 3.15. Flow diagram of converting the relative current moment to the absolute value of current moment.

In order to calculate the discharge length that changes every moment, the extension speed of return stroke is assumed as c/2 (c: speed of light, 3.0×10^8 m/s) [*Rakov*, 2007, *Baba and Rakov*, 2007], and the upper end of discharge length is assumed as 5 km. Since the thermal layer of −10 ˚C is distributed in the range of 5-7 km in summer in Japan, the upper end of discharge is assumed as 5 km. The black line in Figure 3.16 shows the time variation of the discharge length. The discharge length is assumed to increase until 5 km (33.3 µs) at the constant speed, and to be maintained as 5 km after 33.3 µs. The current moment (red line in Figure 3.16) is calculated by multiplying the current (blue line shown in Figure 3.16) by the discharge length (black line shown in Figure 3.16) at the moment.
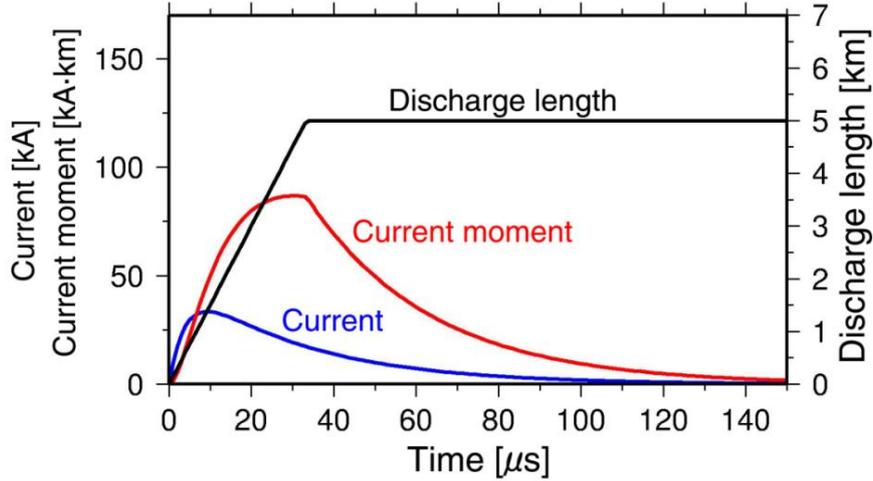
Figure 3.16. Relationship between the discharge length and the current moment.

In order to convert the relative current moment to the absolute value of current moment [kA·km], it is assumed that the peak current corresponds to the peak amplitude of the reconstructed waveform according to the relationship shown in section 3.2.5. In addition, it is assumed that the source current varies rapidly between T_0 and T_1, and that current with mean value flows along the discharge channel at T_1. The mean value is calculated by the following equation.

$$I_{mean} = I_{peak} \times \frac{2}{\pi} \; [\text{kA}] \tag{3.13}$$

where I_{mean} is the mean value of current between T_0 and T_1, I_{peak} is the estimated peak current, and π is the circular constant.

Figure 3.17 shows these assumption and the relationship between peak current and current moment at the time of T_1. The red line in Figure 3.17 shows the current, and the blue line in Figure 3.17 shows the mean value of current between T_0 and T_1. The discharge length at T_1 is calculated as shown in Figure 3.17. The absolute value of current moment at T_1 (IM_{T1}) is estimated by multiplying the discharge length at T_1 by the mean value of current (I_{mean}). The ratio of IM_{T1} to the relative current moment at T_1 is calculated as k. The relative current moment of each point between T_0 and T_3 is multiplied by k, then the absolute value of current moment is obtained.
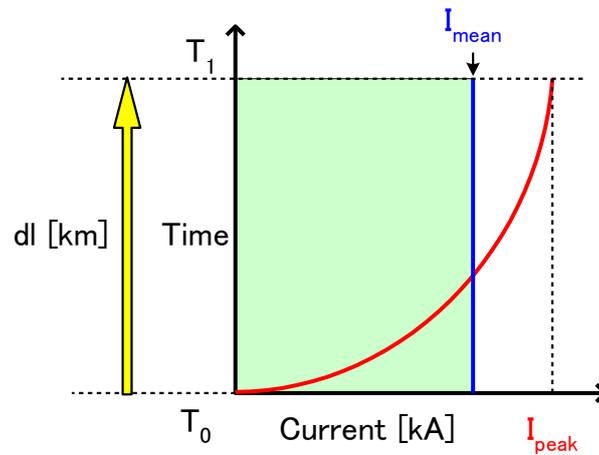
Figure 3.17. Relationship between the peak current and the absolute value of current moment at the time of T_1 (T_{Ipeak}).

Figure 3.18 shows an example of conversion from the relative current moment to the absolute value of current moment between T_0 and T_p. The red line shown in Figure 3.18 is the reconstructed electric field waveform, and the blue line is the estimated current moment. The symbols of red triangle indicate the data points. In this case, the discharge length is calculated as 2.7 km, because the duration between the time between T_0 and T_1 is 18 μs. The current moment at T_1 (IM_{T1}) is calculated as 41.6 kA·km as shown in Figure 3.18. Figure 3.19 shows the whole of result of the same case. As mentioned above, the current moment decay with equation (3.12) between T_p and T_3. The current moment is integrated from T_0 to T_3, then iCMC is obtained.
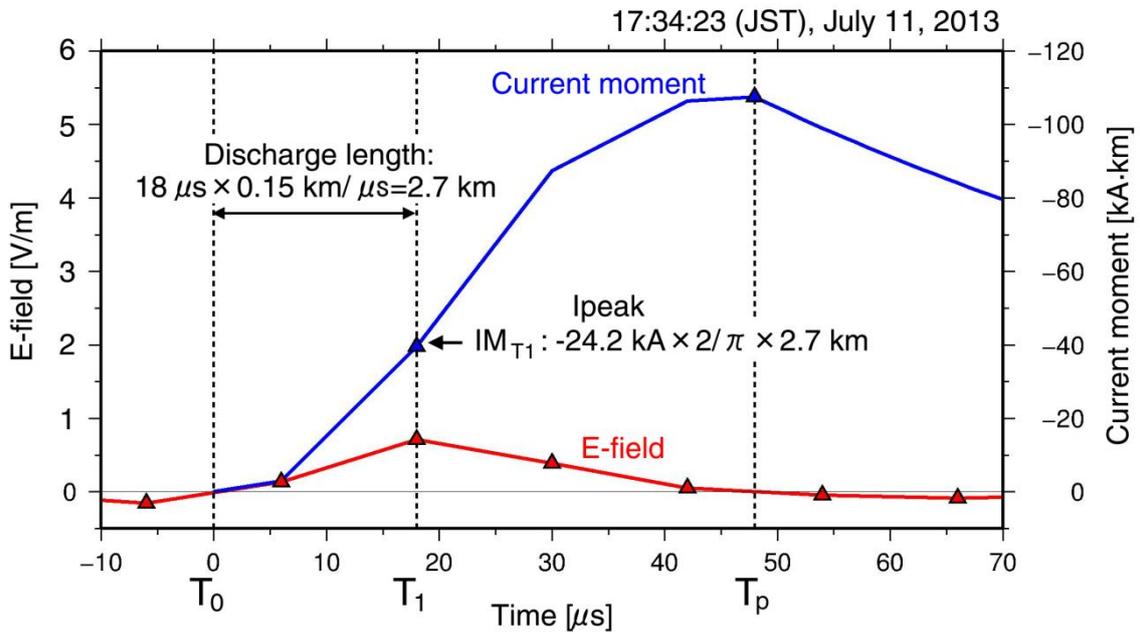
Figure 3.18. Example of conversion from the relative current moment to the absolute value of current moment between T_0 and T_p on 17:34:23 (JST), July 11, 2013. The red line is the reconstructed electric field waveform, and the blue line is the converted current moment. The symbols of red triangle are the data points.
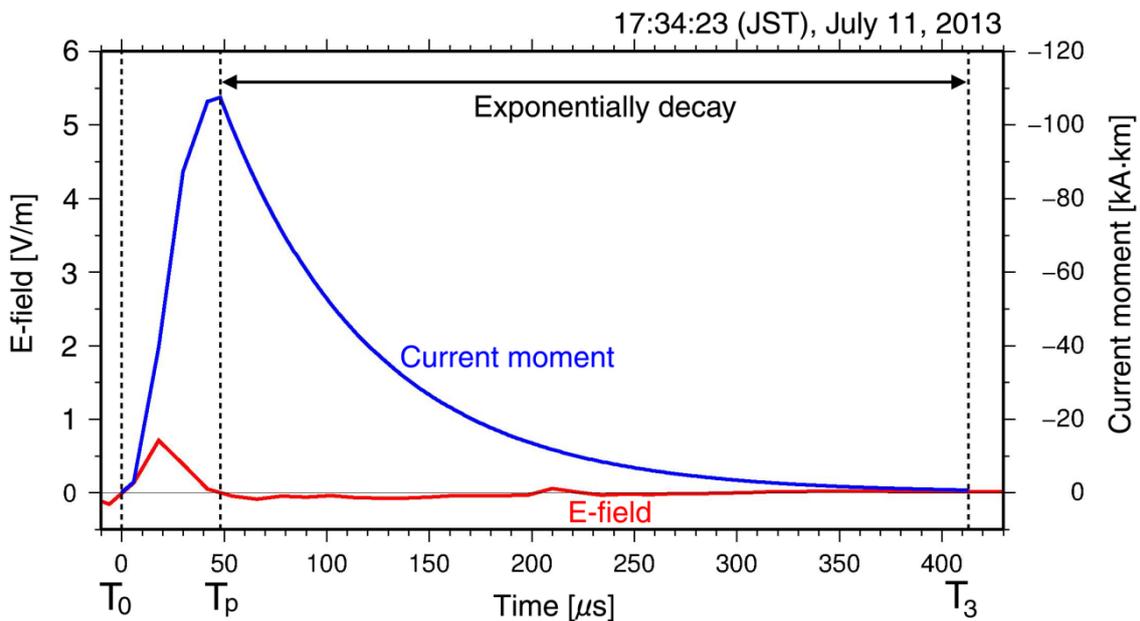
Figure 3.19. Example of conversion from the relative current moment to the absolute value of current moment between T_0 and T_3 on 17:34:23 (JST), July 11, 2013.

3.2.8   Correcting integration interval of waveform

Lightning current is divided into return stroke and continuing current which have time constant, respectively. In the calculation of current moment, VLF observation system has a high sensitivity for the return stroke, which has a time constant shorter than 500 μs. In order to estimate iCMC with a duration of 1 ms or less, the relationship between T_3 and CMC estimated by the ELF wave with a duration of 1 ms was examined.

According to *Sato et al.* [2013], the time variation of the ELF magnetic field with lower cutoff frequency of 400 Hz shows a similar time variation of the lightning current within about 1600 km where the induction term dominates. Figure 3.20 is a schematic diagram showing how to correct the integrated interval of the waveform using the current moment estimated by the ELF wave obtained at Onagawa site. The method is described as following.

(1) Lightning event is identified based on the expected time of arrival at Onagawa site calculated from the lightning location of JLDN data.

(2) The obtained waveform is converted into magnetic flux density [pT] by the reconstruction of gain and phase characteristics.

(3) H_Φ is calculated by the bearing angle of the CG location from the magnetic north.

(4) The lightning current is calculated by the method proposed by *Sato et al.* [2013], assuming a proportionate relationship between magnetic flux density (H_Φ [pT]) and value of current (I_{ELF}). The relational equation is described as

$$I_{ELF}(t) = 0.0442 H_\varphi(t) [\text{kA}] \tag{3.14}$$

where *t* is the time.

(5) Assuming the discharge length of 5 km, ELF current moment is calculated by I_{ELF} multiplied by 5 km. The green waveform in Figure 3.19 is obtained.

(6) CMC estimated by the ELF wave (S2 in Figure 3.19) is integrated between T_0 and 1 ms.

(7) T_4 is calculated using the same method of calculating S1 in section 3.2.7, so that S3 is equal to S2.

The ELF wave was simultaneously recorded at Onagawa site at May 16, 2013. The number of identified ELF waves of –CG was 11. The relationship between T_3 and T_4 for 11 cases was investigated. Figure 3.21 shows a scatter plot of T_3 versus T_4. The black line is linear approximation with $R^2 = 0.78$. T_3 is corrected into T_4 using the following equation.

$$T_4 = 0.94 * T_3 + 171.9 \qquad (3.15)$$

The current moment integrated until 1 ms after onset is defined as iCMC in this study.
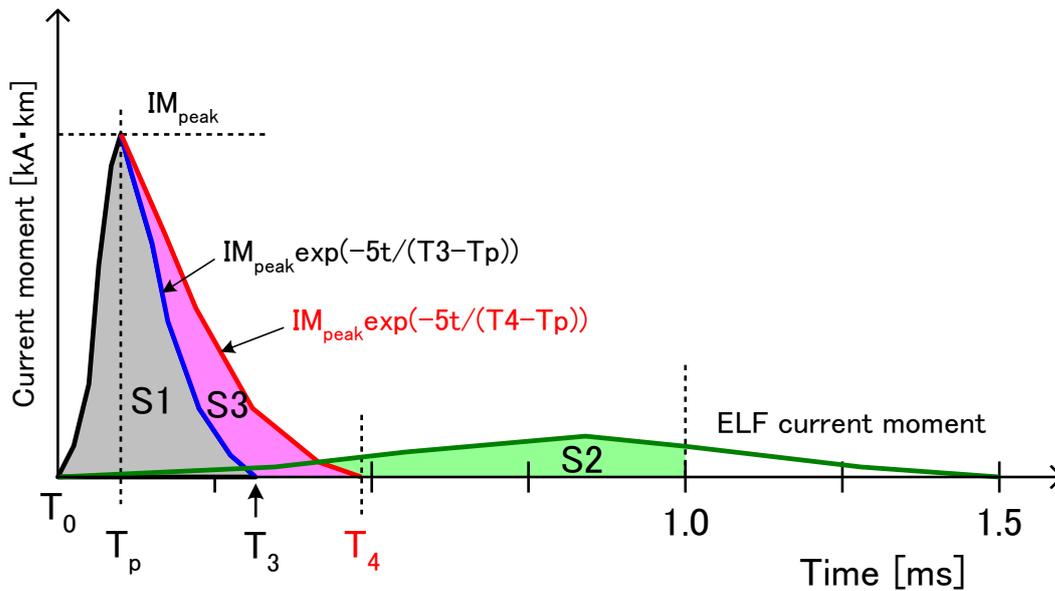
Figure 3.20. Schematic diagram of correcting integration interval of waveform using the current moment estimated by ELF waveform.
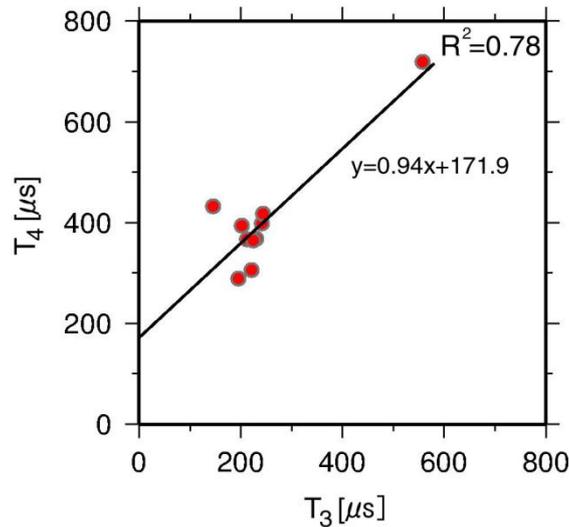
Figure 3.21. Scatter plot of T_3 versus T_4. The black line is linear approximation with $R^2=0.78$.

3.3 Results of estimated lightning magnitudes

The 10,606 VLF sferic events obtained at Yamanashi site at the distance from 50 to 200 km were analyzed. Table 3.2 shows the number of events whose iCMC are estimated. The number of estimated iCMC of −CG and +CG are 7,418 and 57, respectively. The detection efficiency of iCMC of −CG and +CG are 69–82 %, and 19–43 %, respectively. The average of iCMC of −CG and +CG are −6.9 C·km and +12.9 C·km, respectively. iCMC of −CG and +CG range from −69.2 to −1.1 C·km and 2.1 to 45.4 C·km, respectively.

Figure 3.22 shows the distribution of occurrence frequency of the peak current estimated from the VLF data and JLDN. The left panel (a) shows the case of −CG, and right panel (b) shows the case of +CG. The bule line in Fugire 3.22 indicates the distribution of occurrence frequency of the peak current intensity (absolute value of peak current) estimated from VLF data, and the black dashed line indicates that of JLDN. In the case of −CG, the distribution of occurrence frequency of the peak current intensity more than 12 kA estimated from VLF data closely coincides with that of JLDN. The distribution of occurrence frequency of the peak current intensity more than 12 kA indicates that its distribution of occurrence frequency decrease linearly with increase in

peak current intensity on single logarithmic plot. The occurrence frequency of the peak current intensity between 10 kA and 12 kA estimated from VLF data is clearly more than that of JLDN. Peak current intensity could not be estimated for the events with peak current of 10 kA or less. In the case of +CG, it seems that the distribution of occurrence frequency of the peak current estimated from VLF data is similar to that of JLDN.

Table 3.2. The number of events detected and estimated the impulsive charge moment change by the JLDN and Yamanashi site.

	May 16, 2013		Jun. 22, 2013		Jul. 11, 2013		Aug. 11, 2013	
Polarity of CG	–CG	+CG	–CG	+CG	–CG	+CG	–CG	+CG
JLDN	49	32	184	23	2,439	17	7,688	174
iCMC	40	9	138	10	1,926	5	5,314	33
Detection efficiency	82%	28%	75%	43%	79%	29%	69%	19%
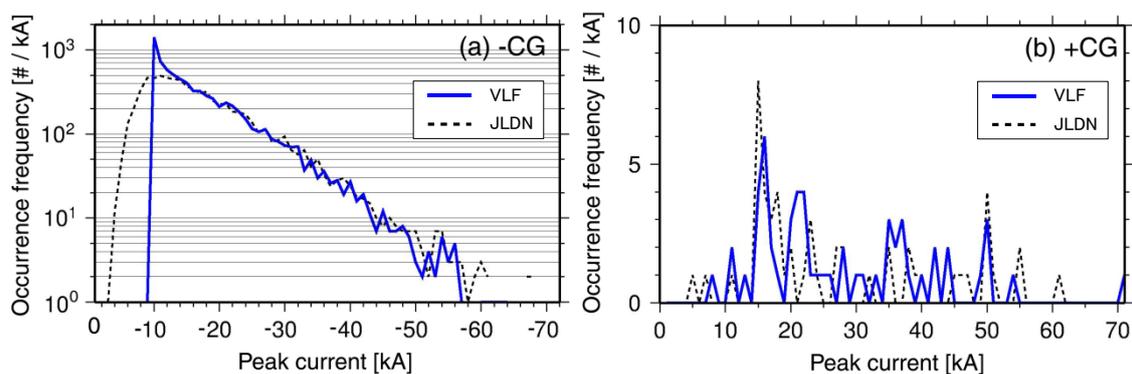
Figure 3.22. Occurrence frequency of peak current estimated by VLF and JLDN. (a) negative CG, (b) positive CG.

Figure 3.23 shows the frequency distribution of estimated iCMC. The left panel (a) shows the case of –CG, and the right panel (b) shows the case of +CG. In the case of – CG, the frequency distribution of iCMC has a peak at –4 C·km. The distribution of occurrence frequency decreases exponentially with increase in iCMC intensity on single logarithmic plot for the iCMC between 4 C·km and 30 C·km. In the case of the occurrence frequency of iCMC intensity less than 4 C·km, its frequency distribution decrease sharply with decrease in iCMC intensity. The characteristics of occurrence frequency of iCMC cannot be investigated for the iCMC more than 30 C·km because the number of events are small. Similarly, in the case of +CG, the characteristics of occurrence frequency of iCMC cannot be investigated because the number of events are small.
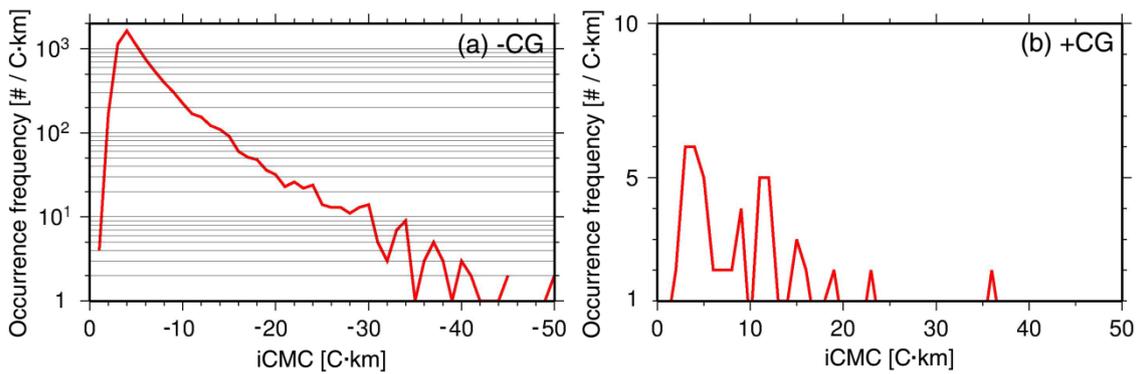
Figure 3.23. Occurrence frequency of iCMC. (a) negative CG, (b) positive CG.
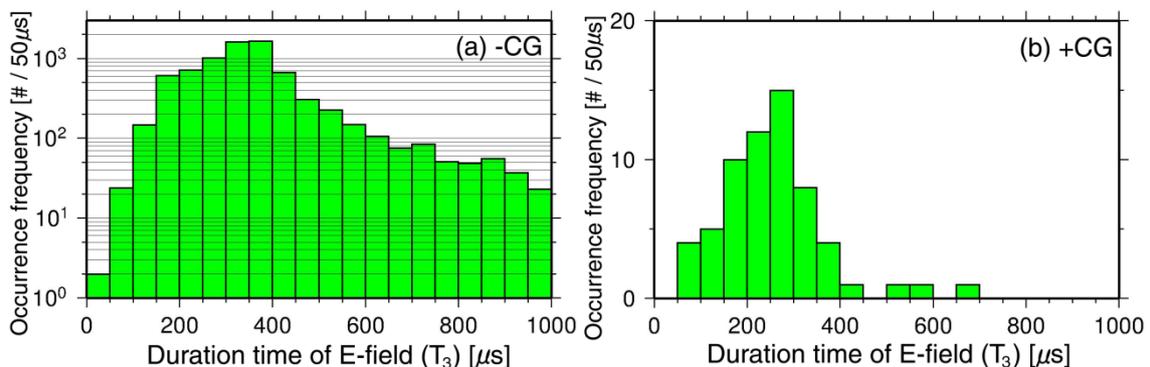
Figure 3.24. Occurrence frequency of duration time of electric field (T_3). (a) negative CG, (b) positive CG.

Figure 3.24 shows the distribution of occurrence frequency of duration time of electric field (T_3), The left panel (a) shows the case of –CG, and right panel (b) shows the case of +CG. In the case of –CG, the frequency distribution of T_3 has a peak around 350–400 µs. The frequency distribution of T_3 more than 400 µs indicates that its frequency distribution decrease exponentially with increase in time on single logarithmic plot. In the case of +CG, the frequency distribution of T_3 has a peak around 250–300 µs.

The relationship among iCMC, the peak current intensity estimated from VLF data and the duration time of sferic (T_3) was examined. Figure 3.25 shows a scatter plot of the iCMC versus the peak current, (a) negative CG, (b) positive CG, respectively. The solid lines in black are power function fitted by the least-squares method as

$$-CG: y = -0.187x^{1.242} \tag{3.16}$$

$$+CG: y = -0.101x^{1.390} \tag{3.17}$$

where *x* and *y* show the peak current and iCMC, respectively. There is a good correlation between iCMC and the peak current (–CG: $R^2 = 0.74$, +CG: $R^2 = 0.61$). It is found that iCMC intensity more than 20 C·km in the case of –CG is a weak correlated with the peak current (–CG: R2 = 0.21).

Figure 3.26 shows a scatter plot of the duration time of sferic (T_3) (µs) versus iCMC [C·km]. The solid lines in black are linear function fitted by the least-squares method as

$$-CG: y = -0.017x - 0.5 \tag{3.18}$$

$$+CG: y = 0.047x - 2.1 \tag{3.19}$$

where *x* and *y* show the duration time of sferic (T_3) and iCMC, respectively. There is a weak correlation between iCMC and the duration time of sferic (T_3) (–CG: $R^2 = 0.21$, +CG: $R^2 = 0.34$).

Figure 3.27 shows a scatter plot of the duration time of sferic (T_3) (µs) versus iCMC (C·km). The solid lines in black are linear function fitted by the least-squares method as

$$-CG: y = -0.011x - 13.2 \tag{3.20}$$

$$+CG: y = 0.015x + 23.2 \tag{3.21}$$

where x and y are duration time of sferic (T_3) and the peak current. There is no correlation between the peak current and the duration time of sferic (T_3) (–CG: $R^2 = 0.04$, +CG: $R^2 = 0.02$).
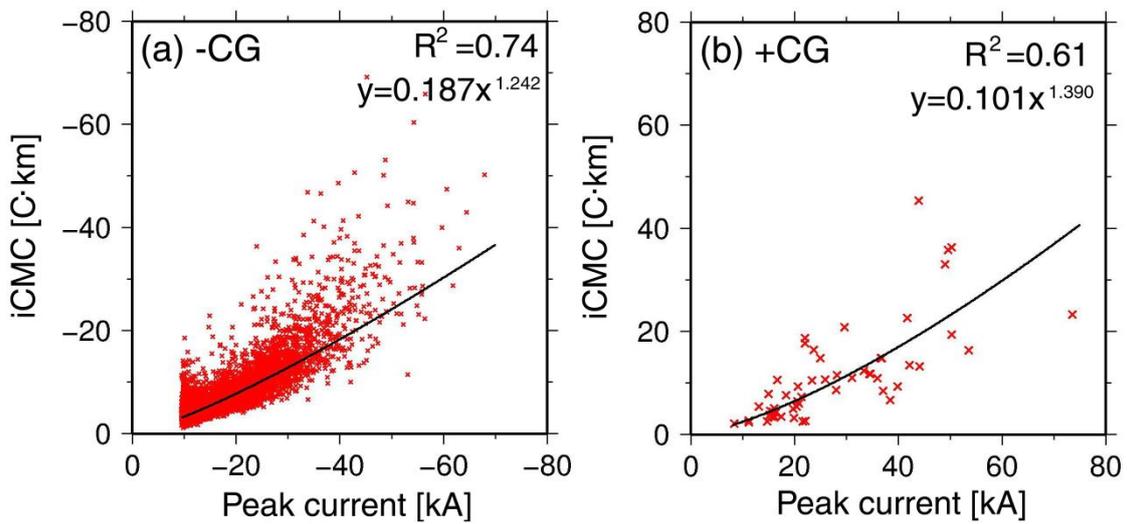
Figure 3.25. Scatter plot of iCMC [C·km] versus estimated peak current [kA]. (a) negative CG, (b) positive CG.
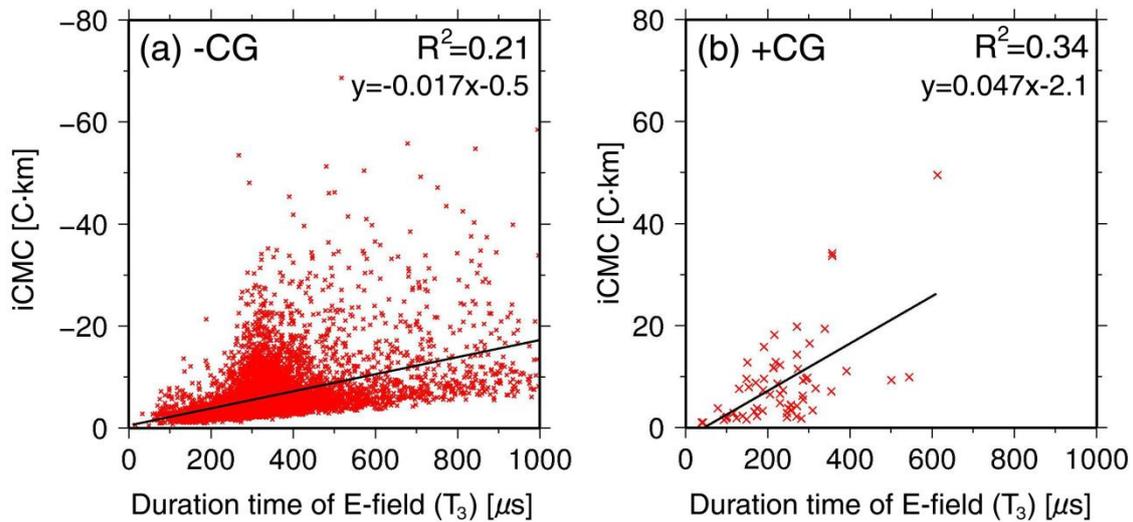
Figure 3.26. Scatter plot of the duration time of sferic (T_3) [µs] versus iCMC [C·km]. (a) negative CG, (b) positive CG.
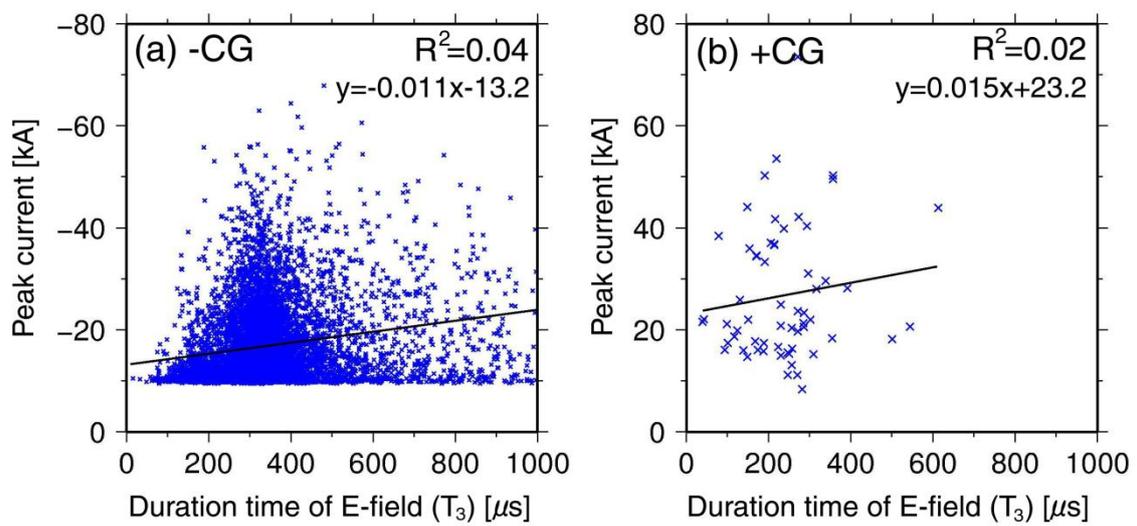
Figure 3.27. Scatter plot of the duration time of sferic (T3) [µs] versus estimated peak current [kA]. (a) negative CG, (b) positive CG.

3.4 Discussion

3.4.1 Estimation of peak current

The peak current intensities was estimated using the normalized amplitude of VLF waveform and the peak current of JLDN data. The normalized amplitude of VLF waveform at 50 km is highly correlated with the peak current of JLDN data. The determination coefficient of –CG and +CG between them are 0.79 and 0.81, respectively. The relationship between the normalized amplitude of VLF waveform and the peak current of JLDN data is well fitted to linear function as shown in equation (3.10) and equation (3.11). According to equation (3.10), the peak currents from −9.2 kA to 0 kA cannot be estimated.

Equation (3.10) and equation (3.11) have the nonzero intercept. This nonzero intercept is pointed out by *Orville et al.* [1991a] and *Idone et al.* [1993] on the NLDN. According to *Idone et al.* [1993], the relationship between 57 directly measured stroke peak currents originated in 36 triggered lightning flashes and NLDN normalized magnetic signal strengths (M_{peak}) has the following form,

$$I_{peak} = 4.20 + 0.171 M_{peak} \qquad (3.22)$$

where I_{peak} is the peak current (kA). *Cummins et al.* [1998] suggested that the nonzero intercept in the relation may reflect the fact that NLDN did not detect many strokes with peak current below 5 kA. The result of comparison between the peak current estimated by WWLLN which measure the VLF radiowaves and that of NZLDN (New Zealand Lightning Detection Network) has also the nonzero intercept [*Hutchins et al.*, 2012]. Figure 3.28 shows the relationship between peak current of WWLLN and the NZLDN peak current of NZLDN. If a intercept goes through zero intercept other than equation (3.10) and (3.11), the determination coefficient of correlation between the normalized amplitude and peak current of JLDN is clearly lowered. Therefore, equation (3.10) and (3.11) are used to estimate the peak current. The peak currents estimated from VLF data have a variation of 20 % with respect to peak current of JLDN data around 20 kA.
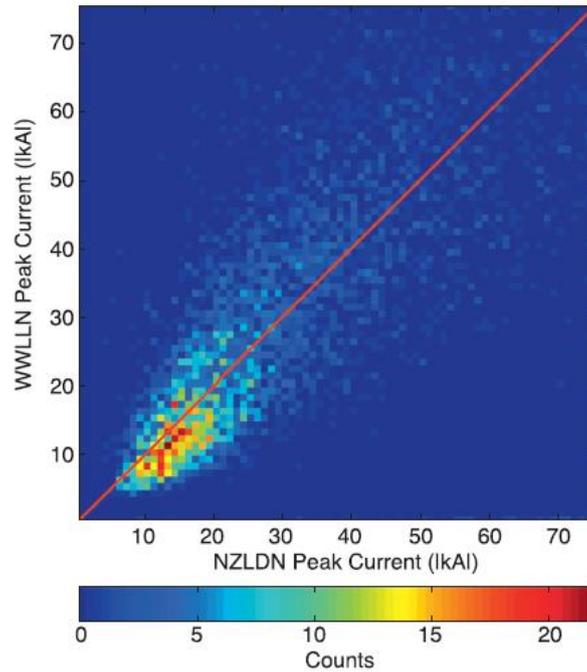
Figure 3.28. WWLLN peak current vs NZLDN return-stroke peak current for three time periods in 2009 using 5260 matches [*Hutchins et al.*, 2012].

As Figure 3.22 (a) shows, the distribution of occurrence frequency of the peak current intensity estimated from VLF data mostly coincides with that of JLDN. The result indicates the validity of the relational expression with straight-line approximation in the range of 50–200 km. According to *Lu et al.* [2011], the examination of VLF magnetic field data for over 2,000 CG lightning strokes in the range of 200 to 4,000 km indicates that the VLF intensity is correlated with the peak current of NLDN data. They found that the lightning peak current and the amplitude of VLF signal satisfy the following relationship,

$$\text{Daytime: } B_p = 127.06 * \frac{I_{peak}}{r^{1.23}} \tag{3.23}$$

$$\text{Nighttime: } B_p = 40.6 * \frac{I_{peak}}{r^{1.02}} \tag{3.24}$$

where B_p (nT) is the amplitude of VLF signal recorded at distance r (km) from the lightning discharge with a peak current of I_{peak} (kA). The relationship between the peak VLF signal and the distance from lightning discharge is described as power function

while that of the relationship in this study is described as linear function. In addition, proportionality coefficient and exponent value of equation (3.23) and (3.24) are differed between day and night. This is attributed to the fact that the results of *Lu et al.* [2011] is affected by the skywave because the skywave overlaps groundwave at more than 1,000 km. Therefore, the result obtained by the analysis for the groundwave in the range of 50–200 km is different in their results.

    The occurrence frequency of the peak current intensity between 10 kA and 12 kA estimated from VLF data is clearly more than that of JLDN as shown in Figure 3.22 (a). The peak current intensity less than 10 kA estimated by JLDN are estimated as about 10 kA. It is difficult to estimate the peak current less than 10 kA, because the events of small peak current intensity have a faster time variation (an order of μs) of the lightning current which cannot be detected by the VLF lightning observation system which has low sensitivity for high frequency more than 50 kHz.

3.4.2   Estimation of impulsive charge moment change

The iCMC, peak current and duration time of sferic were estimated from VLF data for 4 days. The detection efficiency of iCMC of −CG is about 70–80 %, but that of +CG is about 20–40 % with respect to JLDN data. The Low detection efficiency of +CG is caused by the discrepancy of polarity. In some part of +CG, iCMC cannot be calculated because the source current varies intricately.

    Figure 3.29 shows the frequency distribution of iCMC of this study and that of the CMCN (charge moment change network) by *Cummer et al.* [2013]. Note that iCMC of the CMCN is the lightning charge moment change estimated from the ELF (less than 1 kHz) data during the first 2 ms after the discharge onset. The red solid line is distribution of iCMC of this study, and the blue dashed line is distribution of iCMC of CMCN adapted from *Cummer et al.* [2013]. The occurrence frequency of this study is sifted so that the value of both studies are same at 4 C·km. It is shown that the curve in this study (red line shown in Figure 3.29) has a peak at −4 C·km. The distribution of iCMC of CMCN does not have a clear peak unlike its distribution of this study. This is

attributed to the fact that CMCN has lower sensitivity for the return than for the continuing current because iCMC estimation by *Cummer et al.* [2013] uses ELF frequency range lower than 1 kHz by which rapid change of return stroke cannot be measured sufficiently.
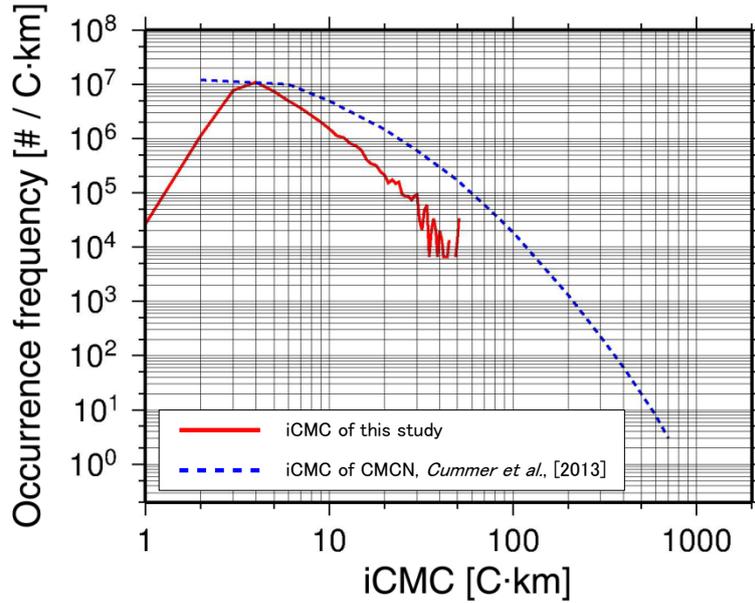
Figure 3.29. Distribution of iCMC for –CG lightning events. Red solid line is distribution of iCMC of this study, and blue dashed line is distribution of iCMC adapted from *Cummer et al.*, [2013].

According to *Dennis and Pierce* [1964] and *Jones* [1970], the lightning current flowing at the ground during the primary return stroke is described as following equation.

$$I(t) = I_0\{\exp(-\alpha t) - \exp(-\beta t)\} \tag{3.25}$$

where *I(t)* is the current at the ground of the return stroke at time *t*, I_0, *α* and *β* are constants. The value of 30 kA, 2×10^4 sec^{-1}, and 2×10^5 sec^{-1} are suggested as typical values of I_0, *α* and *β*, respectively. [*Dennis and Pierce*, 1964]. The current moment is described by

$$IM(t) = I(t) \cdot dl(t) \tag{3.26}$$

where *IM*(*t*) is the current moment at time t, and *dl*(*t*) is the discharge length at time *t*. Assuming that the return stroke speed is half of speed of light, and upper end of discharge is 5 km, the current moment is computed. Then CMC is obtained by integrating current moment with time. Figure 3.30 shows the time variation of typical lightning current and the current moment. The red line is the current moment, the blue line is lightning current, and the black line is the discharge length. In this case, the charge amount and the value of CMC are computed as 1.3 C and 5.4 C·km, respectively. This result is consistent with the value of iCMC of this study estimated from the portion of the return stroke.
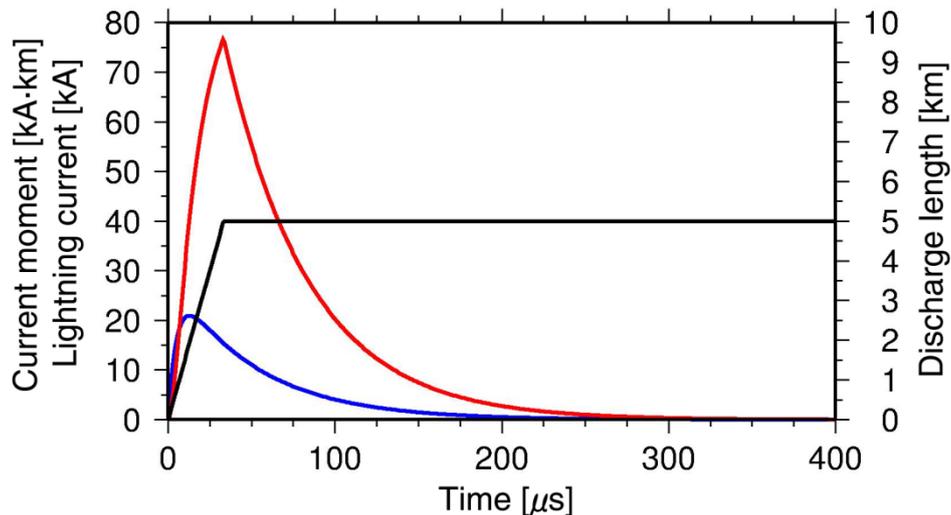
Figure 3.30. Typical current of return stroke and current moment. Red line is the current moment, blue line is the lightning current, and black line is the discharge length.

Figure 3.31 shows the relationship between the peak current estimated from VLF data and iCMC of –CG. The red cross shows iCMC more than –20 C·km, and the blue cross shows iCMC less than –20 C·km. The dashed line (3) in black is power function fitted by the least-squares for whole of iCMC. iCMC is estimated as about –15 C·km at peak current equal 30 kA by the relation (3) in Figure 3.31. Figure 3.32 shows the relationship between charge for the events with a duration of 1 ms and the peak current in rocket-triggered lightning in Florida [*Schoene et al.*, 2010]. When the peak current equal 30 kA in Figure 3.32, the value of charge is about 4 C. Assuming the discharge

length equal 5 km, the value of CMC is about 20 C·km. The charge of rocket-triggered lightning in Florida agrees with the result of this study, which is consistent with the value of iCMC estimated from VLF data.
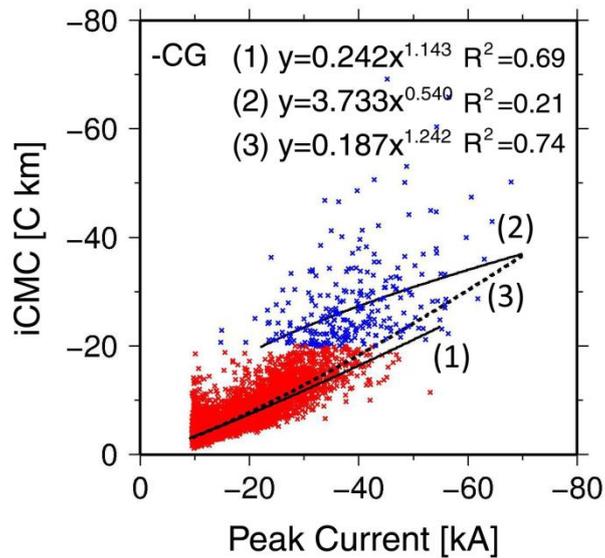
Figure 3.31. Peak current estimated from VLF data versus iCMC of –CG. The red cross shows iCMC more than −20 C·km, the blue cross shows iCMC less than −20 C·km.
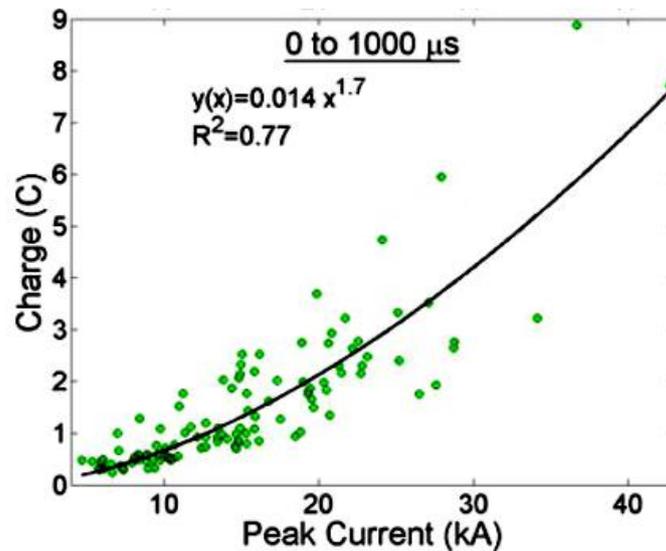
Figure 3.32. Charge with a duration of 1 ms versus peak current in rocket-triggered lightning in Florida [*Schoene et al.*, 2010].

The iCMC has large correlation with peak current below absolute value of 20 C·km (R^2 = 0.69). On the other hand, iCMC above 20 C·km of its absolute is weakly correlated with the peak current (R^2 = 0.21). The solid black line (1) and (2) in Figure 3.31 are linear function fitted by the least-squares for the events less than absolute value of 20 C·km and that of more than 20 C·km, respectively. The coefficient and exponent of the two equation are clearly different from each other.

Figure 3.33 shows scatter plot of iCMC which is estimated from ELF data with a duration of 2 ms versus peak current of NLDN [*Cummer et al.*, 2013]. In the case of − CG (left side of Figure 3.33), the red and orange area which indicate highly occurrence rate of events extend below around 20–30 C·km. This result agrees with the result of this study. Figure 3.34 shows scatter plot of the charge moments estimated from ELF data versus the peak currents for 331 events of sprite-including CG discharge [*Sato*, 2004]. Sprite which generated by huge lightning discharge is optical emission of the transient luminous events above thunderstorm. The range of the CMC is from 100 to 10,000 C·km. In the case of these huge CG event, there is no correlation between the charge moment change and the peak current. In summary, it is concluded the correlation between small CMC (less than tens of C·km) and the peak current is high, however the correlation between huge CMC (more than 100 C·km) and the peak current is extremely low. It is presumed that the relationship between them has a boundary around 20 C·km.
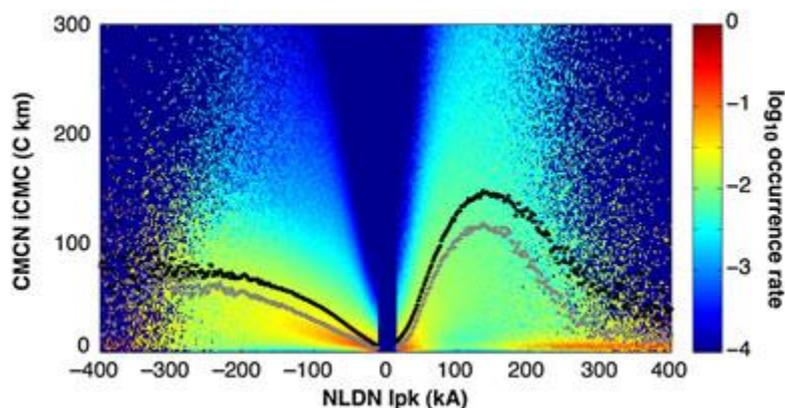
Figure 3.33. Normalized scatter density plot of iCMC versus NLDN peak current (Ipk) for 13.1 million NLDN-identified CG strokes. Each vertical slice denotes the probability distribution function of iCMC (on a logarithmic color scale) for the given value of Ipk, and the mean and median iCMC for each value of Ipk are marked with black and gray dots, respectively [*Cummer et al.*, 2013].
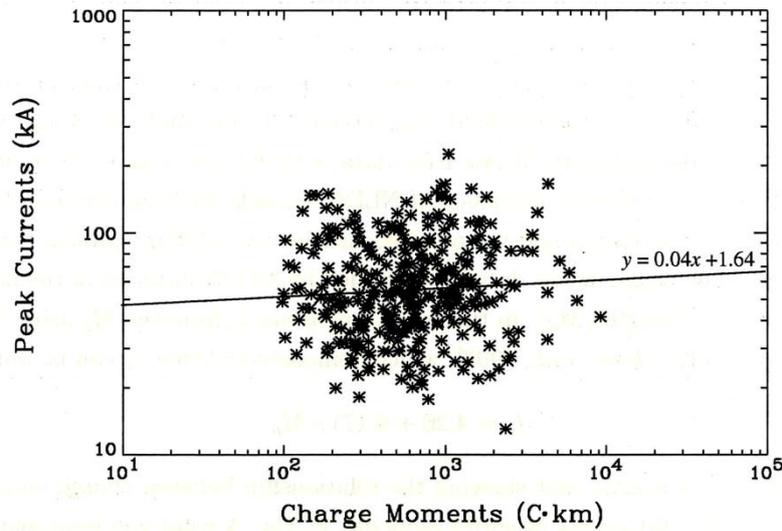
Figure 3.34. Scatter plot of the charge moments versus the peak currents for 331 events of sprite-including CG discharge [*Sato*, 2004].

Finally, the relationship among iCMC, the peak current estimated from VLF data and the duration time of electric field (T_3) were discussed. In the case of –CG, the frequency distribution of T_3 has a peak around 350–400 μs as shown in Figure 3.24 (a). There is   no correlation between the peak current estimated from VLF data and T_3 as shown in Figure 3.27 (a). T_3 and the peak current are independent phenomena from each other. T_3 is the time of integration interval to estimate iCMC, then iCMC cannot be determined by just peak current.

3.5   Summary and conclusion

The method of analysis to estimate the impulsive charge moment change (iCMC) with a duration of 1 ms or less from the VLF sferics is established. By this method, the lightning magnitudes of small CG lightning occurred in the range of 50–200 km can be estimated. In order to establish the method to estimate the peak current from VLF waveform, the relationship between peak current of Japan Lightning Detection Network (JLDN) and normalized amplitude of the electric field waveform was investigated. High

correlation between the peak current of JLDN and the normalized amplitude in the range of 50–200 km is shown. The methodology to estimate the peak current using waveform in the VLF band, which is detectable at far distance than that in the LF band, was established. The method contributes to suppression of the calculation amount for estimating iCMC, which may make it possible to calculate lightning magnitudes in a short period for real-time alert.

The 10,606 VLF sferic events obtained at Yamanashi site at the distance from 50 to 200 km were analyzed. iCMC of –CG and +CG were calculated successfully for 7,418 and 57 events, respectively. The detection efficiency of iCMC estimation of –CG is about 72 %. Since the estimated detection efficiency for the current systems for iCMC or peak current using the VLF data are less than 11 %, that of the VLF lightning observation system developed in this study for estimation of iCMC is the highest level in the world.

In the case of –CG, the frequency distribution of peak current intensity more than 12 kA estimated from the VLF data closely coincides with that of the JLDN. This result statistically indicates the validity on the relation expression developed in this study. It is found that the frequency distribution of iCMC has a peak at −4 C·km.

The relationship between iCMC and peak current was examined. It is found that correlation between iCMC over 20 C·km and peak current is small ($R^2 = 0.21$) while correlation between iCMC less than 20 C·km and peak current is high ($R^2 = 0.69$). The relationship among iCMC, peak current and duration time of electric field waveform was also examined. There is a weak correlation between iCMC and the duration time of the electric field waveform (–CG: $R^2 = 0.21$, +CG: $R^2 = 0.34$). There is no correlation between the peak and the duration time of electric field waveform (–CG: $R^2 = 0.04$, +CG: $R^2 = 0.02$). These results suggest that iCMC cannot be estimated from the peak current for the event over 20 C·km. It is necessary to estimate iCMC more than 20 C·km from the time variation of waveform.

Chapter 4

Relationship between atmospheric parameters and lightning magnitudes

4.1 Introduction

Most of previous studies have been considered only the information of the occurrence frequency and polarity of lightning in the study of the relationship between the lightning activity and the atmospheric parameters. *Holle et al.* [1994] found that convective echo of radar tends to have almost exclusively negative CG lightning, whereas up to one-third of CG lightning in stratiform regions are positive. *Carey and Rutledge* [1998] found that the correlation between negative CG lightning and the area averaged rain rate is very high (r = 0.93) and the anti-correlation between large hail echo volume and positive CG lightning is much more significant (r = −0.85).

Some studies investigated the relationship between storm evolution and the peak current of lightning [*Carey and Rutledge*, 2003; *Soula et al.*, 2004; *Montanya et al.*, 2007]. *Carey and Rutledge* [2003] found that median peak current in severe storms is very low and is noticeably smaller than in non-severe storms. *Soula et al.* [2004] reported that some of hailstorm produced especially high positive CG proportions associates with negative CGs with low values of peak current and multiplicity. *Montanya et al.* [2007] reported that the average peak currents and multiplicities observed during the whole lifetime of 2 hailstorms are lower than those of typical

values. They suggested that less negative charge is available to be lowered to the ground, probably because of strong updrafts. The suggestion is open to question because the peak current intensity depends on the electric conductivity of the surface and line charge density in the lower portion of the stepped leader.

Thomas et al. [2010] reported that there is no clear relationship between impulse charge moment change (iMq) of inner core and storm intensity of 3 hurricanes. In their study, iMq is defined as the product of cloud charge removed by vertical currents within 2 ms of return stroke and the mean height of this removed charge [*Cummer and Inan*, 2000; *Thomas et al*., 2010]. However the relationship between development of individual thunderstorm and lightning magnitudes is not examined. Since the detection efficiency of iCMC of their study for small lightning is low, the relationship between storm evolution and the small lightning activity which accounts for the majority of CG lightning cannot be examined. iCMC might be quantitatively related to the meteorological parameters.

Therefore, the relationship between the developing process of thunderstorm and the lightning magnitudes was investigated using the estimated iCMC and peak current.

4.2   Data and Methodology

The analysis deals with a separable heat thunderstorm without any synoptic-scale disturbance, such as a front and a low pressure near the Kanto area. The three separable thunderstorms were selected. Case (1) is the thunderstorm occurred in the period from 13:40 to 15:50 on July 11, 2013. Case (2) is the thunderstorm occurred in the period from 17:10 to 19:10 on July 11, 2013. Case (3) is the thunderstorm occurred in the period from 16:40 to 19:30 on August 11, 2013.

The C-band rain radar data provide by the Japan Meteorological Agency (JMA) was used to compare the atmospheric parameter with the lightning activity. The JMA rain radar data is obtained by 20 radar stations placed throughout Japan. The radar reflectivity at 2 km altitude obtained at each station is corrected and converted to 10-minute-interval surface rainfall intensity. The resolution of the radar rain data is

1-km resolution, and that of the radar echo top data is 2.5-km resolution. The rain volume and the area size of echo height more than 12 km are calculated for the area of analysis on each 10 minute. The spatial area size of analysis is determined so as to cover the whole thunderstorm. The area size is fixed through a life cycle of thunderstorm while the center location of the analyzed area is changed with the movement of thunderstorm.

The estimated iCMC, the peak current of JLDN data and the duration time of electric field (T_3) during a 10-min period centered at the radar time are distributed. The relationship between the time variation of the rain volume, the area size of radar echo height more than 12 km and the lightning parameters for the 3 thunderstorms was examined using the estimated iCMC, the peak current and the duration time of the electric field (T_3).

4.3   Results

4.3.1   Case of July 11, 2013 (Case 1)

The thunderstorm occurred in the period om 13:40 to 15:50 on July 11, 2013. The weather conditions in this case was verified. Figure 4.1 shows the surface weather chart at 09 h (JST), July 11, 2013. The high-pressure system (described as H in Figure 4.1) in the Pacific Ocean covers Kanto region. The Baiu (rainy season) front is located across Tohoku region. The typhoon located over the south of Japanese islands is moving to the northwest. However the weather condition around Kanto region is not affected by the typhoon because it's well distant from Kanto region. Figure 4.2 and Figure 4.3 show the 500-hPa level upper weather chart at 09 h (JST) and at 21 h (JST), July 11, 2013, respectively. The black line is the isohypse (a line connecting points on an isobaric surface which have a constant height), the color contour is the air temperature at 500 hPa at isobaric surface. The upper level chart shows no significant change in the contour and the temperature in Kanto region. The partial area of temperature from −12 ˚C to −6 ˚C in the south of Kanto region at 21 h (JST) is corresponding to the convective activity

in the thunderstorm. According to JMA reports, high temperatures of 39.5 ˚C in Tatebayashi, Gunma (Figure 4.4 (b)), north of the Kanto was recorded. The thunderstorms occurred over a wide range of northern Kanto from the afternoon.

The period of analysis ranged from 13:40 to 15:50 (JST). The area of analysis was confined from 139.4°E to 140.4°E and from 36.3°N to 36.8°N. Figure 4.4 (a) shows the area of analysis on July 11, 2013 from 13:40 to 15:50. The considered thunderstorm moved from west to east in Tochigi prefecture.
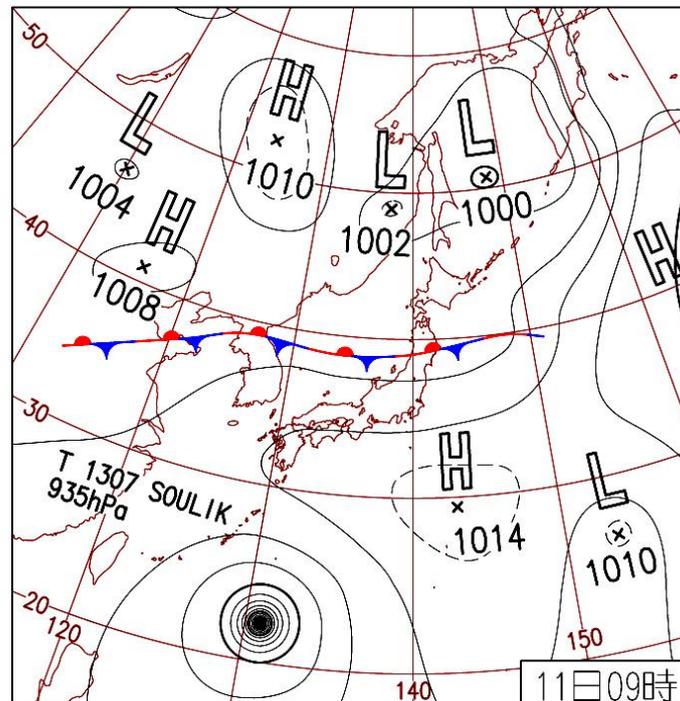
Figure 4.1. Surface weather chart at 09 h (JST), July 11, 2013.
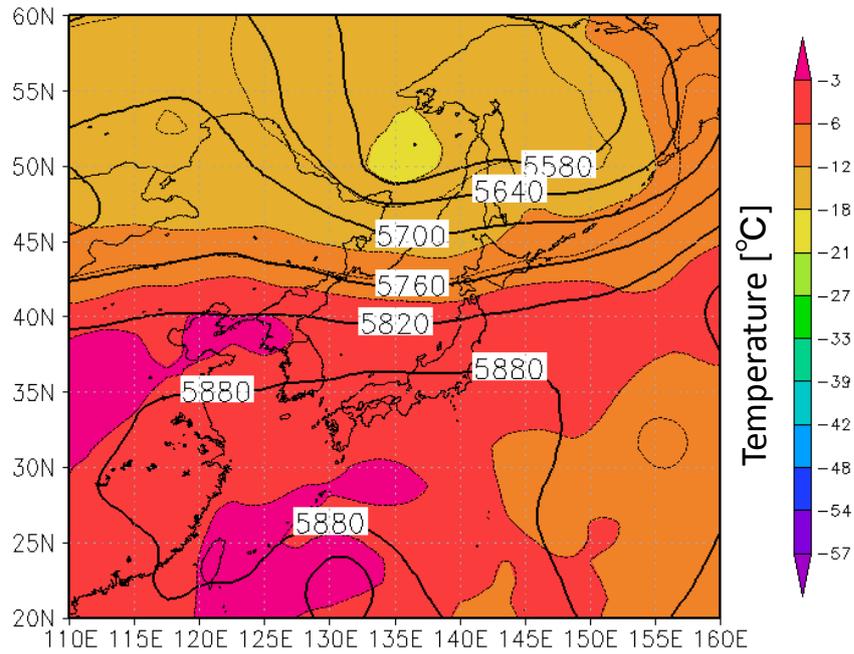
Figure 4.2.   500-hPa level upper weather chart at 09 h (JST), July 11, 2013. The black line is isohypse, and color contour is an air temperature at 500 hPa at isobaric surface.
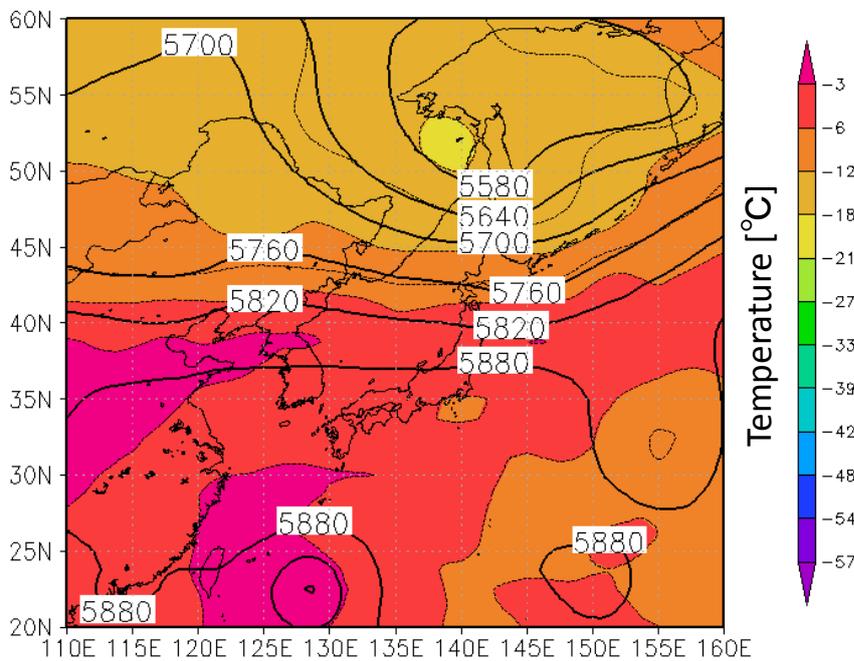
Figure 4.3.   500-hPa level upper weather chart at 21 h (JST), July 11, 2013. The black line is isohypse, color contour is an air temperature at 500 hPa at isobaric surface.
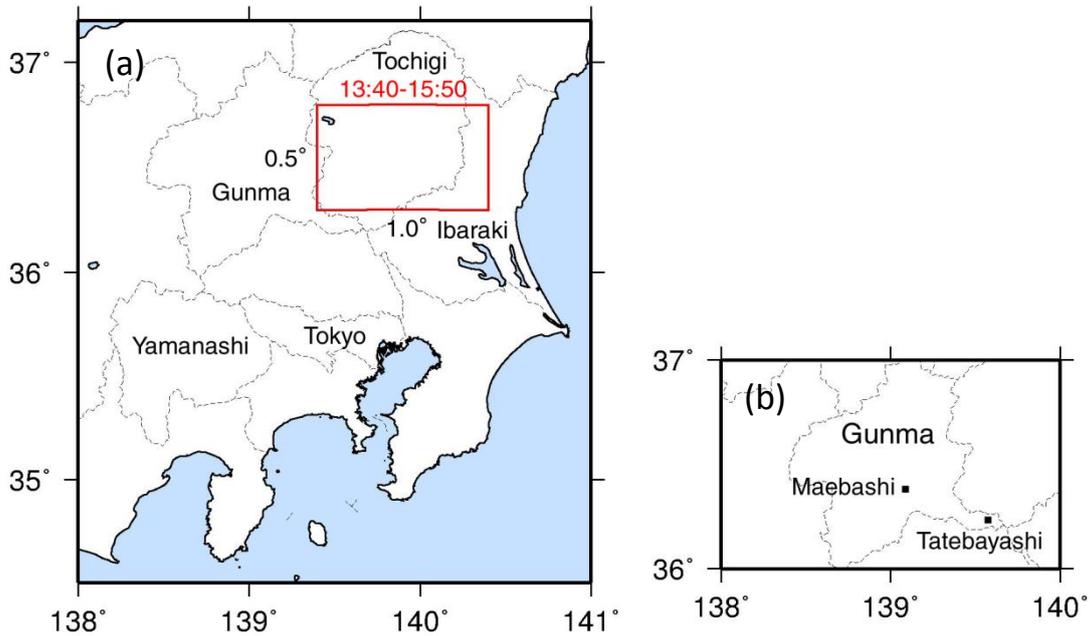
Figure 4.4. (a) Area of analysis on July 11, 2013 from 13:40 to 15:50 (JST). (b) Map of Gunma prefecture.

Figure 4.5 shows the evolution of the rain area on July 11, 2013 from 13:50 to 15:20. The rain intensity is color shaded as shown, the altitude is grey shaded, and dashed line is a border between prefectures. The CG lightning flash locations during a 10-min period centered at the radar time are plotted. The black cross indicates −CG. The –CG lightning dominates through whole lifetime of the thunderstorm. The lightning activity starts at 14:00 and reaches its peak at 14:30. It seems that the distribution of the lightning locations varied as time passes. The lightning locations are distributed from center of thunderstorm to east side at 14:20, and moved to the area from south side of thunderstorm to southwest side at 14:30. The intensive rain area more than 80 mm/h (described as red in Figure 4.5) spreads at 14:10, then weak rain area less than 10 mm/h (aqua in Figure 4.5) spreads toward northeast after 14:40. The lightning activity rapidly weakens after 14:50.
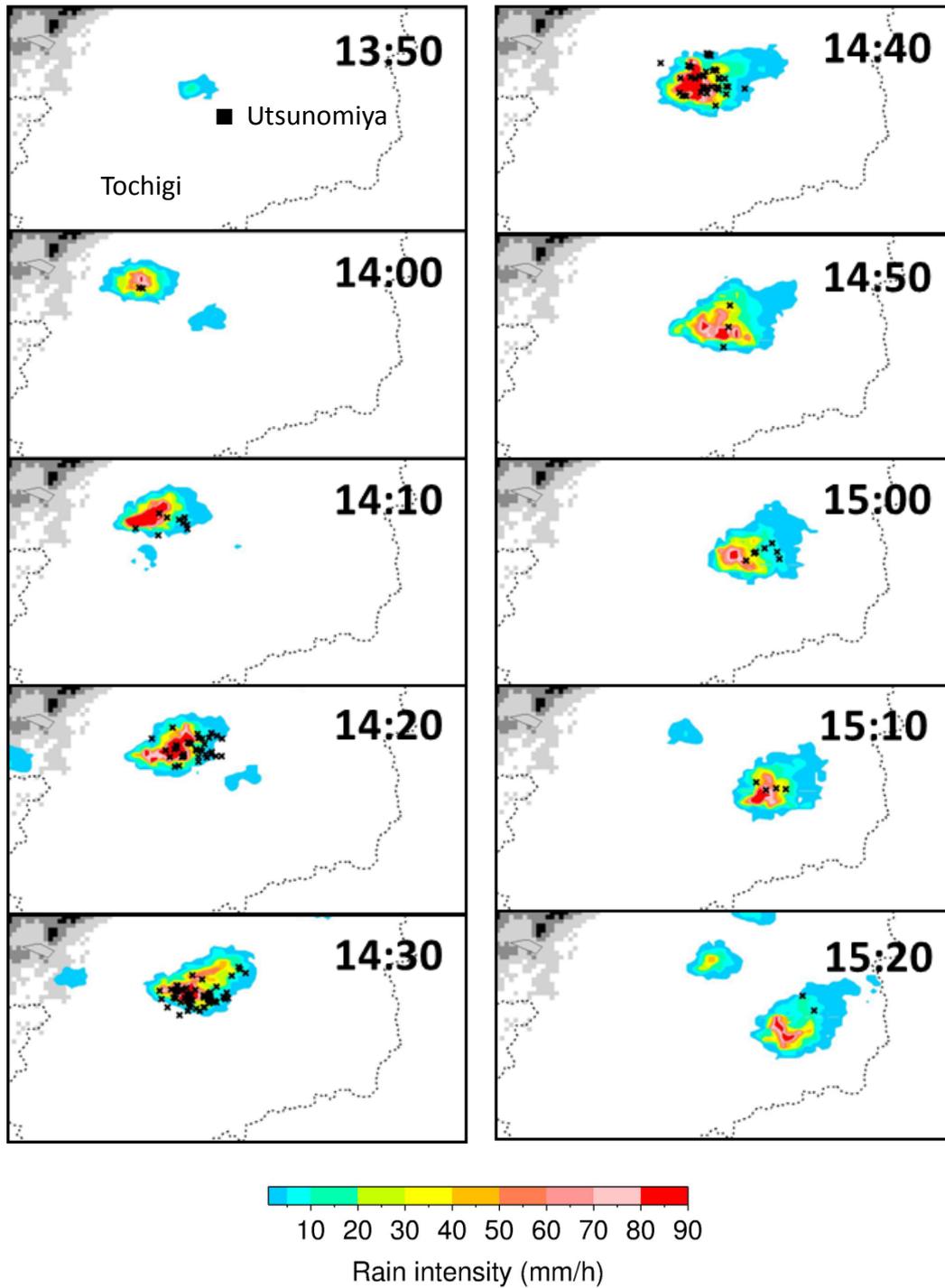
Figure 4.5. Evolution of the precipitation area on July 11, 2013 from 17:10 to 19:10 (JST). The CG lightning flash location during a 10 min period centered on the radar time are plotted. The black cross indicates a negative CG.

Figure 4.6 shows the time series of the –CG and +CG flash rate, IC flash rate, rain volume and area size of echo height more than 12 km on July 11, 2013 from 13:50 to 15:50. The bar graph in Figure 4.6 displays the rain volume calculated over 10-min interval. The blue line, red line, and dashed line display the 5-min flash rate of –CG, +CG and IC, respectively. The green line is the area size of echo height more than 12 km, calculated over 10-min interval. This thunderstorm produces 198 flashes of –CG and 31 flashes of IC throughout its whole lifetime, and that does not produce +CG flashes. The averaged values of peak current are –13.1 kA for –CG and 21.3 kA for +CG, respectively. The flash rate of –CG increases from 14:00 to 14:30. The peak of flash rate is 48 events per 5 minutes at 14:30. After that, –CG flash rate rapidly decreases. The rain volume increases from 14:00 to 14:40. The peak of rain volume is approximately 1.3×10^9 mm^3 per 10 minutes at 14:40. The area of radar echo height more than 12 km increases from 14:20 to 14:40. The peak of the area is 22 km^2 at 14:40. The time evolution of rain volume, area of radar echo height more than 12 km and –CG flash rate show similar variation from 14:00 to 15:00. The peak of –CG flash rate is shifted in advance by about 10 minutes as compared to the peak of the rain volume and the area of radar echo height more than 12 km.

Figure 4.7 shows the time series of the –CG and +CG flash rate, IC flash rate, area size of intensive rain more than 50 mm/h and area of echo height more than 12 km during the same period. The bar graph in Figure 4.7 displays the area size of intensive rain more than 50 mm/h, and the lines in Figure 4.7 are same as in Figure 4.6. The peak of area size more than 50 mm/h is 48 km^2 at 14:40. The rain area size more than 50 mm/h shows similar variation to the rain volume from 14:00 to 15:00. However, the time evolution of the rain area size more than 50 mm/h and rain volume shows different variation after 15:10 when –CG lightning activity weakens.
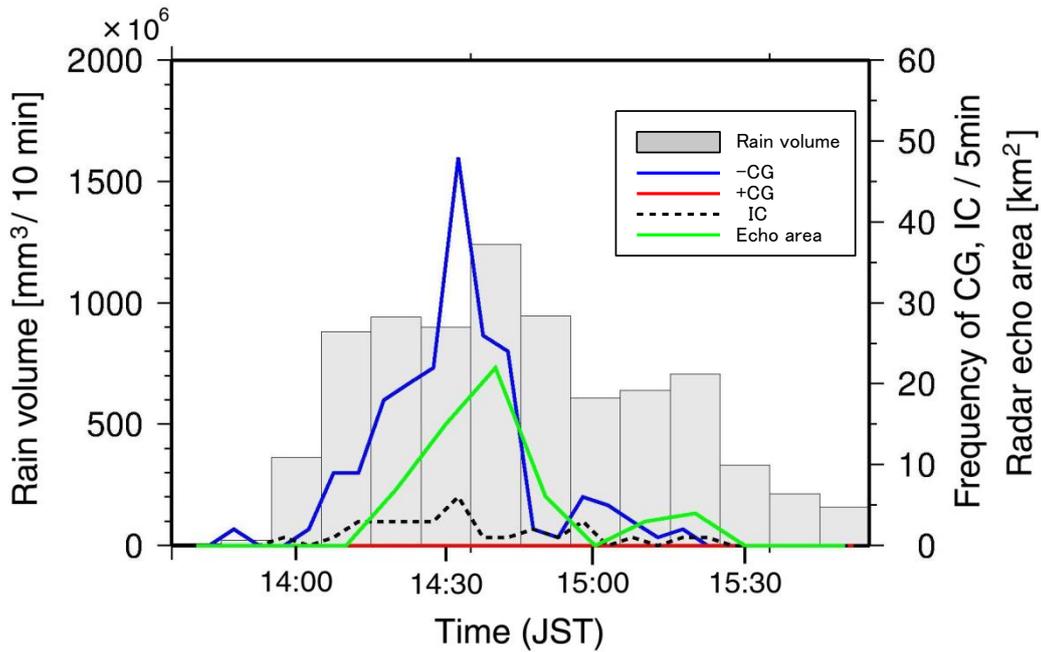
Figure 4.6. Evolution of the rain volume, area of echo height more than 12 km and lightning flash rate on July 11, 2013 from 13:50 to 15:50 (JST).
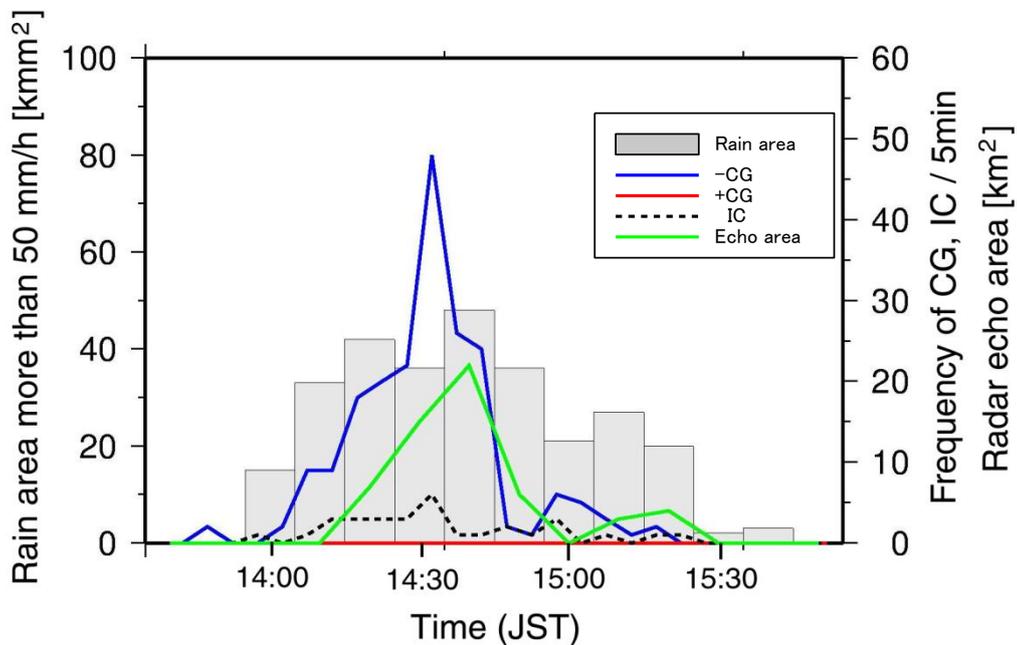
Figure 4.7. Evolution of the rain area more than 50 mm/h, area of echo height more than 12 km and lightning flash rate on July 11, 2013 from 13:50 to 15:50 (JST).

Figure 4.8 shows the time variation of frequency distribution of (a) iCMC, (b) peak current estimated by the JLDN and (c) duration time of electric field (T_3) on July 11, 2013 from 14:00 to 15:10. All of the events shown in Figure 4.8 is –CG. These events are distributed over 10-min interval. The detection efficiency of iCMC in this period as compared to the events detected by the JLDN is 53 %. The averaged value of iCMC is – 5.6 C·km.

The distribution of iCMC varies as time advances. The events with iCMC more than 5 C·km in absolute value increases and are distributed widely for iCMC from 14:10 to 14:40. The distribution of peak current and duration time of electric field also varies as time advances. The events with peak current intensity more than 15 kA in absolute value also increases and are distributed widely for peak current from 14:10 to 14:40. The events of duration time of electric field (T_3) more than 200 μs indicate the similar variation to that of iCMC and peak current. As shown in Figure 4.5 and Figure 4.6, this thunderstorm developed in this period, then it reached mature stage at around 14:40. After 14:50 when –CG flash rate rapidly decreases, the distribution of iCMC, peak current and duration time of electric field (T_3) show no significant time variation.
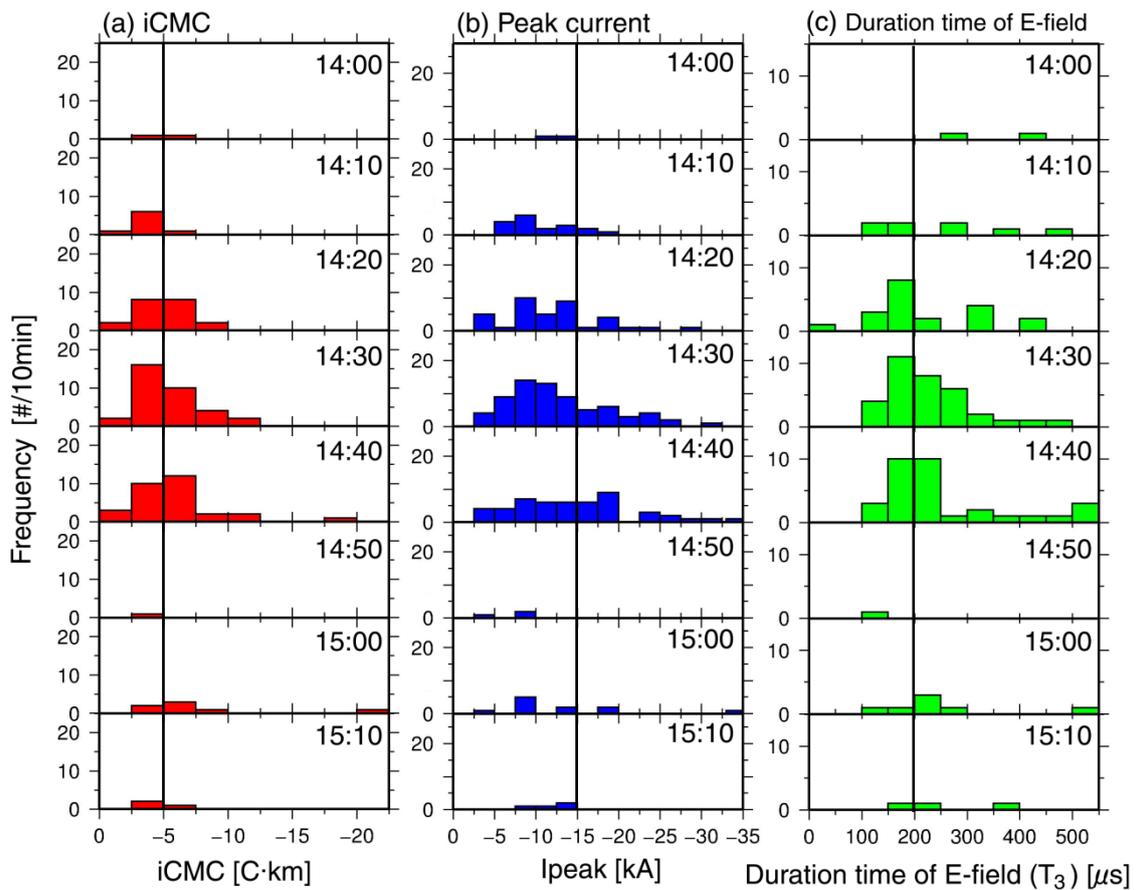
Figure 4.8. Time variation of frequency distribution of (a) iCMC, (b) peak current and (c) duration time of electric field (T_3) on July 11, 2013 from 14:00 to 15:10 (JST).

4.3.2   Case of July 11, 2013 (Case 2)

The thunderstorm occurred in the period from 17:10 to 19:10 on July 11, 2013. According to the JMA report, a downburst occurred at around 18:00 (JST) in Isesaki and Ota, Gunma (Figure 4.9 (b)). The intensity of downburst occurred in Isesaki was estimated as F0 (17–32m/s) of Fujita scale, and that occurred in Ota was estimated as F1 (33–49m/s). The period of analysis ranged from 17:10 to 19:10. The area of analysis was confined within a dimension of 0.25° in the longitudinal direction by 0.3° in the latitudinal direction. The considered thunderstorm moved from west to east in the north of Kanto. Figure 4.9 (a) shows the area of analysis in this case.

Figure 4.10 shows the evolution of the rain area in the period from 17:10 to 19:10 on July 11, 2013. The rain intensity is color shaded as shown, and dashed line is a border between prefectures. The CG lightning flash locations during a 10-min period centered on the radar time are plotted. The black cross indicates −CG. The blue circle indicates +CG. The −CG lightning dominates throughout its whole lifetime. Cell B separates from Cell A at 17:50. Cell A, which produced a downburst, moved to the northeast, and Cell B moved to the southeast. After that, Cell B got out of the area of analysis at 18:20. The lightning activity started at 14:00, and it has two peaks at 17:40 and 18:40. The distribution of the lightning locations varied as time advances. The lightning locations are distributed on the east side of intensive rain area at 17:30 and 18:20. On the other hand, the locations are distributed around the center of the intensive rain area at 17:40, 18:30 and 18:40. When the downburst occurred on the surface at 18:00, the lightning locations of Cell A are distributed around the center and the east side of intensive rain area. The lightning activity rapidly weakened after 19:00.
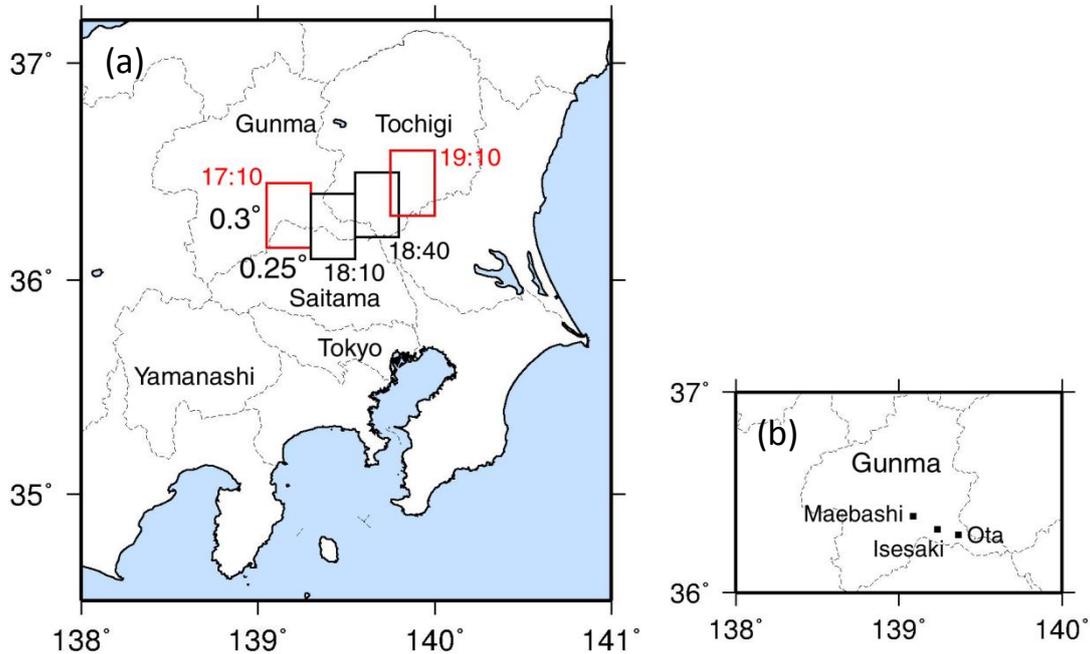

Figure 4.9. (a) Area of analysis on the July 11, 2013 from 17:10 to 17:10 (JST). (b) Map of Gunma prefecture.
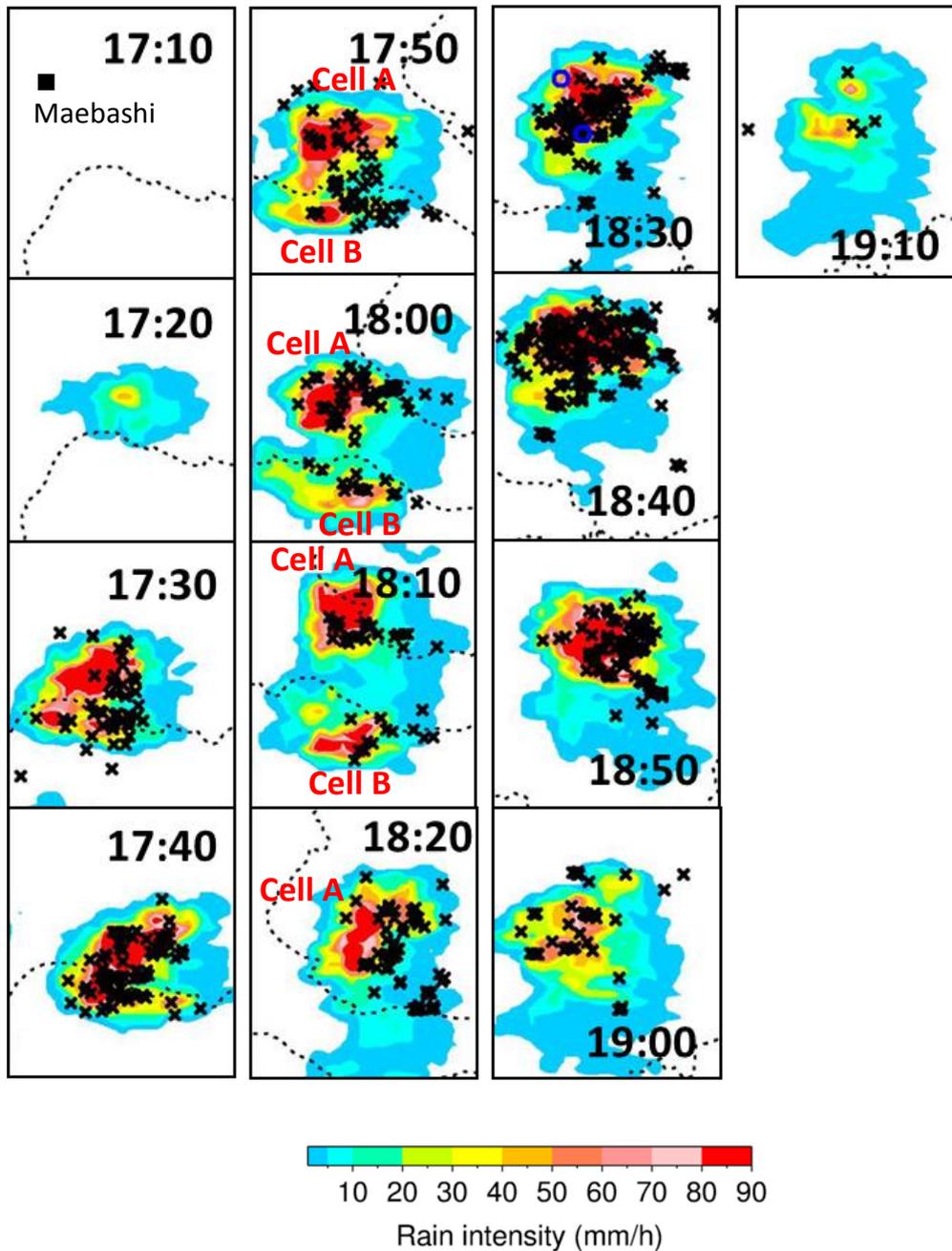
Figure 4.10. Evolution of the precipitation area on July 11, 2013 from 17:10 to 19:10 (JST). The CG lightning flash location during a 10 min period centered on the radar time are plotted. The black cross indicates a negative CG. The blue circle indicates a positive CG.

Figure 4.11 shows the time series of the –CG and +CG flash rates, IC flash rate, rain volume and area size of echo height more than 12 km in the period from 17:20 to 19:10 on July 11, 2013. The bar graph in Figure 4.11 displays the rain volume calculated over 10-min interval. The blue line, red line, and dashed line display –CG flash rate, +CG flash rate, IC flash rate, respectively. The green line displays the area size of echo height more than 12 km, calculated over 10-min interval. This thunderstorm produced 1,062 flashes of –CG, 2 flashes of +CG and 112 flashes of IC throughout its whole lifetime. The averaged values of peak current are –15.0 kA for –CG and 19.0 kA for +CG, respectively. The –CG lightning dominated throughout its whole lifetime.

This thunderstorm roughly has two peaks of –CG flash rate at 17:40 and 18:40. The first peak of flash rate is 49 events per 5 minutes at 17:40, and that of second peak is 127 events per 5 minutes at 18:40. The brief decreasing of the rain volume and the area size of radar echo height more than 12 km at 18:20 is caused by Cell B which moves to outside of area of analysis. The peak of the rain volume is approximately 1.6×10^6 mm^3 per 5 minutes at 18:40. The peak of the area size of radar echo height more than 12 km is 48 km^2 at 18:50. The second peak of –CG flash rate is two and a half times larger than that of the first peak. The peak of –CG flash rate is shifted in advance by about 10 minutes as compared to the peak of the area size of radar echo height more than 12 km.

According to JMA reports, the downburst occurred on the surface at around 18:00. The flash rate of –CG decreases in advance of the occurrence of downburst on the surface (about 10 minutes). After that, the –CG flash rate briefly increases from 17:50 to 18:00. On the other hand, the area size of rain echo height more than 12 km is continuously increasing, and the rain volume stays during the same period. There is no change in +CG flash rate and no apparent change in IC flash rate.

Figure 4.12 shows the time series of the –CG and +CG flash rates, IC flash rate, area size of intensive rain more than 50 mm/h and area size of echo height more than 12 km during the same period. The bar graph in Figure 4.11 displays the area size of intensive rain more than 50 mm/h, and the lines in Figure 4.12 are same as in Figure 4.11. The peak of area size more than 50 mm/h is 68 km^2 at 18:40. The area size of intensive rain shows similar variation to rain volume.
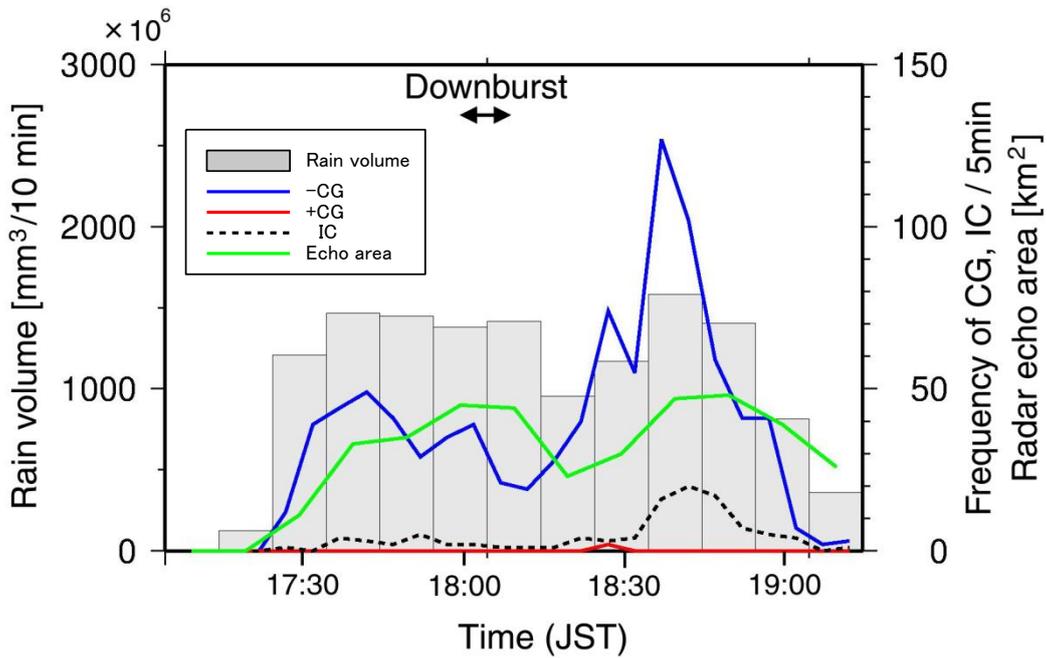
Figure 4.11. Evolution of the rain volume, area of echo height more than 12 km and lightning flash rate on July 11, 2013 from 16:40 to 19:10 (JST).
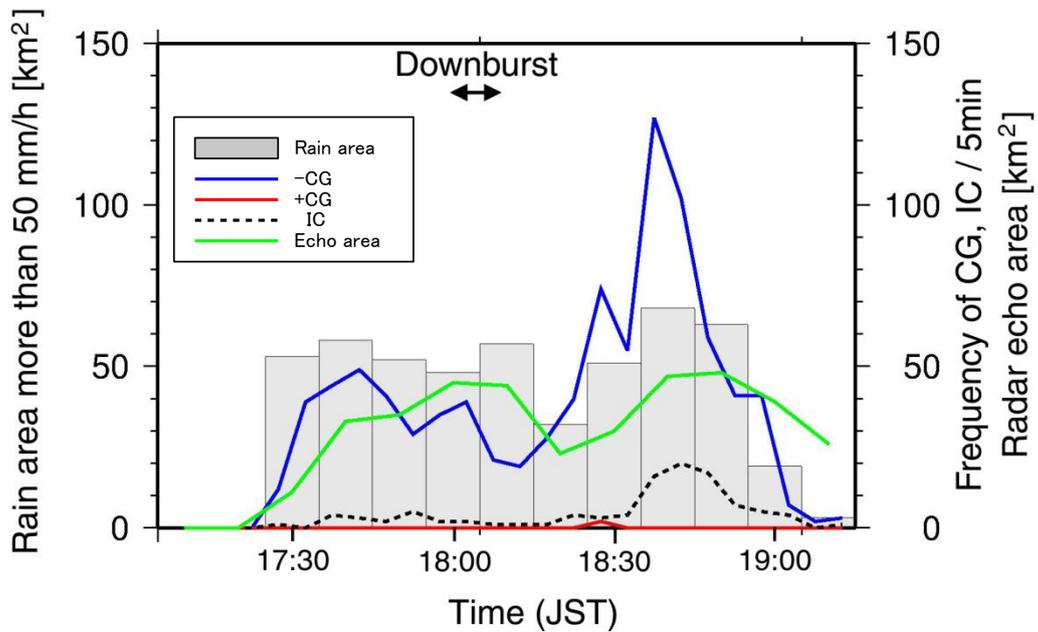

Figure 4.12. Evolution of the rain area more than 50 mm/h, area of echo height more than 12 km and lightning flash rate on July 11, 2013 from 17:10 to 19:10 (JST).

Figure 4.13 shows the time variation of frequency distribution of (a) iCMC, (b) peak current of JLDN and (c) duration time (T_3) of electric fields in the period from 17:30 to 19:10 on July 11, 2013. All of the events shown in Figure 4.13 is –CG. These events are distributed over 10-min interval. The detection efficiency of iCMC in this period with respect to the events detected by JLDN is 71 %. The average value of iCMC is –7.1 C·km.

The number of events with iCMC more than 5 C·km in absolute value increases and are distributed widely for iCMC with development of the thunderstorm. The occurrence frequency of higher value of iCMC in absolute value increases from 17:30 to 17:40 and from 18:20 to 18:40. Especially, the number of events with iCMC in absolute value more than 20 C·km increases at 18:40 when the occurrence frequency of –CG reaches its peak as shown in Figure 4.11. The distributions of the peak current and the duration time of electric field also vary with development of thunderstorm. The events with peak current more than 15 kA in absolute value increase and are distributed widely for peak current from 17:30 to 17:40 and from 18:20 to 18:40. The events with duration time of electric field (T3) more than 200 μs indicate the similar variation to that of iCMC and peak current.

On the other hand, the events with iCMC in absolute value more than 5 C·km decrease before and after the occurrence of the downburst on the surface from 17:50 to 18:10. Especially, the events with iCMC in absolute value more than 5 C·km decrease after the occurrence of the downburst at 18:10. The distributions of the peak current more than 15 kA in absolute value and the duration time of electric field more than 200 μs also indicate the similar variation to that of iCMC during the period.
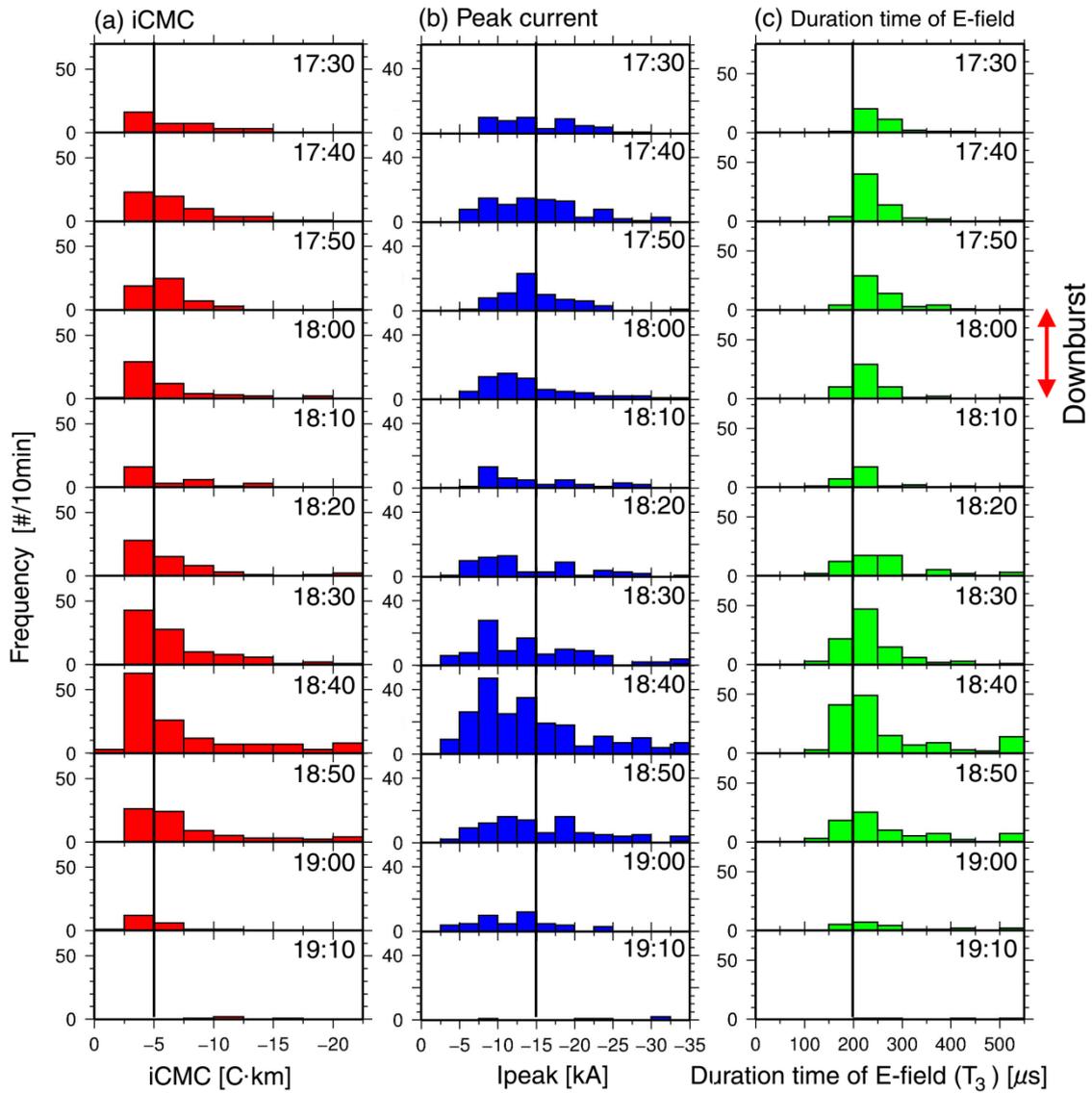
Figure 4.13. Time variation of frequency distribution of (a) iCMC, (b) peak current and (c) duration time of electric field (T_3) on July 11, 2013 from 17:30 to 19:10 (JST).

4.3.3 Case of August 11, 2013 (Case 3)

The thunderstorm occurred in the period from 16:40 to 19:30 on August 11, 2013. The weather conditions in this case was verified. Figure 4.14 shows the surface weather chart at 09 h (JST), August 11, 2013. The high-pressure system (described as H in Figure 4.14) in the Pacific Ocean overlies Kanto region. Figure 4.15 and Figure 4.16 show the 500-hPa level upper weather chart at 09 h (JST) and at 21 h (JST), August 11, 2013, respectively. The black line is the isohypse, color contour is the air temperature at 500 hPa at isobaric surface. These 500-hPa level upper weather chart show no significant change in the contour and the temperature in Kanto region. There is no synoptic scale disturbance. According to JMA reports, the temperature went up to more than 35 °C at many AMeDAS sites in Kanto region, and reached new record of all-time high at 47 AMeDAS sites throughout Japan. The thunderstorms occurred over a wide range of Kanto from the early afternoon. In addition, according to report of the Maebashi local meteorological observatory, a downburst occurred at around 18:00–18:30 (JST) in Takasaki and Maebashi, Gunma (Figure 4.17 (b)). The both downbursts were estimated as F1 (33-49m/s).
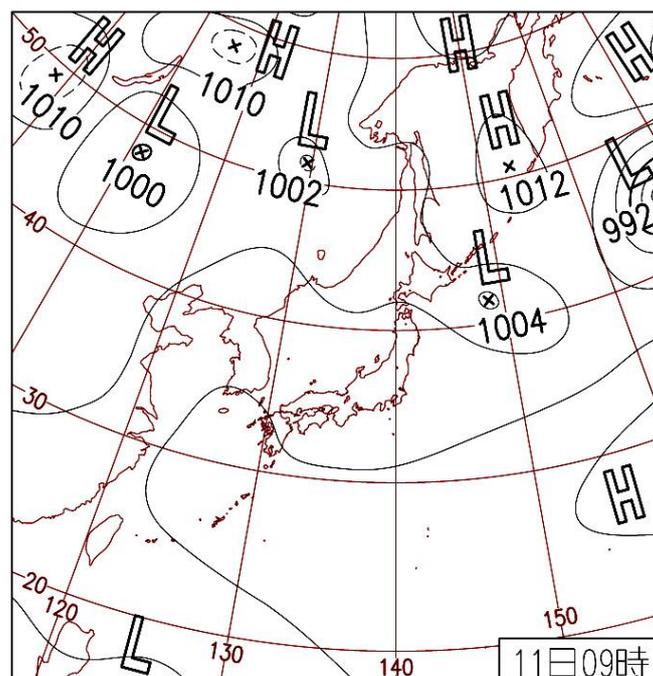
Figure 4.14. Surface weather chart at 09 h (JST), August 11, 2013.
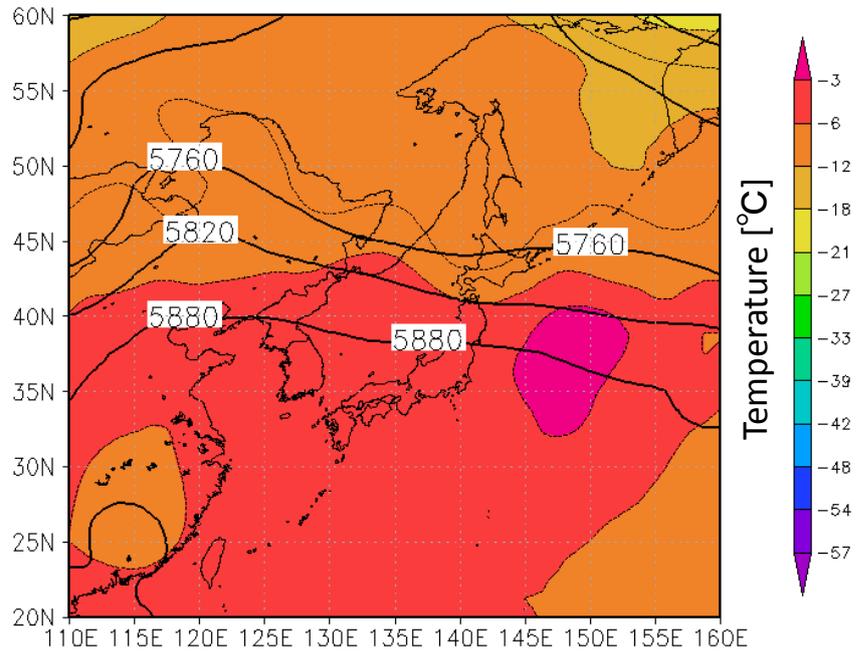
Figure 4.15.   500-hPa level upper weather chart at 09 h (JST), August 11, 2013. The black line is isohypse, color contour is an air temperature at 500 hPa at isobaric surface.
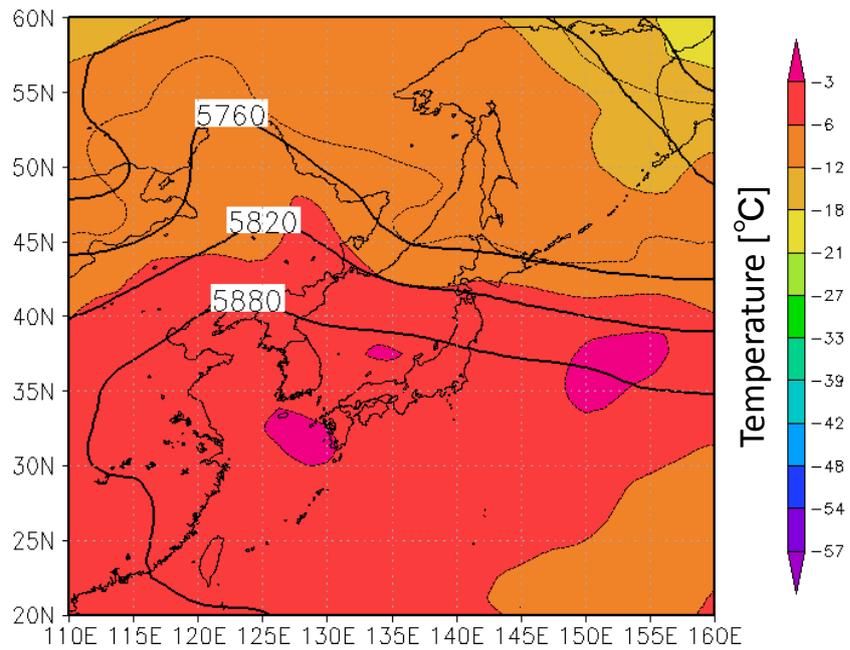
Figure 4.16.   500-hPa level upper weather chart at 09 h (JST), August 11, 2013. The black line is isohypse, color contour is an air temperature at 500 hPa at isobaric surface.

The period of analysis ranged from 16:40 to 19:30. The area of analysis was confined within a dimension of 0.4° in the longitudinal direction by 0.35° in the latitudinal direction. The considered thunderstorm moved from west to east in the northern part of Kanto region. Figure 4.17 (a) shows the area of analysis in the period from 16:40 to 19:40 on August 11, 2013.

Figure 4.18 shows the evolution of the rain area in the period from 16:40 to 19:00 on August 11, 2013. The rain intensity is color shaded as shown, the altitude is gray shaded, and dashed line is a border between prefectures. The CG lightning flash locations during a 10-min period centered at the radar time are plotted. The black cross and blue circle indicates –CG and +CG, respectively. Cell B separated from Cell A at 17:10. Cell A, which produced a downburst, moved to the east, and Cell B moved to the southeast. Cell B got out of the area of analysis at 17:20. The lightning activity started at 17:00 and reached its peak at 18:00. The –CG lightning dominates from 17:00 to 18:10, and the +CG lightning dominates from 18:20 to 18:30. The lightning locations are distributed around the east side of intensive rain area at 17:10, 17:20, and 17:40. On the other hand, the lightning locations are distributed around the center of intensive rain area at 18:00, 18:20 and 19:00. When the downburst occurred on the surface from 18:00 to 18:30, the lightning locations are distributed around the center of the intensive rain area or near the intensive rain area.
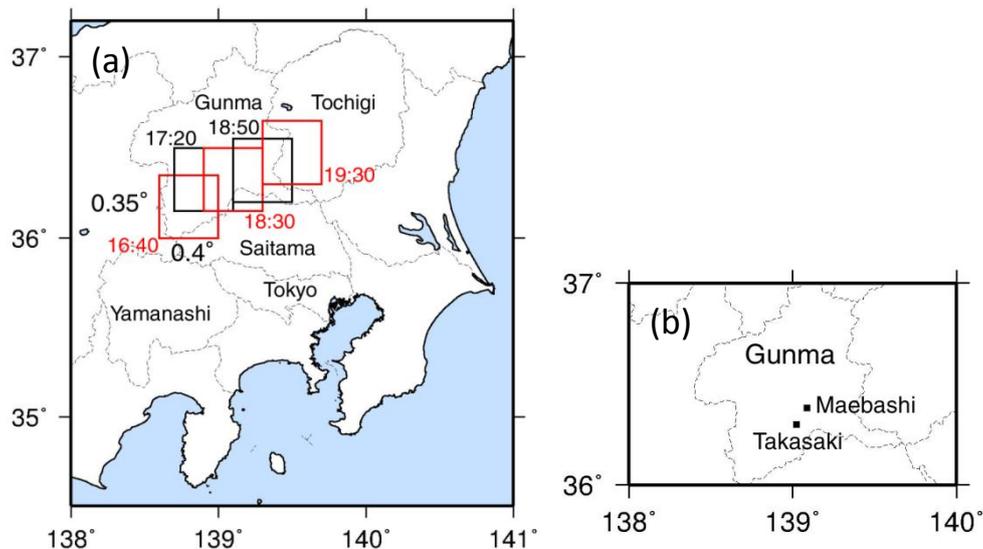
Figure 4.17. (a) Area of analysis on the August 11, 2013 from 16:40 to 19:40 (JST). (b) Map of Gunma prefecture.
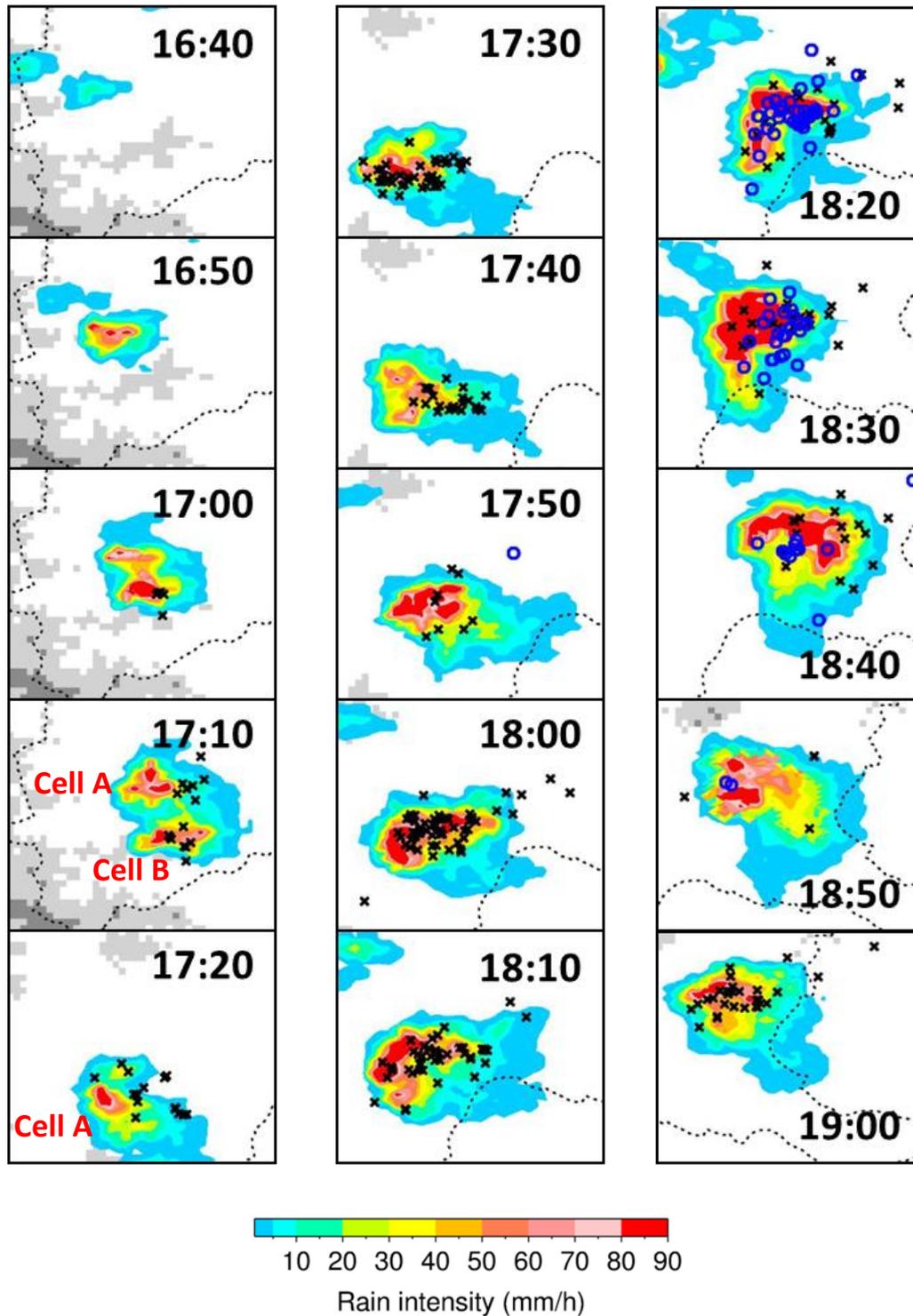
Figure 4.18. Evolution of the precipitation area on August 11, 2013 from 16:40 to 19:30 (JST). The CG lightning flash location during a 10 min period centered on the radar time are plotted. The black cross indicates a negative CG. The blue circle indicates a positive CG.

Figure 4.19 shows the time series of the –CG and +CG flash rates, IC flash rate, rain volume and area size of echo height more than 12 km in the period from 16:40 to 19:40 on August 11, 2013. The bar graph in Figure 4.19 displays the rain volume calculated over 10-min interval. The blue line, red line, and dashed line displays –CG flash rate, +CG flash rate, and IC flash rate, respectively. The green line displays area size of echo height more than 12 km, calculated over 10-min interval. This thunderstorm produced 322 flashes of –CG, 65 flashes of +CG and 300 flashes of IC throughout its whole lifetime. The number of +CG and IC flashes were clearly more than Case (1) and Case (2) on July 11, 2013. The averaged values of peak current are –12.6 kA in –CG and 61.6 kA in +CG, respectively. The value of averaged peak current of +CG is larger than Case (1) and Case (2).

The time series of lightning flash rates shows complex change. This thunderstorm has prominent three peak of –CG flash rate at 17:30, at 18:00, and at 19:00. The first, second and third peak of –CG flash rate is 25 events per 5 minutes, 50 events per 5 minutes, 21 events per 5 minutes, respectively. The –CG lightning activity dominated from 17:00 to 17:40. The +CG flash rate rapidly increases at 18:20, and +CG lightning activity finish at 18:50. The IC flash rate rapidly increases from 17:40 to 17:50. The IC activity shows similar variation to the –CG lightning activity after 18:00. The peak of rain volume is approximately 2.3×10^9 mm^3 per 10 minutes at 18:30. The brief decreasing of the rain volume at 17:20 is caused by Cell B which moved to outside of area of analysis. The area of radar echo height more than 12 km increases from 16:40 to 19:00. The peak of the area size is 135 km^2 at 19:00.

According to JMA reports, the downburst occurred on the surface in the period from 18:00 to 18:30. The –CG flash rate rapidly and clearly decreases in advance of the occurrence of downburst on the surface (about 10 min). After that, –CG flash rate rapidly and briefly increases at 18:00. In addition, IC flash rate increases in advance of the occurrence of downburst on the surface and increasing –CG flash rate at 17:50. –CG flash rate rapidly decreases from 18:00 to 18:20, then +CG rapidly increases from 18:10 to 18:20. On the other hand, the rain volume and the area size of rain echo height more than 12 km are continuously increasing before and after the occurring of the downburst.
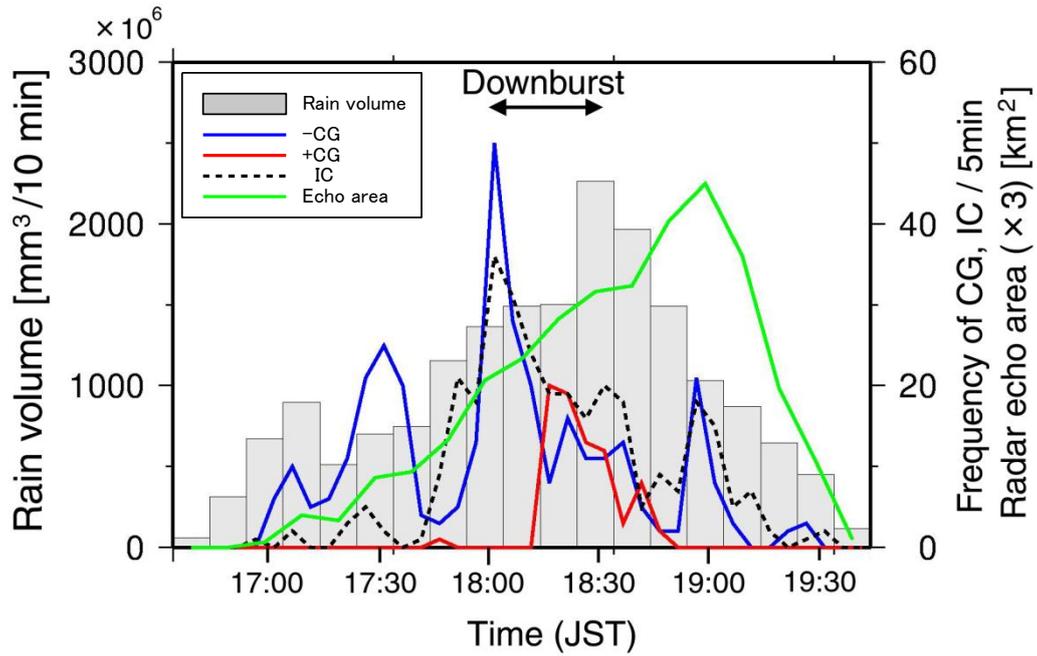
Figure 4.19. Evolution of the rain volume, echo top area and lightning flash rate on August 11, 2013 from 16:40 to 19:10 (JST).
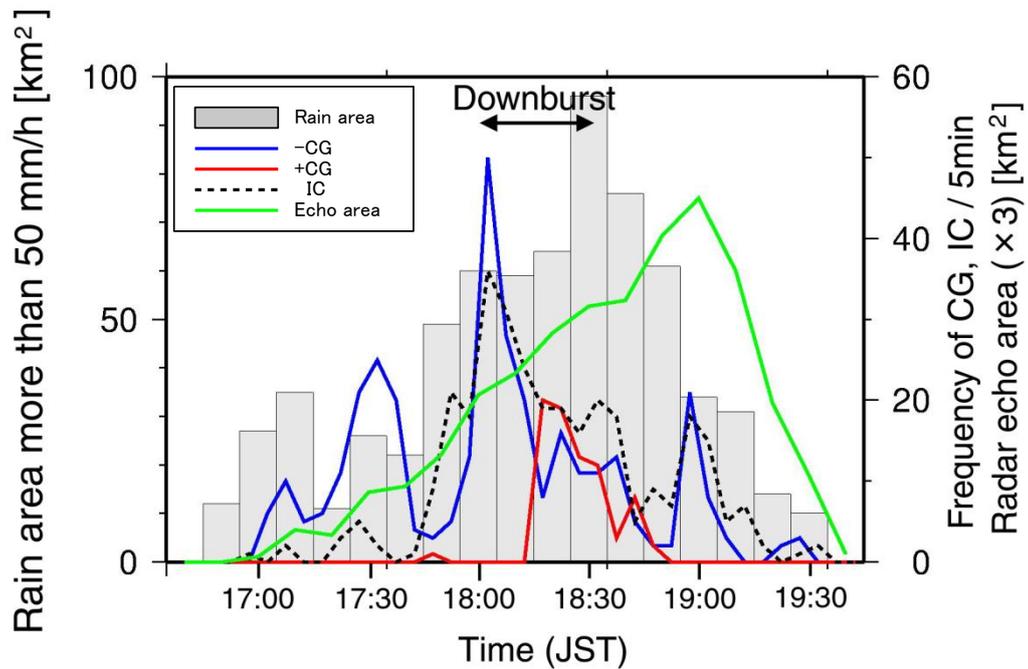
Figure 4.20. Evolution of the rain area (more than 50 mm/h), echo top area and lightning flash rate on August 11, 2013 from 17:10 to 19:10 (JST).

Figure 4.20 shows the time series of the –CG and +CG flash rates, IC flash rate, area of intensive rain more than 50 mm/h and area size of echo height more than 12 km during the same period. The bar graph in Figure 4.19 displays area size of intensive rain more than 50 mm/h, and the lines in Figure 4.20 are same as in Figure 4.19. The brief decreasing of the intensive rain area at 17:20 is caused by Cell B which moved to outside of the area of analysis. The peak of the intensive rain area size is 96 km^2 at 18:30. The intensive rain area shows quite similar variation to the rain volume as shown in Figure 4.19.

Figure 4.21 shows time variation of frequency distribution of (a) iCMC, (b) peak current estimated by JLDN and (c) duration time (T_3) of electric fields in the period from 17:00 to 18:50 on August 11, 2013. All of the events shown in Figure 4.21 is –CG. These events are distributed over 10-min interval. The detection efficiency of iCMC in this period with respect to the events detected by the JLDN is 75 %. The averaged value of iCMC is 6.1 C·km.

The ratio of iCMC more than 5 C·km in absolute value increases from 17:10 to 17:30, and that increases and are distributes widely for iCMC with development of the thunderstorm as shown in Figure 4.18 and 4.20. The distribution of peak current more than 15 kA in absolute value and duration time of electric field more than 200 μs also increase with the development of thunderstorm.

This thunderstorm produced the downburst on the surface from 18:00 to 18:30. The events with iCMC more than 5 C·km in absolute value clearly decrease after 18:10. The period is close agreement with time of occurrence of downburst. The events with the peak current more than 15 kA in absolute value clearly decrease after 18:20. The events with the duration time of electric field more than 250 μs also decrease after 18:20.
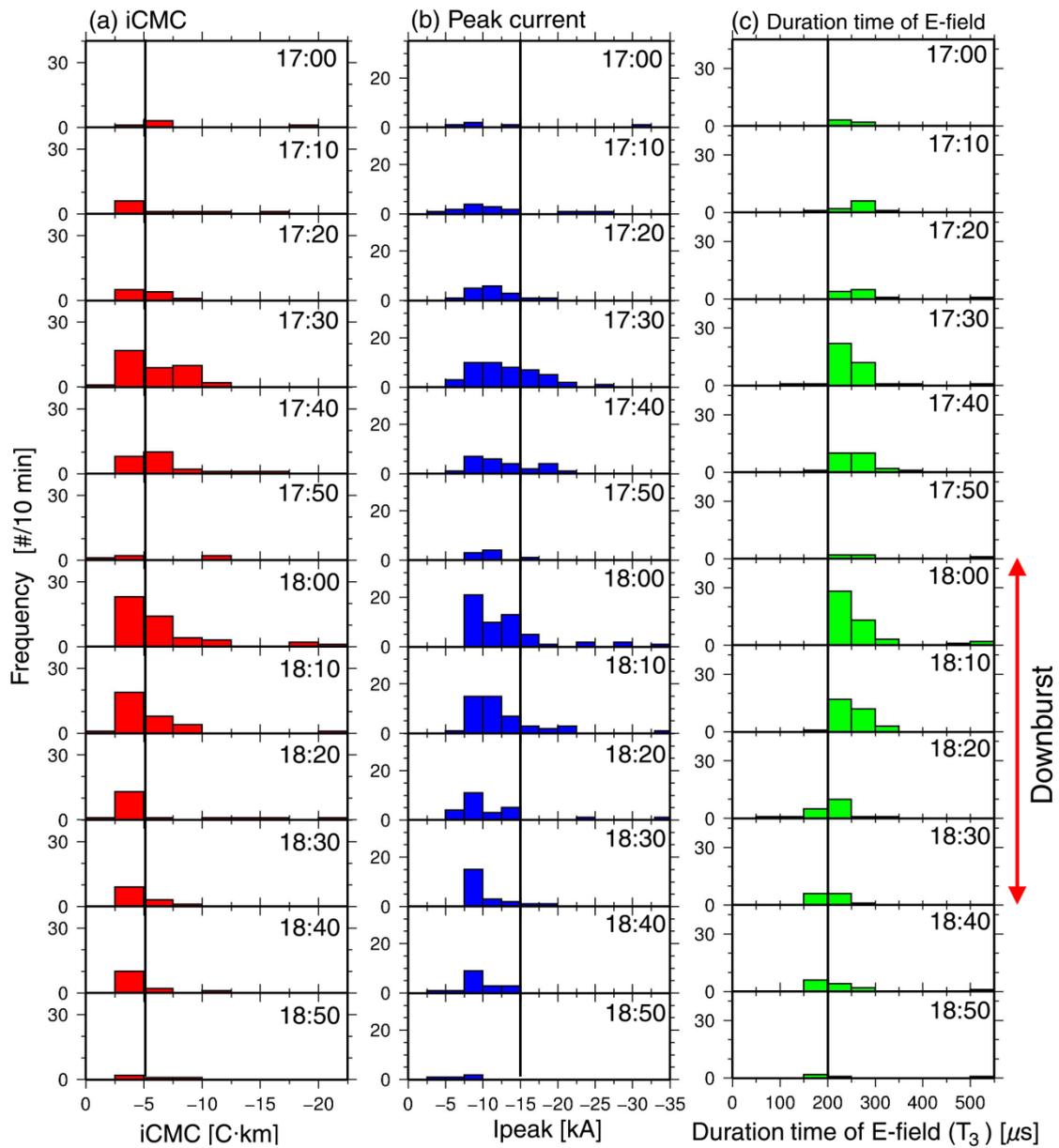
Figure 4.21. Time variation of frequency distribution of (a) iCMC, (b) peak current and (c) duration time of electric field (T_3) on August 11, 2013 from 17:00 to 18:50 (JST).

4.4 Discussion

4.4.1 Lightning magnitudes and a development process of thunderstorm

The relationships between the rain volume, the area size of radar echo height more than 12 km and iCMC were examined for 3 cases. The 3 cases analyzed in this thesis show the time variations of distribution of iCMC with the development of thunderstorm. The ratio of iCMC intensity more than 5 C·km increased during the period when thunderstorm develops. The iCMC is multiplication of two physical values, namely, amount of neutralized charge of CG lightning and its altitude (discharge length). Figure 4.22 shows schematic diagram of the inferred relationship between thunderstorm evolution and the distribution of electrical charges. The left-hand panel shown in Figure 4.22 indicates thunderstorm at early stage and the right-hand that at well-developed phase. It is possible that the discharge length of well-developed thunderstorm (dl2) is longer than that of thunderstorm of early stage (dl1) as shown in Figure 4.22 (a), or that charge in the well-developed thunderstorm (Q2) is larger than that of thunderstorm of early stage (Q1) as shown in Figure 4.22 (b). Strong updraft in the developed thunderstorm carries charged precipitation particles to higher altitude or well-developed thunderstorm generates larger charge pool in the cloud. It is reported that storms which have high updraft speeds also have high CG lightning rates and that higher updraft carry precipitation particles (supercooled drops, hail and graupel) to higher altitudes [*Gungle and Krider*, 2006]. This suggestion supports both hypotheses shown in Figure 4.22. *Kamra and Pawar* [2007] suggested that charging region is lifted up in mature stage of the thunderstorm by strong updraft. This suggestion supports the hypothesis described in Figure 4.22 (a).

Table 4.1 shows characteristics of the –CG and +CG flashes produced by the thunderstorms analyzed in this thesis. The thunderstorm of Case (2) produced much more number of –CGs than other two thunderstorms, and iCMC and peak current in the Case(2) are high (7.1 C·km and 15 kA in absolute value). On the other hand, the thunderstorm of Case(3) produced much more number of +CGs than other two

thunderstorms. Both thunderstorms produced the downburst, however, each CG activity was different. The 3 thunderstorms analyzed in this thesis have different averaged value of iCMC and peak current. *Cummer and Lyons* [2004] found that each thunderstorm has a different distribution of CMC (within 2 ms) from the result of ELF measurements in U.S. high plains.

Table 4.2 shows view of the peak value of the rain volume per 5-min, area of rain intensity more than 50 mm/h and area of radar echo height more than 12 km. These peak value estimated by meteorological radar data are not correlated with the average value of iCMC, peak current and occurrence frequency of −CG. Some of previous studies [*Montanya et al.*, 2007; *Soula et al.*, 2004] reported that the average value of peak current of −CGs in hailstorms are low (approximately 10–12 kA in absolute value). It is likely that the averaged value of the peak current is not directly related with the thunderstorm activity in this thesis.
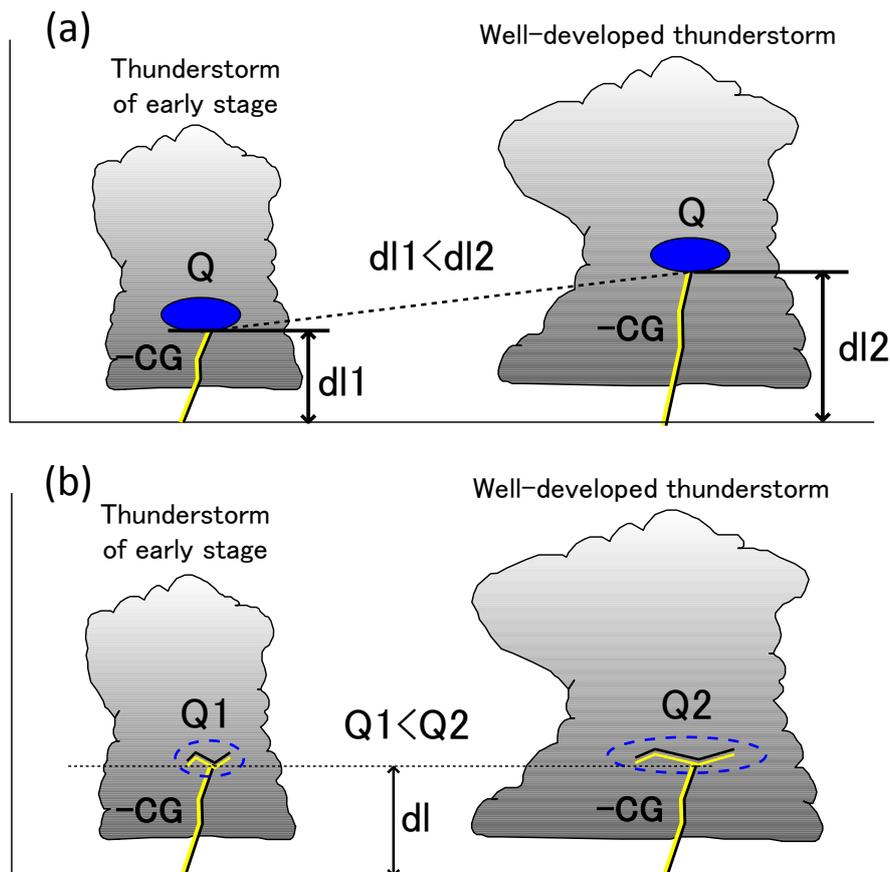
Figure 4.22. Schematic diagram of inferred relationship between the thunderstorm evolution and distribution of electrical charges.

Table 4.1. Characteristics of the –CG and +CG flashes produced by the thunderstorms analyzed in this thesis.

Date of event	–CG			+CG	
	Number of flash	Averaged value of iCMC	Averaged value of I_{peak}	Number of flash	Avaraged value of I_{peak}
July. 11, 2013 Case (1)	198	5.6 C·km	−13.1 kA	3	+21.3 kA
July. 11, 2013 Case (2)	1,062	7.1 C·km	−15.0 kA	2	+19.0 kA
August. 11, 2013 Case (3)	322	6.1 C·km	−12.6 kA	65	+61.6 kA

Table 4.2. View of the peak value of the rain volume, rain area and radar echo area produced by the thunderstorms analyzed in this thesis.

Date of event	Peak value of		
	Rain volume per 10-min	Area size of rain intensity more than 50 mm/h	Area size of radar echo height more than 12 km
July. 11, 2013 Case (1)	1.3×10^9 mm^3	48 km^2	22 km^2
July. 11, 2013 Case (2)	1.6×10^9 mm^3	68 km^2	48 km^2
August. 11, 2013 Case (3)	2.3×10^9 mm^3	96 km^2	135 km^2

4.4.2   Lightning activities and downburst

The thunderstorm of Case (2) and Case (3) produced downburst. The time variation of lightning flash rates and that of the occurrence frequency distribution of iCMC were examined. It is found that –CG flash rate decreases in advance of occurrence of the downburst on the surface (about 10 minutes) in both cases. IC flash rate increased in

advance of increase in –CG flash rate in Case (3). Some studies found that total lightning activity (IC+CG) observed by VHF band rapidly often increases in advance of severe weather (tornado, downburst and hail) [*Williams et al.*, 1999: *Goodman et al.*, 2005; *Schultz et al.*, 2009; *MacGorman et al.*, 2012]. The aspect of increase in total lightning activity is called as lightning jump. The IC flash rate in Case 3 in this study is in agreement with their results. *Metzeger* [2010] reported that in most of tornado or downburst-producing thunderstorm IC flash rate increase while CG flash rate increases in advance of occurrence of tornado or downburst (wind type lightning jump). Metzeger [2010] also reported that most of hail-producing thunderstorm shows that IC flash rate increase while CG flash rate decreases in advance of occurrence of hail (hail type lightning jump). The results of the two downburst-producing thunderstorm in this thesis disagree with characteristics of wind type lightning jump reported by *Metzeger* [2010]. However, our results agree with characteristics of hail type lightning jump.

After occurrence of the downburst on the surface, the −CG flash rate decreased and the +CG flash rate increased in Case(3). The ratio of iCMC intensity more than 5 C·km clearly decreased during the period of occurrence of downburst on the surface.

These time variations of lightning activities are explained by Figure 4.23 and Figure 4.24. Figure 4.23 shows time history of the vertical motion of the largest most reflective precipitation particles during the evolution of the downburst-producing downdraft [*Fujita*, 1992]. Strong updraft carries rapidly the large precipitation particles (graupel and hail) upward. The large precipitation particles further evolve and those become heavy. Those large precipitation particles cause downdraft. According to *Wakimoto and Bringi* [1988], the center of the microburst (downburst) damage at the surface is well-correlated with the distribution of hail estimated by the observations of the multiparameter radar.

Figure 4.24 shows the time variations of inferred vertical motion of charge and lightning activities in the downburst-producing thunderstorm. Blue and red circles display negative and positive charge center, respectively. Black arrow displays updraft, and thick aqua arrow displays downdraft. Color bars indicate which type of lightning activity dominates. Blue, red and green bar show the –CG, +CG and IC activity. Yellow

bar shows the period of occurrence of downburst at the surface. Blue line indicates the time variation of iCMC.

As shown in Figure 4.24 (b), the strong updraft carries rapidly the negatively-charged large precipitation particles at high altitude. The ratio of iCMC more than 5 C·km in absolute value increases with the development of thunderstorm at this time. The distance between positive and negative charge center decreases. Therefore, the IC flash rate increases, and the –CG flash rate decreases. After that, developed downdraft carries the negatively-charged large precipitation particles as shown in Figure 4.24 (c) and (d). When the distance between the positive and the negative center increases, the –CG flash rate increases and the IC flash rate decreases (Figure 4.24 (d) and (e)). *MacGorman et al.* [1989] suggested that the peaks in ground flash rates result from increasing the distance between the main positive and negative charge centers, from the sedimentation of negative charge. The relationship between the evolution of downburst and the timing of enhancement of IC and CG activities was suggested by *Williams et al.* [1989]. The results of this thesis support these suggestions. *Kuhlman et al.* [2010] found that the 8 microburst producing storms in central Oklahoma, U.S. have a tripole charge structure, and lightning flashes generally occur between upper positive charge region and middle level negative charge region in advance of occurrence of the downburst. Although the results in this thesis cannot present whether the microburst-producing storm has a tripole charge structure, our hypothesis agrees in that the IC flashes occur between the upper positive charge region and negative charge region in advance of the downburst at the surface. The negative charges fall with the large precipitation particles with strong downdraft as shown in Figure 4.24 (f), or those are decreased by IC and –CG discharges. The amount of remaining negative charge in the cloud is small, then the ratio of iCMC more than 5 C·km in absolute value clearly decreased (blue line shown in 4.24). In Figure 4.25 the stages (a)~(f) described in Figure 4.24 are superimposed on Figure 4.19 (left panel) and on Figure 4.21 (a), respectively. The time variation of inferred vertical motion of charge and lightning activities in the downburst-producing thunderstorm, shown in Figure 4.24, is coincident with the results of Case 3 which occurred on August 11, 2013.
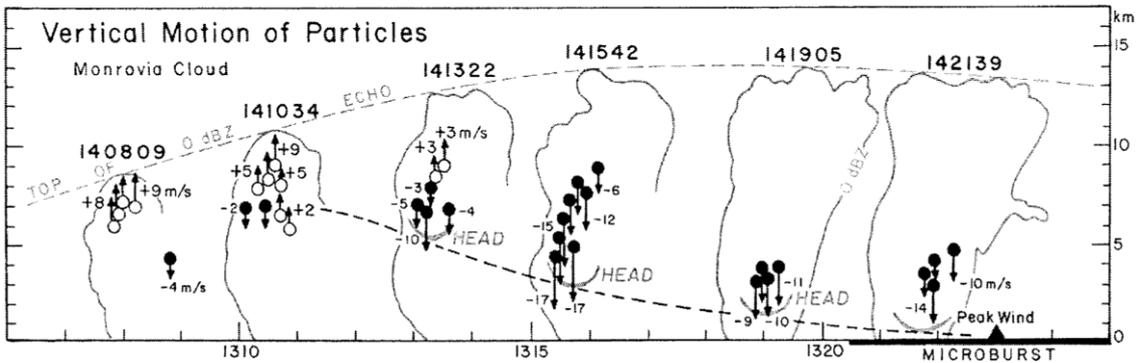
Figure 4.23. Time history of the vertical motion of the largest most reflective precipitation particles during the evolution of the downburst-producing downdraft [*Fujita*, 1992].
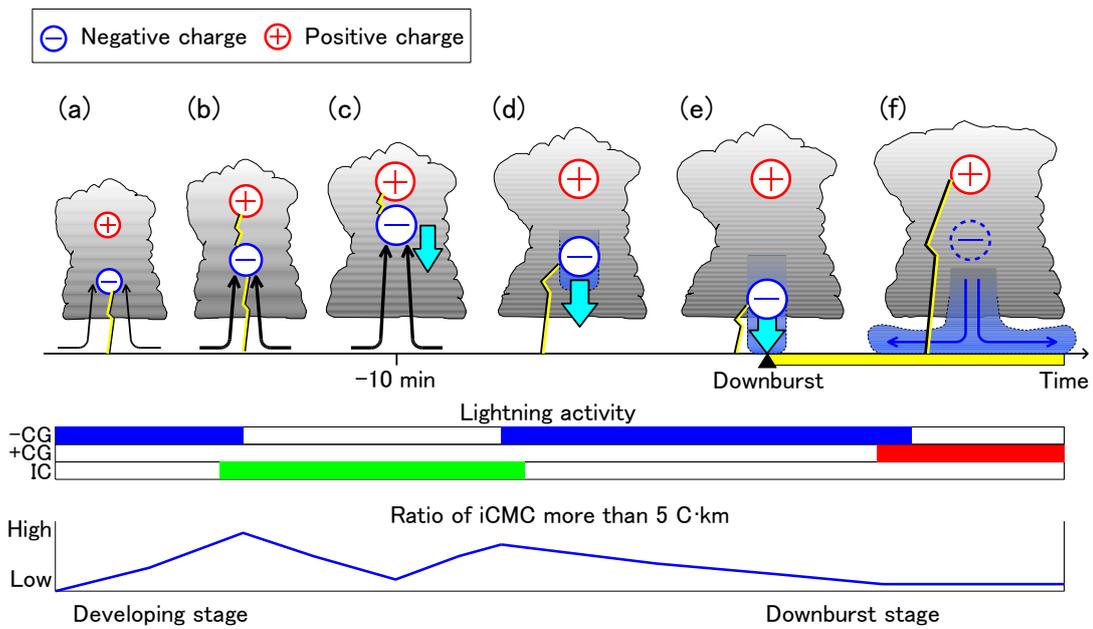
Figure 4.24. The time variation of inferred vertical motion of charge and lightning activities in the downburst-producing thundercloud. Blue circles and red circles display negative and positive charge center, respectively. Black arrow displays updraft, and thick aqua arrow displays downdraft. Color bars indicate which type of lightning activity dominate. Blue, red and green bar show the –CG, +CG and IC activity. Yellow bar shows the period of occurrence of the downburst at the surface. Blue line indicates the time variation of the ratio of iCMC more than 5 C·km in absolute value.
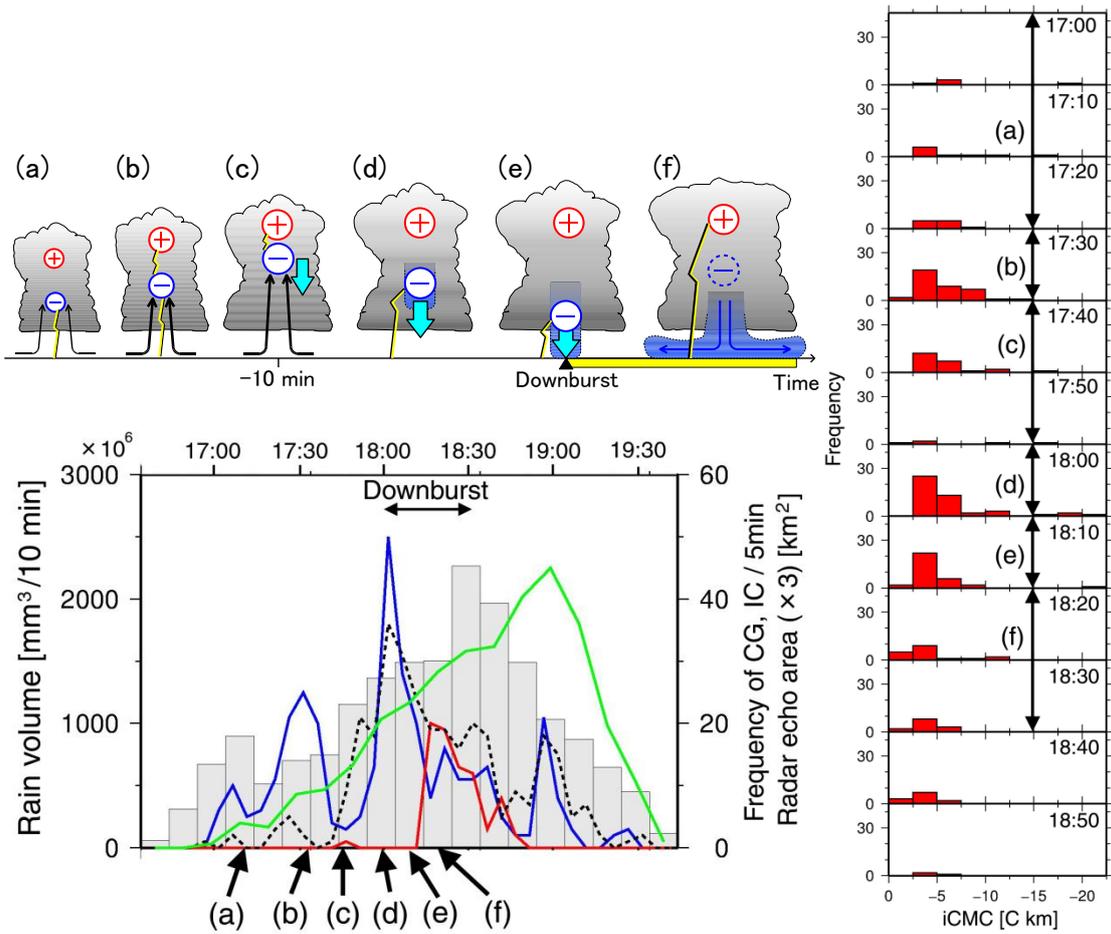
Figure 4.25. Stages (a)~(f) shown in Figure 4.24 superimposed on Figure 4.19 (left panel) and on Figure 4.21 (a) (right panel), respectively.

4.5 Summary and conclusion

The relationship among the time variation of rain volume, the area size of radar echo height more than 12 km and the lightning parameters for the 3 cases was examined using the estimated iCMC, the peak current and the duration time of electric field waveform. The rain volume and the area size of radar echo height more than 12 km are calculated using the JMA C-band radar data every 10 minutes. It is found that absolute value of iCMC of –CG increases as occurrence frequency of –CG, the area size of the radar echo height more than 12 km and rain volume increase, i.e., with the development of thunderstorm. The time variations both of the peak current and the duration time of electric field enhancement show a similar variation. The peak value of the rain volume per 10-min, area size of rain intensity more than 50 mm/h and area size of radar echo height more than 12 km, which are estimated by meteorological radar data, are not correlated with the averaged value of iCMC, peak current and occurrence frequency of –CG in this thesis.

It is found that the occurrence frequency of –CG shows temporal decreases in advance of the occurrence of downburst on the ground by ~15 minutes, while the area size of radar echo height more than 12 km is continuously increasing. It is possible that large negatively-charged precipitation particles (hail and graupel) carried upward by strong updraft approach the positively-charged particles (ice crystal), then the occurrence frequency of –CG decrease. In addition, it is found that –CG with iCMC less than 5 C·km in absolute value is dominant in the occurrence time period of the downburst on the surface. It is possible that negatively-charged graupels and hails fall to the ground with the downburst, or negative charges decrease by IC and –CG activities, and the occurrence frequency of –CG with iCMC less than 5 C·km in absolute value increase.

Chapter 5

Conclusion and suggestions for future work

5.1 Conclusion

The purpose of this thesis is to establish the methods of analysis to estimate small charge moment change (CMC) of –CG and to investigate the relationship between developing process of thunderstorm and lightning activity with impulsive CMC (iCMC) of each lightning stroke. This thesis deals with three subject: 1) development of a new VLF observation system in Kanto region, Japan and its continuous operation, 2) establishment of the methods of analysis to estimate iCMC of –CG and peak current from VLF waveform, 3) investigation of the relationship between meteorological parameters and lightning activity with information of magnitudes.

A new VLF lightning observation system was developed. A continuous monitoring of waveform in frequency range of 2 kHz – 35 kHz at three stations in Kanto region located in the range of 150 km from Tokyo, Japan, has been carried out for the first time. Kanto region is the one of the best location to investigate the relationship between the meteorological parameters and the lightning activity in the world because of existing the dense meteorological observation networks. The observation system with three observation sites has been operated since May 15, 2013.

Lightning peak current and iCMC (CMC with a duration of 1 ms or less) were estimated from VLF data. In order to estimate the peak current from VLF waveform, the relationship between peak current estimated by Japan Lightning Detection Network (JLDN) and normalized amplitude of electric field waveform was investigated. It is

shown that high correlation between the peak current of JLDN and the normalized amplitude in the range of 50–200 km ($R^2 = 0.79$). The methodology to estimate peak current using waveform in VLF band, which is detectable at far distance than that in LF band was established. A new method of estimation of iCMC without use of frequency analysis nor VLF propagation model was established. The iCMC is estimated using the duration time of electric field of groundwave identified from the VLF waveform and peak current. The method contributes to suppression of the calculation amount for estimating iCMC, which may make it possible to calculate lightning magnitudes in a short period for real-time alert. The data of 10,606 VLF sferics observed at Yamanashi site (35.669°N, 138.581°E) at the distance from 50 to 200 km were analyzed, then the numbers of estimated iCMC of –CG and +CG were 7,418 and 57, respectively. The detection efficiency (DE) of iCMC estimation of –CG in this study is about 72 %, while the estimated DE of current systems for iCMC or peak current using VLF are less than 11 %. The DE of VLF lightning observation system for estimation of iCMC is the highest level in the world. The relationship between iCMC and the peak current estimated from VLF data was examined. It is found that correlation between iCMC over 20 C·km and the peak current is small ($R^2 = 0.21$), and correlation between iCMC less than 20 C·km and the peak current is high ($R^2 = 0.69$). These results suggest that iCMC cannot be estimated from the peak current for the event over 20 C·km. It is necessary to estimate iCMC more than 20 C·km from the time variation of waveform.

The relationship among the time variation of rain volume, the area size of radar echo height more than 12 km and lightning parameters for the 3 cases was examined using the estimated iCMC, peak current and the duration time of electric field waveform. The rain volume and the area size of echo height more than 12 km were calculated using the Japan Meteorological Agency (JMA) C-band radar data every 10 minutes. It is found that the absolute value of iCMC of –CG increases as occurrence frequency of –CG, the area size of the radar echo height more than 12 km and rain volume increase, i.e., with the development of thunderstorm for the first time in the world. One possibility is that the negative charges in the cloud are carried upward by updraft or many negative charges generated by updraft are distributed in the cloud. The time variations both of the peak current and the duration time of electric field enhancement show a similar

variations. It is found that occurrence frequency of –CG shows temporal decrease in advance of the occurrence of downburst on the ground by ~15 minutes, while the area size of radar echo height more than 12 km is continuously increasing for the first time in Japan. It is possible that large negatively-charged particles (hail and graupel) carried upward by strong updraft approach the positively-charged particles (ice crystal), then the occurrence frequency of –CG decreases. In addition, it is found that –CG with absolute iCMC smaller than 5 C·km is dominant in the occurrence time period of the downburst. It is possible that negatively-charged hails and graupels fall to the ground with downburst, or negative charges decrease by IC and –CG activities, and the ratio of –CGs with iCMC less than 5 C·km in absolute value increases.

These results in this thesis are expected for leading to link the lightning data including iCMC and short-term meteorological forecast in the future.

5.2 Suggestions for future work

5.2.1 Development of lightning geo-location system

The lightning geo-location system for real-time monitoring of lightning activity should be established. Currently the lightning geo-location system is developing in partnership with Salesian Polytechnic, Tokyo, Japan and the basic method of geo-location for the CGs has been established. Information of the lightning magnitudes such as iCMC would improve accuracy meteorological forecast and would contribute to disaster prevention or mitigation in the region of low-density meteorological observation network.

5.2.2 Relationship between lightning activity and time variation of vertical structure of thunderstorm

It is found that iCMC intensity more than 5 C·km of –CG increases with the development of thunderstorm. One possible explanation is that the negative charges in

the cloud are carried upward by updraft or many negative charges generated by updraft are distributed. In order to confirm the cause of increase in iCMC, the quantitative relationship between lightning activity and the time variation of vertical structure of thunderstorm are to be examined using a volume scan radar data. X-band polarimetric radar operated at a frequency of 9.375 GHz in Kanto region, Japan can estimate raindrop size distribution [*Maki et al.*, 2005; *Kim et al.*, 2010]. The quantitative relationship between the lightning activity and distribution of raindrop size in the thunderstorm also can be investigated using X-band polarimetric radar data.

5.2.3 Quantitative analysis of severe weather events

In this thesis, it is shown that 2 downburst-producing thunderstorms have the feature of decreasing in occurrence frequency of –CG flashes in advance of the occurrence of downburst at the surface. *Kuhlman et al.* [2010] suggested that the downburst is not always accompanied by lightning jump. *Metzenger* [2010] suggested that lightning jumps are classified into three different types (hail type lightning jump, wind type lightning jump and mixed type lightning jump). The number of the cases is to be increased in order to establish the quantitative relationship between lightning activity and severe weather (downburst, tornado and hail). These examination may contribute to improvement of short period severe weather forecast.

Bibliography

Abarca, S. F., K. L. Corbosiero, and T. J. Galarneau Jr. (2010), An evaluation of the Worldwide Lightning Location Network (WWLLN) using the National Lightning Detection Network (NLDN) as ground truth. *J. Geophys. Res.*, *115*, D18206, doi:10.1029/2009JD013411.

Alexander, G. D., J. A. Weinman, V. M. Karyampudi, W. S. Olson, and A. C. L. Lee (1999), The Effect of Assimilating Rain Rates Derived from Satellites and Lightning on Forecasts of the 1993 Superstorm. *Mon. Wea. Rev*., 127, 1433-1457.

Baba, Y., and V. A. Rakov (2007), Electromagnetic models of the lightning return stroke, *J. Geophys. Res.*, *112*, D04102,doi:10.1029/2006JD007222.

Bennett, A. J., C. Gaffard, J. Nash, G. Callaghan, and N. C. Atkinson (2011), The Effect of Modal Interference on VLF Long-Range Lightning Location Networks Using the Waveform Correlation Technique. *J. Atmos. Oceanic Technol.*, *28*, 993-1006.

Berger, K. (1967), Novel observations on lightning discharges: Result of research on Mount San Salvatore. *J. Franklin Inst.*, *283*, 478-525.

Biagi, C. J., K. L. Cummins, K. E. Kehoe, and E. P. Krider (2007), National Lightning Detection Network (NLDN) performance in southern Arizona, Texas, and Oklahoma in 2003-2004, *J. Geophys. Res.*, *112*, D05208, doi:10.1029/2006JD007341.

Bruning, E. C., W. D. Rust, T. J. Schuur, D. R. MacGorman, P. R. Krehbel, and W. Rison (2007), Electrical and Polarimetric Radar Observations of a Multicell Storm in TELEX. *Mon. Wea. Rev.*, *135*, 2525-2544, doi:10.1175/2010MWR3160.1.

Burke, C. P. and D. L. Jones (1992), On the polarity of and continuing currents in unusually large lightning flashes deduced from ELF events, *J. Atmos. Terr. Phys.*, *54*, 243.

Carey, L. D., and S. A. Rutledge (1998), Electrical and multiparameter radar observations of a severe hailstorm , *J. Geophys. Res.*, *103(D12)*, 13979-14000.

Carey, L. D. and S. A. Rutledge (2000), The relationship between precipitation and lightning in tropical island convection: A C-band polarimetric radar study. *Mon. Wea. Rev.*, *128*, 2687-2710.

Carey, L. D., and S. A. Rutledge (2003), Characteristics of cloud-to-ground lightning in severe and nonsevere storms over the central United States from 1989-1998, *J. Geophys. Res.*, *108(D15)*, 4483, doi:10.1029/2002JD002951.

Chang, D. E., J. A. Weinman, C. A. Morales, and W. S. Olson (2001), The Effect of Spaceborne Microwave and Ground-Based Continuous Lightning Measurements on Forecasts of the 1998 Groundhog Day Storm. *Mon. Wea. Rev.*, *129*, 1809-1833.

Cummer, S. A. (2000), Modeling electromagnetic propagation in the Earth-ionosphere waveguide, *IEEE Trans. Antennas Propagat.*, *48*, pp.1420-1429.

Cummer, S. A., and U. S. Inan (1997), Measurement of charge transfer in sprite-producing lightning using ELF radio atmospherics, *Geophys. Res. Lett.*, *24*, 1731-1734, doi:10.1029/97GL51791.

Cummer, S. A., and U. S. Inan (2000), Modeling ELF radio atmospheric propagation and exacting lightning currents form ELF observations, *Radio Sci.*, *35*, 385-394, doi:10.1029/1999RS002184.

Cummer, S. A., and W. A. Lyons (2004), Lightning charge moment changes in U.S. High Plains thunderstorms, *Geophys. Res. Lett.*, *31*, L05114, doi:10.1029/2003GL019043.

Cummer, S. A., W. A. Lyons, and M. A. Stanley (2013), Three years of lightning impulse charge moment change measurements in the United States, *J. Geophys. Res. Atmos*, *118*, 5176.5189, doi:10.1002/jgrd.50442.

Cummins, K., L.Martin, J. M. Edward, A. B. William, L. H. Richard, B. P. Alburt, and E. Pifer (1998), A Combined TOA/MDF Technology Upgrade of the U.S. National Lightning Detection Network, *J. Geopys. Res.*, *103*, 9035.

Cummins K and M. Murphy (2009), An Overview of Lightning Locating Systems: History, Techniques, and Data Uses, With an In-Depth Look at the U.S. NLDN (2009 - invited paper), *IEEE Transactions on Electromagnetic Cmpatibility*, *51 (3)*, pp. 499-518, August 2009.

Deierling, W., and W. A. Petersen (2008), Total lightning activity as an indicator of updraft characteristics, *J. Geophys. Res., 113*, D16210, doi: 10.1029/2007JD009598.

Dennis, A. S., and E. T. Pierce (1964), The return stroke of the lightning flash to Earth as a source of VLF atmospherics, *Radio Sci.*, *68D*, P. 777.

Dowden, R. L., J. B. Brundell and C. J. Rodger (2002), VLF lightning location by time of group arrival (TOGA) at multiple sites. *J. Atmos. Sol.-Terr. Phys.*, *64*, 817-830.

Fisher ,R. J., G. H. Schnetzer, R. Thottappillil, V. A. Rakov, M. A. Uman, and J. D. Goldberg (1993), Parameters of triggered-lightning flashes in Florida and Alabama, *J. Geophys. Res, 98.*, pp. 22,887-22,902.

Fujita, T. T. (1992) The mystery of severe storms. *WRL Research Paper 239*, University of Chicago, 298 pp.

Fullekrug, M., C. Price, Y. Yair, and E. R. Williams (2002), Letter to the Editor Intense oceanic lightning, *Ann. Geophys.*, *20*, 133-137, doi:10.5194/angeo-20-133-2002.

Gaffard, C., A. J. Bennett,N. C.Atkinson, J.Nash, E.Hibbett,G. Callaghan, P. Taylor, and P. Odams (2008), Observing lightning from the ground over large areas of the globe. *Proc. WMO Tech. Conf. on Instruments and Observing Methods*, St. Petersburg, Russia, WMO, 1(16).

Goodman, S. J., R. Blakeslee, H. Christian, W. Koshak, J. Bailey, J. Hall, E. McCaul, D. Buechler, C. Darden, J. Burks, T. Bradshaw, and P. Gatlin (2005), The North Alabama Lightning Mapping Array: Recent severe storm observations and future prospects, *Atmos. Res., 76*, 423-437.

Gungle, B., and E. P. Krider (2006), Cloud-to-ground lightning and surface rainfall in warm-season Florida thunderstorms, *J. Geophys. Res., 111*, D19203, doi:10.1029/ 2005JD006802.

Haddad, M. A., V. A. Rakov, and S. A. Cummer (2012), New measurements of lightning electric fields in Florida: Waveform characteristics, interaction with the ionosphere, and peak current estimates, *J. Geophys. Res.*, *117*, D10101, doi:10.1029/2011JD017196.

Holle, R. L., A. I. Watson, R. E. Lopez, D. R. Macgorman, R. Ortiz, and W. D. Otto (1994), The Life Cycle of Lightning and Severe Weather in a 3-4 June 1985 PRE-STORM Mesoscale Convective System. *Mon. Wea. Rev.*, *122*, 1798-1808.

Hu, W. and S. A. Cummer (2006), An FDTD Model for Low and High Altitude Lightning-Generated EM Fields, *IEEE Trans. Antennas Propagat.*, *54*, pp.1513-1522.

Huang, E., E. Williams, R. Boldi, S. Heckman, W. Lyons, M. Taylor, T. Nelson, and C. Wong (1999), Criteria for sprites and elves based on Schumann resonance observations, *J. Geophys. Res*., *104*, 16,943-16964, doi:1029/1999JD900139.

Huang, S. M., A. B. Chen, G. L. Yang, C. J. Hsu, C. L. Kuo, R. R. Hsu, S. A. Cummer, Y. Takahashi, and H. T. Su (2010) Radio Emission Recording Systems at NCKU-Taiwan. 2010 Asia-Pacific Radio Science Conference, 22~26 Sep. 2010, Toyama, Japan.

Hutchins, Michael L., Robert H. Holzworth, Craig J. Rodger, James B. Brundell, 2012: Far-Field Power of Lightning Strokes as Measured by the World Wide Lightning Location Network. *J. Atmos. Oceanic Technol.*, *29*, 1102–1110.

Idone, V. P., A. B. Saljoughy, R. W. Henderson, P. K. Moore, and R. B. Pyle (1993) A reexamination of the peak current calibration of the National Lightning Detection Network, *J. Geophys. Res.*, *98*, 18323-18332.

Ishii, M., F. Fujii, T. Shimohori, M. Saito, A. Sugita, and S. Hidayat (2001a), Detection efficiency of JLDN, *Proc. 12nd Ann. Confer. PE Soc. IEEJ Vol. B*, 191-192. (in Japanese)

Ishii, M., T. Shimohori, M. Saito, F. Fujii, S. Hidayat, Y. Miyake, and A. Sugita (2001b), Location Accuracy of JLDN Lightning Data, *Natl. Conv. Rec., IEE Japan*, pp. 2821. (in Japanese)

Japan Meteorological Agency (2013), Daily weather map, http://www.data.jma.go.jp/fcd/yoho/hibiten/index.html, accessed October 22, 2013.

Jones, D. L. (1970), Electromagnetic radiation from multiple return strokes of lightning, *J. Atmos. Terr. Phys.*, *32*, P. 1077.

Kamra, A. K., and S. D. Pawar (2007), Evolution of lightning in an isolated hailstorm of moderate size in the tropic, *J. Geophys. Res.*, *112*, D20205, doi:10.1029/2006JD007820.

Kase, H., Y. Takahashi, and K. Yamashita (2009), The relationship between the terrestrial gamma‐ray flashes occurrence and the charge moment change of parent lightning discharge, paper presented at AGU Chapman Conference on Effects of Thunderstorms and Lightning in the Upper Atmosphere, Penn. State Univ., University Park, 10.14 May.

Kempf, N. M., and E. P. Krider (2003), Cloud-to-Ground Lightning and Surface Rainfall during the Great Flood of 1993. *Mon. Wea. Rev.*, *131*, 1140-1149.

Keogh, S., E. Hibbett, J. Nash, and J. Eyre (2006), The Met Office Arrival Time Difference (ATD) system for thunderstorm detection and lightning location, *Met Office Forecasting Research Tech. Rep.*, *488*, 22 pp.

Kim, D-S, M. Maki and D-I. Lee (2010), Retrieval of Three-Dimensional Raindrop Size Distribution Using X-Band Polarimetric Radar Data. , *J. Atmos. Oceanic Technol*, *27*, 1265-1285.

Krider, E. P., A. E. Pifer, and D. L. Vance (1980), Lightning direction finding system for forest fire detection, *bull. Am. Meteorol. Soc*., Boston, Mass.

Kuhlman, K. M., T. M. Smith, and S. T. Irwin (2010), Lightning activity and charge structure of microburst producing storms, paper presented at 21st International Lightning Detection Conference, Orlando, Florida, USA.

Lu, G., S. A. Cummer, J. Li, F. Han, D. M. Smith, and B. W. Grefenstette (2011), Characteristics of broadband lightning emissions associated with terrestrial gamma ray flashes, *J. Geophys. Res.*, *116*, A03316, doi:10.1029/2010JA016141.

MacGorman, D. R., C. Emeric., and P. L. Heinselman (2012), Lightning activity in a hail-producing storm observed with phased-array radar, paper presented at 22nd International Lightning Detection Conference, Broomfield, Colorado, USA.

MacGorman, D. R., I. R. Apstolakopoulos, N. R. Lund, N. W. S. Demetriades, M. J. Murphy, and P. R. Krehbiel (2011), The timing of Cloud-to-Ground Lightning relative to total lightning activity, *Mon. Wea. Rev. 139*, doi:10.1175/MWR-D-11-00048.1.

MacGorman, D. R., and D. W. Burgess (1994), Positive cloud-to-ground lightning in tornadic storms and hailstorms. *Mon. Wea. Rev.*, *122*, 1671–1697.

MacGorman, D. R., D. W. Burgess, V. Mazur, W. D. Rust, W. L. Taylor and B. C. Johnson (1989), Lightning rates relative to tornadic storm evolution on 22 May 1981, *J. Atmos. Sci.*, *46*, 221-250.

Maki, M., and Coauthors (2005), Semi-operational rainfall observations with X-band multi-parameter radar. *Atmos. Sci. Lett.*, *6*, 12-18.

Mansell, E. R., C. L. Ziegler, D. R. MacGorman (2007), A Lightning Data Assimilation Technique for Mesoscale Forecast Models. *Mon. Wea. Rev.*, *135*, 1732-1748.

Marshall, R. A. (2009), Very low frequency radio signatures of transient luminous events above thunderstorms, *Ph.D. Thesis*, Stanford University.

Medeiros, C., and M. F. Saba (2012), Presence of continuing current in negative cloud-to-ground flashes, paper presented at 22nd International Lightning Detection Conference, Broomfield, Colorado, USA.

Metzger, E. L. (2010), The relationship between total cloud lightning behavior and radar derived thunderstorm structure, *Master thesis*, Naval Postgraduate School.

Narita, T., T. Yamada, A. Mochizuki, E. Zaima, and M. Ishii (2000), Observation of current waveshapes of lightning strokes on transmission towers, *IEEE Transactions on Power Delivery*, *15*, 429-35.

Nash, J., N. C. Atkinson, E. Hibbett, G. Callaghan, and P. L. Taylor (2005), Progress in introducing new technology sensor sites for the Met Office long-range lightning detection system. *Proc.WMO Tech. Conf. on Meteorological and Environmental Instruments and Methods of Observation (TECO-2005)*, Bucharest, Romania, World Meterological Organization, 2.9.

Ohkubo, A. (2004), Characteristics of VLF/ELF sferics associated with winter sprite events in Japan, *Master thesis*, Tohoku University.

Onogi, K., J. Tsutsui, H. Koide, M. Sakamoto, S. Kobayashi, H. Hatsushika, T. Matsumoto, N. Yamazaki, H. Kamahori, K. Takahashi, S. Kadokura, K. Wada, K. Kato, R. Oyama, T. Ose, N. Mannoji and R. Taira (2007), The JRA-25 Reanalysis. *J. Meteor. Soc. Japan*, *85*, 369-432.

Orville, R. E. (1991) Calibration of a magnetic direction finding network using measured triggered lightning return stroke peak currents, *J. Geophys. Res.*, *96*, 17135-17142.

Orville, R. E., and Gary R. Huffines, 2001: Cloud-to-Ground Lightning in the United States: NLDN Results in the First Decade, 1989–98. *Mon. Wea. Rev.*, *129*, 1179–1193.

Pessi, A. T., and S. Businger (2009), The Impact of Lightning Data Assimilation on a Winter Storm Simulation over the North Pacific Ocean. *Mon. Wea. Rev.*, *137*, 3177-3195.

Pessi, A. T., S. Businger, K. L. Cummins, N. W. S. Demetriades, M. Murphy, and B. Pifer (2009), Development of a Long-Range Lightning Detection Network for the Pacific: Construction, Calibration, and Performance, *J. Atmos. Oceanic Technol.*, *26*, 145-166.

Price, C. and B. Federmesser (2006), Lightning-rainfall relationship in Mediterranean winter thunderstorms, *Geophys. Res. Lett.*, *33*, L07813, doi:10.1029/2005GL024794.

Price, C., Y. Yair, A. Mugnai, K. Lagouvardos, M. C. Llasat, S. Michaelides, U. Dayan, S. Dietrich, F. Di Paola, E. Galanti, L. Garrote, N. Harats, D. Katsanos, M. Kohn, V. Kotroni,

M. Llasat-Botija, B. Lynn, L. Mediero, E. Morin , K. Nicolaides, S. Rozalis, K. Savvidou, and B. Ziv (2011), Using lightning data to better understand and predict flash floods in the Mediterranean, *Surveys in Geophysics*, *32(6)*, 733-751.

Rakov, V., and M. A. Uman (1998), Review of Lightning Return Stroke Models, *IEEE Trans. EMC, 40*, No. 4, pp. 403-426.

Rakov, V. A. and M. A. Uman (2003) Lightning Physics and Effects, *Cambridge University Press*, The Edinburgh Building, Cambridge.

Rakov, V. A. (2007), Lightning return stroke speed, *J. Lightning Res.*, *Vol.1*, pp.80-89.

Rodger, C. J., J. B. Brundell, R. H. Holzworth, E. H. Lay, N. B. Crosby, T.-Y. Huang, and M. J. Rycroft (2009), Growing detection efficiency of the World Wide Lightning Location Network. *AIP Conf. Proc.*, *1118*, Corte, France, AIP, 15-20, doi:10.1063/1.3137706.

Said, R. K., U. S. Inan, and K. L. Cummins (2010), Long‐range lightning geolocation using a VLF radio atmospheric waveform bank, *J. Geophys. Res.*, *115*, D23108, doi:10.1029/2010JD013863.

Sato, M. (2004), Lightning and Sprite Activities and Their Solar Activity Dependencies, *Ph. D. thesis,* Tohoku University.

Sato, M., Y. Takahashi, A. Yoshida, and T. Adachi (2008), Global distribution of intense lightning discharges and their seasonal variations, *J. Phys. D: Appl. Phys.*, *41*, 234011.

Sato, M., F. Tsuchiya, N. Honma, D. Tsurushima, and Y. Takahashi (2013), Lightning Current Measurement Based on ELF Magnetic Field Observations, AP-RASC 2013, Sep. 3-7 2013, Taipei, Taiwan.

Schoene, J., M. A. Uman, and V. A. Rakov (2010), Return stroke peak current versus charge transfer in rockettriggered lightning, *J. Geophys. Res.*, *115*, D12107, doi:10.1029/2009JD013066.

Seity, Y., S. Soula, P. Tabary, and G. Scialom (2003), The convective storm system during IOP 2a of MAP: Cloud-to-ground lightning flash production in relation to dynamics and microphysics, *Q. J. R. Meteorol. Soc.*,*129*, 523-542.

Smith, D. A., M. J. Heavner, A. R. Jacobson, X. M. Shao, R. S. Massey, R. J. Sheldon, and K. C. Wiens (2004), A method for determining intracloud lightning and ionospheric heights from VLF/LF electric field records, *Radio Sci.*, *39*, RS1010, doi:10.1029/2002RS002790.

Soula, S., and S. Chauzy (2001), Some aspects of the correlation between lightning and rain activities in thunderstorms, *Atmos. Res.*, *56*, 355– 373.

Soula, S., Y. Seity, L. Feral, and H. Sauvageot (2004), Cloud-to-ground lightning activity in hail-bearing storms, *J. Geophys. Res*., *109*, D02101, doi:10.1029/2003JD003669.

Stolzenburg, M. (1994), Observations of high ground flash densities of positive lightning in summertime thunderstorms, *Mon. Weather Rev.*, *122*, 1740-1750.

Takahashi, T. (1978), Riming electrification as a charge generation mechanism in thunderstorms, *J. Atmos. Sci.*, *35*, 1536-1548, 1978.

Tapia, A., J. A. Smith, and M. Dixon (1998), Estimation of Convective Rainfall from Lightning Observations. *J. Appl. Meteor.*, *37*, 1497-1509.

Tessendorf, S. A., L. J. Miller, K. C. Wiens, and S. A. Rutledge (2005), The 29 June 2000 supercell observed during STEPS. part I: Kinematics and microphysics, *J. Atmos. Sci.*, *62(12)*, 4127-4150

Thomas, J. N., N. N. Solorzano, S. A. Cummer, and R. H. Holzworth (2010), Polarity and energetics of inner core lightning in three intense North Atlantic hurricanes, *J. Geophys. Res.*, *115*, A00E15, doi:10.1029/2009JA014777.

Thottappillil, R., and M. A. Uman (1993), Comparison of lightning return-stroke models, *J. Geophys. Res.*, *98*, pp. 22,903-22,914.

Uman, M. A. (1984), Lightning, *Dover*, 264pp.

Uman, M. A., D. K. McLain, and E. P. Krider (1975), The electromagnetic radiation from a finite antenna, *Amer. J. Phys.*, *43*, pp. 33-38.

Wakimoto, R. M. and V. N. Bringi (1988), Dual-Polarization observation of Microbursts associated with intense convection: The 20 July storm during the MIST project, *Mon. Wea. Rev. 116*, 1521-1539.

Weidman, C. D., and E. P. Krider (1986), The amplitude spectra of lightning radiation fields in the interval from 1 to 20 MHz, *Radio Sci.*, *21*, 964.

Wessel, P. and W. H. F. Smith (1998), New, improved version of the Generic Mapping Tools released, *Eos Trans. AGU*, *79*, 579.

Wiens, K. C., S. A. Rutledge, and S. A. Tessendorf (2005), The 29 June 2000 supercell observed during STEPS. part II: Lightning and chargestructure, *J. Atmos. Sci.*, *62(12)*, 4151-4177.

Williams, E. R., W. E. Weber, and R. E. Orville (1989), The Relationship Between Lightning Type and Convective State of Thunderclouds, *J. Geophys. Res.*, *94*, pp. 13,213-13,220.

Williams, E., B. Boldi, A. Matlin, M. Weber, S. Hodanish, D. Sharp, S. Goodman, R. Raghavan, and D. Buechler (1999), The behavior of total lightning activity in severe Florida Thunderstorms, *Atmos. Res. 51*, 245-265.

Williams, E. R., E. Downes, R. Boldi, W. Lyons, and S. Heckman (2007a), Polarity asymmetry of sprite‐producing lightning: A paradox?, *Radio Sci.*, *42*, RS2S17, doi:10.1029/2006RS003488.

Wilson, J. W., and R. M. Wakimoto (2001), The Discovery of the Downburst: T. T. Fujita's Contribution. Bull. *Amer. Meteor. Soc.*, *82*, 49-62.

Yamashita, K., Y. Takahashi, M. Sato, and H. Kase (2011), Improvement in lightning geolocation by time‐of‐arrival method using global ELF network data, *J. Geophys. Res.*, *116*, A00E61, doi:10.1029/2009JA014792.

Yanagi, Y. (2012), Development of VLF electromagnetic wave observation system and estimation method of lightning peak current, *Master thesis*, Hokkaido University.

Zipser, E. J., and K. R. Lutz (1994), The Vertical Profile of Radar Reflectivity of Convective Cells: A Strong Indicator of Storm Intensity and Lightning Probability?. *Mon. Wea. Rev.*, *122*, 1751-1759.